Master's thesis

NTNU
Norwegian University of Science and Technology
Faculty of Engineering
Department of Marine Technology

Daniel Kaasa

Integrated dynamic analysis of a semi-submersible wind turbine considering hull flexibility

Master's thesis in Marine Technology
Supervisor: Assoc. Professor Erin E. Bachynski
June 2019

NTNU
Norwegian University of
Science and Technology

Daniel Kaasa

Integrated dynamic analysis of a semi-submersible wind turbine considering hull flexibility

Master's thesis in Marine Technology
Supervisor: Assoc. Professor Erin E. Bachynski
June 2019

Norwegian University of Science and Technology
Faculty of Engineering
Department of Marine Technology

NTNU
Norwegian University of
Science and Technology

MSC THESIS IN MARINE TECHNOLOGY

SPRING 2019

FOR

STUD.TECHN. Daniel Kaasa

Integrated dynamic analysis of a semi-submersible wind turbine considering hull flexibility

Integrert dynamisk analyse av en halvt nedsenkbar flyttende vindturbin inkludert elastisitet i skroget

Background:

The wind industry has developed very fast in recent years, moving from onshore to offshore in shallow water and then to floating wind turbines (FWTs) in deep water. Global dynamic analysis of FWTs has typically focused on the dynamic loads in the tendons and tower, while structural design of the hull has been based on hydrostatic loads and hydrodynamic loads in the frequency domain.

Hydrodynamic loads for large-volume structures depend strongly on frequency, and novel methods are needed to simultaneously and efficiently account for structural flexibility and distributed hydrodynamic loading in coupled global analysis. The present work will examine the OO-Star Wind Floater, considering beam models for the hull.

The main objectives for the work are:

- Evaluate the expected internal forces in the structure and structural dynamics of the floater with different wave theories to check possible model strategies.
- Develop a framework for a fully coupled model including floater dynamics and possibly hydroelasticity.

The study should focus on wave loading and to what extent, and when, wave loads can be represented with the different modelling strategies. It is proposed to evaluate the following modelling types:

1. Rigid body model using first order potential theory (frequency domain)
2. Rigid body model using Morison's equation
3. Flexible beam model using Morison's equation
4. Flexible beam model using distributed loads from first order potential theory

The first objective will be to evaluate when the different theories are applicable. Both the global mo-

tions and local internal forces in the substructure should be verified. The effect of possible structural dynamics in the substructure should also be evaluated. The main objective will be to develop a modelling strategy for analyzing the OO-Star Wind Floater. If relevant, the response in the tower should also be evaluated and discussed. The 10MW OO-Star Wind Floater developed in the Lifes50+ project can be used as basis.

Assignment:
The following tasks should be addressed:

1. Literature review regarding hydrodynamic load models and hydroelasticity for floating wind turbines.
2. Finalize verification (decay tests, regular waves) of an existing SIMA model of the 10MW OO-Star Wind Floater with rigid hull and first order potential flow loads. Investigate the sensitivity of the results to the mesh in the first order potential flow solver. Extract loads at different cross sections based on the frequency domain model.
3. Build model 2) and compare global responses for the rigid floater with different hydrodynamic load formulations.
4. Development of a beam element model of the 10 MW OO-Star Wind Floater and estimation of hull natural frequencies and mode shapes. Compare global responses for models 2) and 3) to investigate effects of structural flexibility.
5. Development of a distributed potential flow model (pressure integration from WAMIT) using the same beam element model from task 4. Comparison of global responses and internal loads for the four models developed during the thesis to see the combined effects of hydrodynamic and structural modelling.
6. Report and conclude on the investigation.

The work scope could be larger than anticipated. Subject to approval from the supervisor, topics may be deleted from the list above or reduced in extent.

In the project, the candidate shall present his personal contribution to the resolution of problem within the scope of the project work.

Theories and conclusions should be based on mathematical derivations and/or logic reasoning identifying the various steps in the deduction.

The candidate should utilize the existing possibilities for obtaining relevant literature.

The project report should be organized in a rational manner to give a clear exposition of results, assessments, and conclusions. The text should be brief and to the point, with a clear language. Telegraphic language should be avoided.

The project report shall contain the following elements: A text defining the scope, preface, list of contents, main body of the project report, conclusions with recommendations for further work, list of symbols and acronyms, reference and (optional) appendices. All figures, tables and equations shall be numerated.

The supervisor may require that the candidate, in an early stage of the work, present a written plan for the completion of the work. The plan should include a budget for the use of computer and laboratory resources that will be charged to the department. Overruns shall be reported to the supervisor.

The original contribution of the candidate and material taken from other sources shall be clearly defined. Work from other sources shall be properly referenced using an acknowledged referencing system.

Supervisor Erin Bachynski, Assoc. Professor, Dept. of Marine Technology, NTNU

Deadline: 11.06.2018

Preface and acknowledgements

This master thesis has been conducted at the Department of Marine Technology of the Norwegian University of Science and Technology (NTNU) in Trondheim, Norway. It has been completed as the concluding work for obtaining the degree of Master of Science in Marine Engineering from NTNU.

My personal goal of this thesis was to get more familiar with different modelling procedures of hydrodynamic loads on floating structures in software used in marine industry today. Combining this with floating wind turbines, which is seen as a great possibility to increase the amount renewable energy in the world, was a bonus. The topic is very up to date, and working with a company that has interest of the work done in this thesis was an extra motivation.

The work in this study has been very challenging. The combination of a lot of different theories, multiple new software and new tasks that I have never done before made it difficult numerous times. The upside of this study is that I have learned a lot from it. I have increased my knowledge regarding hydrodynamic loads, and further developed my software skills. In addition, the construction of a scientific report has proven to be more demanding than anticipated. This made it a great experience to have for the future.

The work done in this thesis was supervised by Erin E. Bachynski, Associate Professor at Department of Marine Technology, NTNU. I am very thankful for all the help I have received during this thesis. Her guidance and sharing of knowledge throughout the entire project from design and modelling to interpret results from analyses and software problems have been brilliant. I am also grateful to Håkon S. Andersen and Mathias Marley from Dr. techn. Olav Olsen for the help and support during this thesis.

Daniel Kaasa

Abstract

The worlds greenhouse gas emissions today need to be reduced, and this has led to an increased interest for offshore wind turbines. The semi-submersible wind turbine (SSWT) concept OO-Star Wind Floater Semi 10 MW has shown promising results and chosen for further studies. It is believed to be a cost efficient floating wind turbine solution with all the qualities required by the future floating offshore wind market. Previous studies of dynamic analysis of floating offshore wind turbines have usually modelled the hull as rigid. The hydrodynamic loads for large-volume structures depend strongly on frequency, and novel methods are needed to include both flexibility and correct hydrodynamic loads in the global dynamic analysis. This study presents different modelling strategies for hydrodynamic loads, and an attempt on a new method for including the large-volume hydrodynamic loads.

Four different hydrodynamic models were supposed to be made and evaluated in this study. The first one to be made was a rigid body model using first order potential theory. A 3D panel model was generated for the hull, and frequency-dependent added mass, radiation damping and excitation forces were calculated for the hull as a whole. The final model was generated as a SIMO-RIFLEX model in SIMA. Analyses in terms of decay tests and a regular waves test were performed on the model to verify previous results. The results were the same or could be explained except for the natural period in pitch which was -6.3% in difference. The sensitivity of the results to the mesh in the first order potential flow solver was also checked and seen to be approximately the same for the chosen mesh sizes. The second model to be made was the rigid body model using Morison's equation. The added mass in vertical and horizontal direction were estimated from the frequency-dependent added mass from the first order potential theory model. Analyses in terms of decay tests and a regular waves test were performed on the model and compared with rigid body model using first order potential theory. The natural periods were more or less the same. The regular waves test showed larger surge motion for the first order potential theory model, while the heave and pitch motion varied depending on the wave period. The third model to be made was the flexible beam model using Morison's equation. Analyses in terms of decay tests and a regular waves test were performed on the model and compared with rigid body model using Morison's equation. The natural periods were the same or could be explained except for the natural period in pitch which was 7.3% in difference. The regular waves test showed same surge motion in the models, and larger heave motion in the flexible beam model. There was uncertainties connected to the pitch motion, and a conclusion was not made.

An attempt was made to generate a flexible beam model using distributed loads from first order potential theory. A new method was tried by implementing radiation and diffraction pressures from potential theory as hydrodynamic load input for sections of the hull by using SIMO-bodies. This was not finished due to software problems and limited time.

Sammendrag

Verdens klimagassutslipp idag må reduseres, og dette har ført til økt interesse for offshore vindturbiner. Den halvt nedsenkbare vindturbin (SSWT) konseptet OO-Star Wind Floater Semi 10 MW har vist lovende resultater og valgt for videre studier. Det antas å være en kostnadseffektiv flytende vindturbin med alle de kvalitetene som kreves av det fremtidige flytende offshore vindmarkedet. Tidligere studier med dynamisk analyse av flytende vindturbiner har vanligvis modellert skroget som stivt. De hydrodynamiske belastningene for stor-volum strukturer er sterkt avhengige av frekvens, og nye metoder er nødvendig for å inkludere både fleksibilitet og korrekte hydrodynamiske belastninger i den globale dynamiske analysen. Denne oppgaven presenterer ulike modelleringsstrategier for hydrodynamiske belastninger, og et forsøk på en ny metode for å inkludere stor-volum hydrodynamiske belastninger.

Fire forskjellige hydrodynamiske modeller skulle bli laget og evaluert i denne studien. Den første som skulle bli lagd var en model med stivt skrog og første ordens potentialteori. En 3D-panelmodell ble generert for skroget, og frekvensavhengig tilleggsmasse, strålingsdemping og eksitasjonskrefter ble beregnet for skroget som en helhet. Den endelige modellen ble generert som en SIMO-RIFLEX-modell i SIMA. Analyser i form av krengeprøver og en vanlig bølger test ble utført på modellen for å bekrefte tidligere resultater. Resultatene var de samme eller kunne forklares bortsett fra den naturlige perioden i stamp som var -6,3 % i forskjell. Sensitiviteten til resultatene til mesh i modellen med stivt skrog og første ordens potentialteori ble også kontrollert og sett til å være omtrent det samme for de valgte mesh størrelsene. Den andre modellen som skulle lages var en model med stivt skrog og Morisons ligning. Tilleggsmassen i vertikal og horisontal retning ble estimert fra den frekvensavhengige tilleggsmassen fra modellen med stivt skrog og første ordens potentialteori. Analyser i form av krengeprøver og en vanlig bølger test ble utført på modellen og sammenlignet med modellen med stivt skrog og første ordens potentialteori. De naturlige periodene var mer eller mindre de samme. Den vanlige bølger testen viste større jag bevegelse for modellen med stivt skrog og første ordens potentialteori, mens hiv og stamp bevegelsene varierte avhengig av bølgeperioden. Den tredje modellen som skulle lages var den fleksible bjelkemodellen og Morisons ligning. Analyser i form av krengeprøver og en vanlig bølger test ble utført på modellen og sammenlignet med modellen med stivt skrog og Morisons ligning. De naturlige perioder var de samme eller kunne forklares bortsett fra den naturlige perioden i stamp som var 7,3 % i forskjell. Den vanlige bølgetesten viste samme jag bevegelse i modellene, og større hiv bevegelse i den fleksible bjelkemodellen og Morisons ligning. Det var usikkerheter knyttet til stamp bevegelsen, og en konklusjon ble ikke gjort.

Det ble forsøkt å generere en fleksibel bjelkemodell med distribuerte belastninger fra førsteordens potensialteori. En ny metode ble prøvd ved å implementere strålings- og diffraksjonstrykk fra potensielteori som hydrodynamisk belastning for deler av skroget ved hjelp av SIMO-kropper. Dette ble ikke fullført på grunn av data problemer og begrenset tid.

Contents

List of Figures

List of Tables

List of acronyms

CFD	Computational Fluid Dynamics
COB	Center Of Buoyancy
COG	Center Of Gravity
DAF	Dynamic Amplification Factor
DOF	Degreee Of Freedom
FBM	Flexible Body Morison
FBP	Flexible Body Potential
FEM	Finite Element Method
FFT	Fast Fourier Transform
FWT	Floating Wind Turbine
KC	Keulegan-Carpenter number
MDOF	Multi Degree Of Freedom
MSL	Mean Sea Level
MWL	Mean Water Level
PSD	Power Spectral Density
RAO	Response Amplitude Operator
RBM	Rigid Body Morison
RBP	Rigid Body Potential
Re	Reynolds number
RNA	Rotor Nacelle Assembly
SDOF	Single Degree Of Freedom
SSWT	Semi-Submersible Wind Turbine
TLP	Tension Leg Platform
TLPWT	Tension Leg Platform Wind Turbine

List of symbols

$\mathbf{A}$	Added mass matrix
$\mathbf{B}$	Damping matrix
$\mathbf{C}$	Hydrostatic restoring matrix
$\mathbf{M}$	Mass matrix
A_{kj}	Added mass coefficients
B_{kj}	Damping coefficients
C_{kj}	Hydrostatic restoring coefficients
C_D	Drag coefficient
C_M	Mass coefficient
D	Diameter of cylinder
F	Excitation forces
$F_{\mathrm{exc,k}}$	Wave excitation loads
$\overline{GM_L}$	Longitudinal metacentric height
$\overline{GM_T}$	Transverse metacentric height
H_s	Significant wave height
K	Mooring system restoring matrix
M	Mass
T	Wave period
T_p	Wave peak period
V	Displaced volume of water
Ws	Wind speed

dF	Horizontal force per unit length
g	Gravity acceleration
h	Water depth
k	Wave number
p	Pressure
p_a	Atmospheric pressure
u	Horizontal fluid velocity
$\dot{u}$	Horizontal acceleration velocity
z_B	Vertical coordinate for COB
z_G	Vertical coordinate for COG

η	Motion
λ	Wave length
∇	Gradient
ω	Wave frequency
ρ	Density of water
θ	Velocity potential
θ_D	Diffraction velocity potential
θ_{diff}	Diffraction problem velocity potential
θ_{rad}	Radiation problem velocity potential
θ_0	Incident waves velocity potential

1 Introduction

The world energy consumption is increasing everyday and this leads to greater demand of energy in the future [1]. Fossil fuel depletion is identified as a future challenge and the importance of investigating alternative energy resources is increasing. A large part of the energy in the future also needs to be clean due to climate change. Renewable energy sources, such as wind, sun and hydro, are believed to be an important part of the future's cleaner energy mix. Wind power generation has approximately zero direct emissions connected to it when in production, and therefore the emissions are only connected to the manufacturing, transport etc.

The EU has set itself targets for reducing its greenhouse gas emissions and increasing the amount of renewable energy progressively up to 2050. Key climate and energy targets are set to be 20% of EU energy from renewable energy by 2020, and 27% by 2030 [2]. Wind energy is an extremely important renewable energy source for the EU and has overtaken coal as the second largest form of power generation capacity with a total net installed capacity of 168.7 GW in 2017. This means that wind energy now stands for 18% of EU's total installed power generation capacity [3].

1.1 Offshore wind energy

In order to reach the renewable energy targets set by EU, more and larger wind turbines are needed. More than 70% of the earth is ocean and therefore are offshore wind farms an important part of the solution [4]. Moving from onshore to offshore wind farms leads to some differences in terms of problems that need to be solved. The main differences are:

- The main environmental loads on an onshore wind turbine are aerodynamic loads from the wind. An offshore wind turbine has additional environmental loads such as hydrodynamic loads from waves and currents. This leads to different design requirements.
- An offshore wind turbine has a substructure under the wind turbine (monopile, jacket or floating platform etc).
- Installation and maintenance are more costly due to difficulties of installation and accessibility for maintenance.
- The offshore wind farms are exposed to sea water and this leads to more corrosive environment compared to onshore.
- The electrical cable from the offshore wind farm to the electric grid onshore needs to be a submarine cable.

- The planning of a location of an offshore wind farm needs to account for activities such as ship traffic, marine life, fishery etc.

Offshore wind farms have been more costly by a large margin than installing onshore for a long time. Higher production, installation, maintenance and operation costs have been the main reasons. Still, there are clear benefits with developing offshore wind turbines compared to onshore. The wind offshore is normally stronger and more consistent than onshore due to more or less no obstacles. This means that the wind resource is larger offshore and a higher amount of energy can be produced per wind turbine. The capacity factor, which measures the actual output as a share of the total output capacity over a period in time, can in some cases be twice as large for offshore wind power compared with onshore [5]. Other benefits of offshore wind farms are that there are more or less no space restrictions. Wind turbines also makes a lot of noise and visual impact on humans which will be reduced by placing them offshore.

Offshore wind farms have started to show large improvements with respect to costs connected to them in recent years. In the report *Europe power by green energy* by Ørstad, the cost for offshore wind energy have been significantly reduced [5]. This can be seen in Figure 1.1 where the costs for different energy sources are compared. Offshore wind energy is now cheaper than "black energy" (coal, natural gas, nuclear etc.) and closing in onshore wind energy. This is based upon the cost for offshore wind including cost of transmission - calculated as levelized revenue (subsidy and market price) of electricity over 25 year lifetime. There are several reasons behind this, but the main reasons are:

- Industrialization: Clear and ambitious national plans for build out allowed for industrialization in every part of the supply chain, thus bringing down the cost per unit.
- Innovation: Research, development and digitalization has resulted in cheaper, more efficient and durable components, and in new methods of production, installation and maintenance.
- Scale: Wind turbines and farms have grown significantly, resulting in more production per turbine and hence producing at a lower cost of energy.

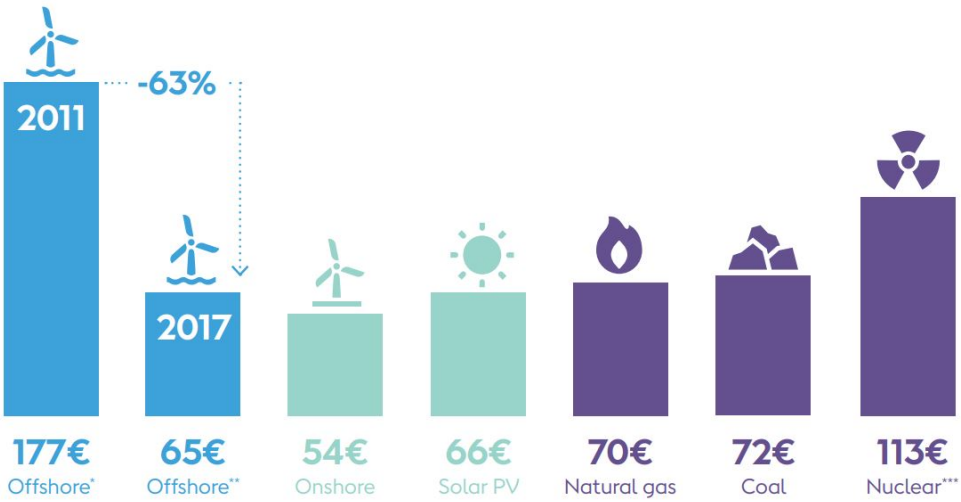

Figure 1.1: Cost of offshore wind energy compared with other sources EUR per MWh (2016 prices) [5].

The first offshore wind farm was installed in Denmark in 1991, and since then have many more been installed all over Europe. The wind power capacity in the EU in 2017 was 168.7 GW, where 153 GW was onshore and 15.8 GW was offshore [3]. More or less all of the offshore wind farms are installed with bottom fixed substructures in shallow waters in the North Sea. However, the first floating offshore wind turbine farm was installed of the coast of Scotland in 2017 [6]. The bottom fixed substructure concepts used today are monopiles, jackets, gravity based and tripods, where monopiles are mostly used by a large margin. These bottom fixed substructures are not economically feasible for larger water depths (40-50 m) [7]. This leads to the main motivation for developing floating concepts. where the floating substructures are moored to the seabed. Some of the disadvantages of floating substructures are more transmission loss, more complexity of blade controls because of body motions, larger inertia loading on tower due to greater floater accelerations, and possibly more expensive/complicated installation processes [8].

1.2 Floating wind turbine concepts

Floating support structures for wind turbines consist of several different main parts and can be divided into the following categories:

- Floating substructure: Main purpose is to maintain buoyancy and structural integrity.
- Mooring: To connect the floater to the seabed, typically by chains or cables.
- Anchoring: For connecting the mooring lines to the seabed.
- Electrical cable: Submarine cable for export of power.

The focus in this report will be on the floating substructure and therefore will the other categories only be briefly mentioned. The four main concepts on floating structures for wind turbines will be introduced and briefly explained in the following sections. Other concepts and different variants of these exist, for example mounting of multiple wind turbines onto a single floating structure, but will not be further discussed in this report.

1.2.1 Spar buoy

The spar buoy concept is a deep, thin vertical floating buoy with small waterline area. It is characterized by its large draft and gets its stability by heavy ballast deep in the hull so the center of gravity is beneath the center of buoyancy. Catenary mooring lines are normally used to moor the spar to the seabed. The first floating offshore wind turbine farm was installed of the coast of Scotland in October 2017 by Equinor. It consists of five 6 MW spar buoys and is called Hywind Scotland [6].

Figure 1.2: The Hywind Scotland floating wind farm by Equinor [6].

1.2.2 Semi-submersible

The semi-submersible concept usually consists of a top deck supported by a number of vertical columns and connected by bracings or/and pontoons under water. It is known for good stability and medium draft. The vertical columns provide hydrostatic stability, while the pontoons provide additional buoyancy. Catenary lines is normally used to moor the semi-submersible to the seabed, same as the spar buoy.

Principle power installed WindFloat, a 2-MW prototype of a three column semi-submersible, in 2011 off the coast of Portugal. This was a success with respect to gaining operational data and experience for

future projects, and the semi-submersible was decommissioned in 2016 [9]. Fukushima Forward was another offshore wind concept for semi-submersible installed off the coast of Japan in 2015. It consists of three floating wind turbines up to 7-MW and one floating power sub-station [10].

Figure 1.3: The WindFloat concept by Principle Power [9].

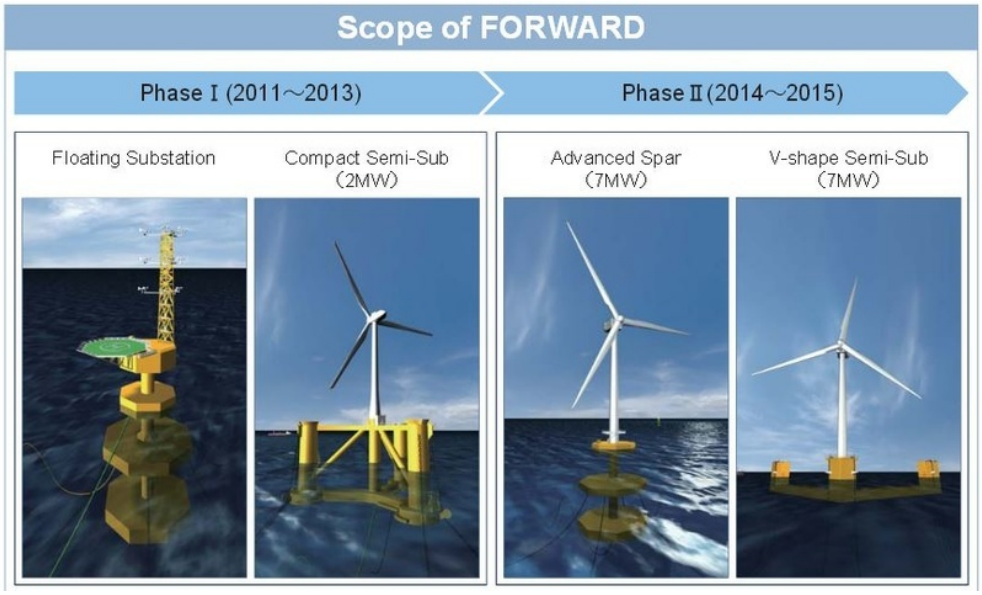

Figure 1.4: Fukushima floating offshore wind farm demostration project [10].

1.2.3 Tension leg platform

Tension leg platforms (TLP) obtain stability in the vertical plane, which are heave, roll and pitch motions, by stiff vertical tendons connected to the seabed. The tension legs are kept taut by having a larger buoyancy force than total weight. Stiffness in the horizontal plane, which are surge, sway, yaw motions, is obtained by geometric stiffness. TLP hulls can be both multi-column or single-column. In the latter case, long cantilever beams are required to obtain a large tendon footprint needed for roll pitch stiffness. Only small prototypes have been made, such as Blue H which was a 80-kW TLP wind turbine installed in 2008 [11], but Gicon has made concept designs of TLP wind turbine up to 10 MW [12].

Figure 1.5: An illustration of the TLP concept by Gicon [12].

1.2.4 Barge

The barge concept is a flat bottomed boat with large water plane area. It is characterized by its small draft and has catenary mooring lines, same as the spar buoy and semi-submersible concepts. Ideol installed Floatgen demostrator, a 2-MW prototype of a barge with a central opening, in 2018 off the coast of France. This was the world first floating barge designed for offshore wind. The central opening is to damp out the floater motions [13].

Figure 1.6: The Floatgen demostrator by Ideol [13].

1.2.5 Advantages and disadvantages of floating substructures

Floating wind turbines are complex structures. Many different types of floating foundations are proposed. Pros and cons of the various concepts, according to IRENA, are provided in Table 1.1. The list is based on the report *Floating Foundations: a Game Changer for Offshore Wind Power* by IRENA organization with some modifications [14].

Table 1.1: Advantages and disadvantages of different floating substructures [14].

Concept	Pros	Cons
Spar buoy	1) Tendency for lower critical wave-induced motions. 2) Simple design. 3) Lower installed mooring cost.	1) Offshore operations require heavy-lift vessels and relatively sheltered, deep water. 2) Needs deeper water than other concepts (> 100 m).
Semi-sub-mersible	1) Constructed onshore/dock. 2) Fully equipped platforms can float in shallow waters during transport. 3) Transport to site using conventional tugs. 4) Can be used in water depths ≥ 40 m. 5) Lower installed mooring cost.	1) Tendency for higher critical wave-induced motions. 2) Tends to use more material and larger structures in comparison to other concepts. 3) Complex fabrication compared with other concepts.
TLP	1) Tendency for lower critical wave-induced motions. 2) Low mass. 3) Can be assembled onshore/dock. 4) Can be used in water depths ≈ 50-60m.	1) Harder to keep stable during transport and installation. 2) A special purpose vessel may be required because of design. 3) Some uncertainty about impact of possible high-frequency dynamic effects on turbine. 4) Higher installed mooring cost.
Barge	1) Constructed onshore/dock. 2) Fully equipped platforms can float in shallow waters during transport. 3) Transport to site using conventional tugs. 4) Can be used in water depths ≥ 40 m. 5) Lower installed mooring cost. 6) Possibility for re-use.	1) Tendency for higher critical wave-induced motions. 2) Tends to use more material and larger structures in comparison to other concepts. 3) Different roll/pitch motion due to non-symmetric barge

1.3 Research aim and motivation

As mentioned before, the EU has set itself targets for reducing its greenhouse gas emissions and increasing the amount of renewable energy progressively up to 2050. Wind energy has been seen as an important renewable energy source and considered to be one of the main energy contributors in the future because of its current state and potential. The primary challenge for the wind energy industry

today is to reduce the costs. This is especially important for deep water offshore wind energy in order to compete with other energy sources. Offshore wind cannot rely on subsides in the future. There is a need for new innovative substructure concepts, and here is where LIFES50+ project comes in.

LIFES50+ is a large research project which is part of the The European Horizon 2020-funded program led by SINTEF Ocean [15]. The goal of the project is to develop cost efficient floating substructures for 10 MW wind turbines. The project started of with four different concepts and three different sites (North-west of Scotland, Maine area and the Mediterranean). Two of the concepts were chosen for phase two, where one of them is the OO-Star Wind Floater Semi 10 MW. This phase consists of further development of the two concepts including model testing. This was done in 2017/18 and the project is now in a finalization stage of this phase.

OO-Star Wind Floater Semi 10 MW is a semi-submersible wind turbine (SSWT) concept designed by Dr. Techn. Olav Olsen [16]. It is believed to be a very cost efficient floating solution with all the qualities required by the future floating offshore wind market [17]. The arguments for this are:

- It is a robust, stable and very simple three-leg semi-submersible floater.
- It has a passive ballast system.
- Can be used for water depth from 50 m.
- The substructure can be made in concrete, steel or a combination. The material selection will be based upon optimal design, cost, fabrication facilities etc.
- For large wind turbines will concrete be best suited. This is not fatigue sensitive and has a long design life, 100 years +. It is also possible to re-use the floater.
- The OO-Star Wind Floater consists of a central shaft supporting the wind turbine, and a tri-star shaped pontoon supporting three buoyancy cylinders for optimal stability.
- There is permanent buoyancy in the columns and shaft. The pontoons provide structural support of the columns, weight stability, damping/added mass and temporary buoyancy for inshore assembly.
- The fabrication can be done in a dock, on a barge or on a quay. The structure is well suited for modular fabrication.
- The substructure can float with very small draft and the unit can be fully assembled at quay-side before tow to site. It is not a requirement for deep water at assembly site.
- The transportation to site are done by towing. No requirements for expensive offshore heavy lifts.

The OO-Star Wind Floater Semi 10 MW is still an unproven concept and this leads to more documenta-

tion needed. Further numerical analyses of the concept is wanted to describe the physics of the structure in a more accurate way. One of these analyses is to find out how much the elasticity of the hull influence the global behaviour of the SSWT including the tower responses. It is desirable to do an analysis with a flexible hull and a rigid hull, and compare the results to investigate the elasticity effect.

The hydrodynamic loads for large-volume structures depend strongly on frequency, and novel methods are needed to simultaneously and efficiently account for structural flexibility and distributed hydrodynamic loading in a coupled global analysis. In this study, a relatively new approach was attempted to generate an elastic multi-body global analysis model of the SSWT. The idea of the method is to put SIMO-bodies in specific places in a beam model of the hull. Each of the SIMO-bodies represents a section. The radiation and diffraction pressures from first-order potential theory for a section are given as hydrodynamic load input for the SIMO-body representing the section. In this way will the resulting model become an elastic multi-body global analysis model with frequency-dependent hydrodynamic loads. The elasticity effect of the SSWT could then be investigated by creating another model with rigid body and first-order potential loads and compare the results from different analyses. The design of the OO-Star Wind Floater Semi 10 MW is more complex compared to other designs which have used the same approach before to generate an elastic multi-body global analysis model. By complex it is referred to multiple columns with varying diameter and heave plates are connected with tapered pontoons with shirt. Part of this study was therefore to investigate if the approach was well suited for more complex designs. The model with rigid body was made, but unfortunately, the elastic multi-body global analysis model was not finished in this study. The main reason for this was software problems.

Another aspect of this study was to investigate wave loading on a SSWT and to what extent, and when, wave loads can be represented with the different modelling strategies. Two more models of the SSWT were made in addition to the model with rigid body and first-order potential theory already mentioned. These were a beam model with Morison-type loading only and a model with rigid body and Morison type loading only. Comparison of results from analyses performed on the models were used to decide when the different modelling strategies were applicable for the SSWT.

To summarize, this study has the following main contributions:

1. A literature review regarding hydrodynamic load models and hydro-elasticity for floating wind turbines.
2. A hydrodynamic model of the SSWT with rigid hull and first order potential flow theory wave loading. Referred to as the RBP model. Verification of the RBP model with existing results and other calculations.
3. A hydrodynamic model of the SSWT with rigid hull and Morison-type loading only. Referred to as

the RBM model. Comparison of the RBM model with the RBP model.

4. A hydrodynamic model of the SSWT with flexible beam elements and Morison-type loading only. Referred to as the FBM model. Comparison of the FBM model with the RBM model.
5. An attempt of creating a hydrodynamic model of the SSWT with the new method for describing the hydrodynamic loads in a global analysis. A flexible beam model using distributed loads from first order potential theory. Referred to as the FBP model.

1.4 Related work

The wind industry has developed very fast in recent years, moving from onshore to offshore in shallow water and then to floating wind turbines (FWT) in deep water. Most of the commercial and academic software for analysing a FWT were originally designed for analysing onshore wind turbines. This often results in software with advanced aerodynamics and simplified hydrodynamics. An example of simplified hydrodynamics is that in some software, the only hydrodynamic model is slender element theory with Morison-type forces on the submerged part of the structure. The offshore industry has also developed software for FWT, which usually have the opposite problem with advanced hydrodynamics and limited aerodynamics. There are some FWT concepts, like the spar buoy, that are slender enough to be argued for using Morison's equation together with simplified pressure calculations for heave motions. But for large volume structure, such as semi-submersibles, the diffraction effects may be significant and need to be accounted for. Linear potential theory solved with boundary element methods has often been used for this.

There have been performed coupled global analysis for different substructure concepts of FWTs before, which have been published in papers. Many of them have been focusing on the spar wind turbine concept. More studies on the semi-submersible wind turbine (SSWT) concept have been done in recent years. An example of this is the LIFES50+ project where both concepts chosen for further studies were SSWTs [15]. To this author knowledge, most of the coupled global analysis have modelled the hull as rigid. This has been a suitable assumption before since both the wind turbines and the platforms have been small enough. For larger wind turbines, like a 10 MW wind turbine, larger platforms are needed. For increased dimensions of floating substructures, structural flexibility in the coupled global analysis may need to be accounted for in the preliminary design and optimization of large-volume floating substructures. A selected number of studies related to hydrodynamic numerical models and coupled global analysis will be presented in the following sections. The findings in the studies will be presented and connected to this master thesis.

Kvittem [18] performed a comparison study of the wave-induced response of a SSWT using Morison's

equation and potential flow theory with Morison drag. The floater was assumed to be rigid in both models. A new coupled simulation code was developed by linking the analysis software SIMO and RIFLEX hydrodynamic, structural and control system computational tools with the aerodynamic forces and wind field generation from AeroDyn and TurbSim. Wave-only simulations and some limited coupled wind-wave simulations were performed on the models and compared. The conclusion was that the Morison model with forces integrated up to wave elevation gave a good representation of the motions compared to the potential flow model with quadratic drag forces. Slender body theory by Morison's equation was sufficient for that particular semi-submersible in the analysis for wave periods between 7-21 seconds. The diffraction effects became important for heave motions when wave periods went below 7 seconds. The same hydrodynamic numerical models in terms of Morison's equation and potential flow theory with Morison drag have been used in this thesis. The linking of SIMO and RIFLEX software have also been done in this thesis through SIMA. Furthermore, the SSWT used in the study, which was very similar to the WindFloat [9], has some similarity to the OO-Star Wind Floater Semi 10 MW design in terms of multiple columns and heave plates. However, there is a distinct difference in the designs and that is the pontoons in the OO-Star Wind Floater Semi 10 MW.

Another comparison study on wave load effects was done by Nematbakhsh [19]. A tension leg platform wind turbine (TLPWT) was considered and computational fluid dynamics (CFD) was compared to potential flow theory. CFD models are capable of capturing nonlinear wave loads which was a concern that may excite the high natural frequencies of the TLPWT. A CFD model based on immersed boundary method in combination with two-body structural model of TLPWT was developed and compared with potential flow theory model made by SIMO-RIFLEX. The floater was assumed to be rigid in the models. Free decay test and regular waves test were performed on the models and compared. The results predicted by the CFD model showed good agreement with the potential flow theory model for small and medium amplitude waves. The only considerable difference was the TLPWT mean surge motion which was predicted higher by the CFD model. The differences between the models did not significantly affect the tendon forces and tower bending moment. The study shows a different hydrodynamic numerical model than the ones used in this thesis and could be an idea for future work. Nonlinear wave loads have not been assessed in this thesis and the study indicates that it is not that important for small and medium amplitude waves for the TLPWT concept. However, it is important to remember that the substructure concepts are different and different nonlinear effects will be important. The potential flow theory model was made by SIMO-RIFLEX as in this thesis. The same tests were performed in terms of decay tests and regular waves tests.

A very similar master thesis to this one was done in 2016 by Svendsen [20]. He did a master thesis regarding structural design and dynamic analysis of a tension leg platform wind turbine (TLPWT), considering elasticity in the hull. The same method in terms of generating a multi-body global analysis model of an FWT was used in his master thesis as in this. He created a 3D panel model for the hull, and

calculated the radiation and diffraction pressures from first order potential theory for each panel using WAMIT. The hull was divided into sections and the pressure on each panel were integrated to generate the frequency-dependent added mass, damping and excitation forces for the sections. The method gave exact translational load component magnitudes and slightly underestimated rotational load component magnitudes compared to WAMIT's output for the hull as a whole. An equivalent beam model was created for the hull and implemented in a global model for the TLPWT. This was done to investigate the hull elasticity's influence on the system's global dynamic properties and internal loads. It was showed that the hull elasticity had significant impact on the vertical motions with natural periods in heave and pitch increasing by 43% and 18%, respectively. Time domain simulations were performed on the model and an attempt was made to investigate the dynamic amplification of internal loads in the hull. The results indicated unexpectedly large amplifications for certain frequencies and more research was needed to draw conclusions. The work done in his master thesis have been helpful since a lot of the same work have been done in this thesis. Modelling procedures have been similar to some extent, even though the designs are different in terms of substructure concepts and how complex the geometry are.

Borg [21] did a study about floating substructure flexibility of large-volume 10MW offshore wind turbine platforms in dynamic calculations. A different method compared to Svendsen [20] was used for capturing the elasticity effect in the hull for a FWT in coupled global analysis. The method involved the use of a radiation-diffraction solver to incorporate flexibility of large volume floating substructure within FWT dynamic calculations. Additional body deformations DOFs were used together with the conventional rigid body DOFs. All modes had a separate shape function that related the displacement of a panel on the body surface to the displacement in the mode. From this, the velocity potential could be determined with linearized boundary conditions at the seabed and free surface together with far-field boundary condition. The relevant hydrodynamic coefficients could then calculated to evaluate the dynamic response of a flexible structure. The method was implemented within a coupled simulation tool and applied to an artificially spar FWT. It was seen that the first substructure bending mode was coupled with the pitch motion. Motion in this flexible mode did not have significant effect on the global substructure and wind turbine response, but substantial forcing and excitation of this mode indicates that sectional loading within the substructure can be dependent on such motion. This study is useful for this master thesis for comparison reasons. The floating substructures are different, but the same DTU 10 MW reference wind turbine has been used. An idea for future work could be to use this method on the OO-Star Wind Floater Semi 10 MW and compare the results.

1.5 Report outline

This thesis will have the following outline:

- **Chapter 2:** A theoretical background on structural dynamics, environmental loads on a structure

with focus on the waves, and hydro-aero-servo-elastic coupling. Also, some theory regarding regular waves test and decay test are given.

- **Chapter 3:** A basic description of the OO-Star Wind Floater Semi 10MW design with main focus on the floating hull.
- **Chapter 4:** Description of the modelling procedures of the hydrodynamic models representing the OO-Star Wind Floater Semi 10MW. Discussion of results, discrepancies, and possible explanations from analyses performed on the models are also presented. Order of the models:
    1. Rigid body model using first order potential theory.
    2. Rigid body model using Morison's equation.
    3. Flexible beam model using Morison's equation.
    4. Flexible beam model using distributed loads from first order potential theory.
- **Chapter 5:** Conclusions and recommendations for future work.

2 Theoretical background

2.1 Strucutral dynamics

2.1.1 OO-Star wind floater semi-submersible with rigid body mechanics

A floating rigid-body has six motion modes, where three of them are translational degrees of freedom (DOF) and three of them are rotational DOFs. The translatory motions are commonly referred to as (1) surge, (2) sway and (3) heave, while the angular motions are referred to as (4) roll, (5) pitch and (6) yaw. The DOFs can be represented with a motion vector on the form:

$$\boldsymbol{\eta}(t) = [\eta_1(t), \eta_2(t), ..., \eta_6(t)]^T \tag{2.1}$$

Figure 2.1 shows the coordinate system and the DOFs for the semi-submersible used throughout this report. It is identical to the conventional definition in offshore wind with the origin fixed to the mean sea level (MSL) at centre of flotation of the floating platform in calm water in equilibrium position.

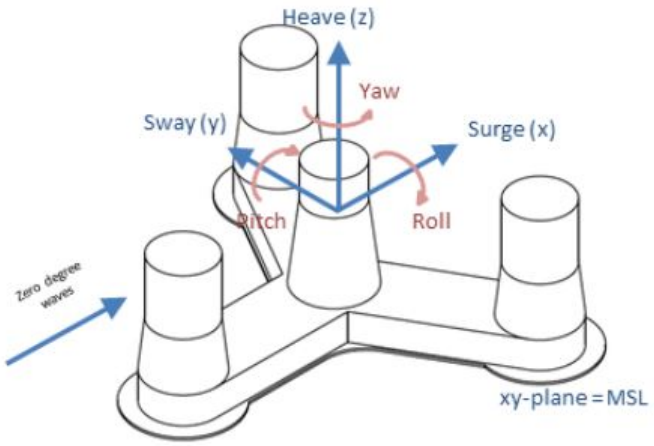

Figure 2.1: The OO-Star Wind Floater Semi 10MW coordinate system.

The equations of motion, which express the governing dynamic equilibrium by differential equations, needs to be established in order to say something about the motions of the floating body. The total inertia of the system can be divided into structural mass and hydrodynamic added mass. The total damping consist of hydrodynamic damping and aerodynamic damping. The total stiffness of the system have components from the hydrostatic restoring forces and moments, and the mooring system. By simplifying to only consider linear damping, restoring and excitation, the equations of motion can be written in matrix form as:

$$(\boldsymbol{M} + \boldsymbol{A})\ddot{\boldsymbol{\eta}} + \boldsymbol{B}\dot{\boldsymbol{\eta}} + (\boldsymbol{C} + \boldsymbol{K})\boldsymbol{\eta} = \boldsymbol{F} \tag{2.2}$$

F is a 6x1 load vector containing the external excitation forces acting on the structure in each mode of motion. M is the structural mass matrix, while A is the added mass matrix. B is the damping matrix, C is the hydrostatic restoring matrix and K is the mooring system restoring matrix. All the matrices are 6x6 due to the six degrees of freedom.

Some general information about the coefficients in the matrices is that the added mass, damping and stiffness coefficients in the matrices depend on the motion mode [22]. This means that the coefficients in heave are not necessarily the same as in surge. Also, all the coefficients can be significantly influenced by the body shape of the structure. The added mass and damping coefficients may also show a strong frequency dependence and therefore not being constant [22]. The hydrostatic restoring matrix will strongly depend on the water plane area and its second moment of inertia. The mooring system restoring matrix will be very different from which mooring system is used. A TLP mooring system will have large restoring stiffness, while a catenary mooring system will have small restoring stiffness. It is also important to remember that eq. (2.2) only give a linear description of the system. Nonlinear effects, such as wave-drift damping and viscous damping, are not included and additional terms would be needed to be added into the equation in order to account for these.

2.1.2 RIFLEX element formulation

One way to improve a dynamic model is to include elastic deflection characteristics. This could be obtained in various ways using beam, bar, shell and/or solid elements. RIFLEX, which is used in this thesis, allows the use of nonlinear beam elements. RIFLEX is a FEM software developed by MARINTEK for analysis of slender marine structure [23]. It is a nonlinear time-domain program that can account for large displacements and rotations. The beam elements are based on Euler-Bernoulli beam theory with an added shear deformation term. RIFLEX can account for nonlinear stiffness relationships, and the user can define such data as inputs. A brief description of the beam element formulation and the solving of the dynamic equilibrium equation in RIFLEX follows in the next paragraphs.

RIFLEX beam element formulation

The beam element in RILFLEX is formulated using the concept of co-rotated ghost reference system [24]. In short, this means that no transformation of the strain and stress components is necessary and large rotational deformations are allowed. The beam element has three translational and three rotational degrees of freedom at each node, see Figure 2.2. The following assumptions are made for the beam element:

- A plane section of the beam initially normal to the longitudinal axis, remains plane and normal after deformations.

- Lateral contraction caused by axial elongation is neglected.
- The strains are small.
- No shear deformations due to lateral loading (accounted for by modifying the bending stiffness).
- No coupling effects between torsion and bending in the stiffness matrix (accounted for by a second order approximation of torsion and bending curvature).

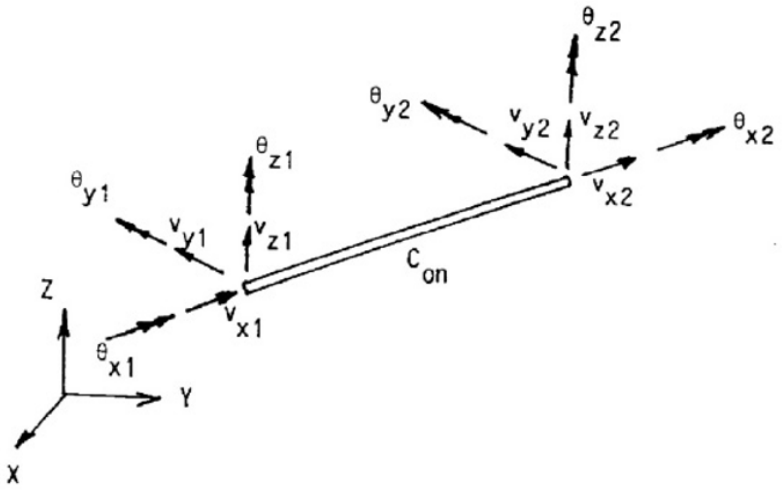

Figure 2.2: Nodal degrees of freedom for a RIFLEX beam element [24].

Solving the governing dynamic equilibrium in RIFLEX

The total number of degrees of freedom will in general be higher for a dynamic model made of RIFLEX beam elements compared to a single rigid body. They are contained in the motion vector, same as for a rigid model. The mass matrices for each element are gathered in a global mass matrix [24]. The global mass matrix is consistent, which means that it is based on the same interpolation polynomials as the stiffness matrix [25]. The global damping matrix consist of contributions from structural damping and hydrodynamic damping. Structural damping is Rayleigh damping, which is mass- and stiffness-proportional damping. The Newton-Raphson iteration procedure is used for the numerical time integration of the dynamic equilibrium equations. This involves that the mass, damping and stiffness matrices are recalculated at each iteration cycle.

2.1.3 Dynamic response of a single and multi degree-of-freedom system

The equation of motion for a multi degree of freedom (MDOF) system can be given as

$$\boldsymbol{M}\ddot{\boldsymbol{r}} + \boldsymbol{C}\dot{\boldsymbol{r}} + \boldsymbol{K}\boldsymbol{r} = \boldsymbol{Q}(t) \tag{2.3}$$

where $\boldsymbol{M}$ is the mass matrix, $\boldsymbol{K}$ is the stiffness matrix and $\boldsymbol{C}$ is the damping matrix where viscous damping is assumed [25]. $\boldsymbol{Q}$(t) is the loading matrix and is assumed to be deterministic. The solution to the

equation of motion can be given in two different ways. One way is a solution in the time domain, the other way is in the frequency domain. The solution in the time domain is given directly as a function of time. This will normally be used if the the loading is deterministic and given as a function of time. Figure 2.3 shows an illustration of the solution in the time domain. Further explanation of the solution in the time domain will not be discussed.

The solution in the frequency domain starts of by expressing an arbitrary excitation by a infinite sum of harmonic components. Mathematically, this is known as the Fourier transformation which is explained in section 2.1.4. The harmonic components will be a function of the frequency ω and expresses the excitation in the frequency domain. The response can be transformed in similar way as the excitation into the frequency domain. The equation of motion (2.3) can therefore be solved in frequency domain by solving for harmonic loading for various frequencies. An advantage of this solution is that it shows directly how sensitive a structure is to different load frequencies. This solution is therefore suited for structures with frequency-dependent mass, damping or stiffness matrix, or non viscous damping model. It is also a preferred solution for analysis of response to stochastic loads.

The equation of motion (2.3) is formulated as a coupled equation system. Solving this either in the time domain or the frequency domain is known as a direct method. Alternatively, the equation of motion 2.3 can be transformed into an uncoupled system, and solved separately. The frequency-response method, which is a direct method, will be explained in the following section, while the uncoupled system will not be further discussed.

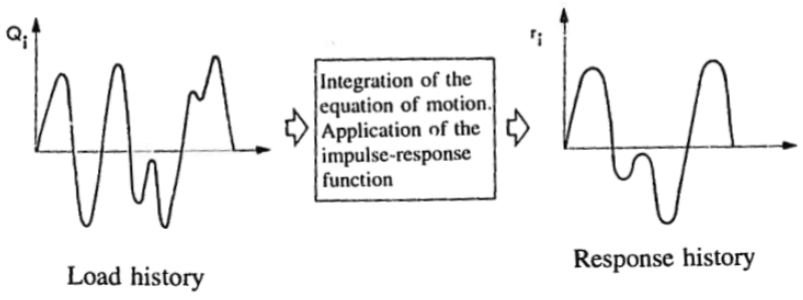

Figure 2.3: Figure illustrating the solution in the time domain [25].

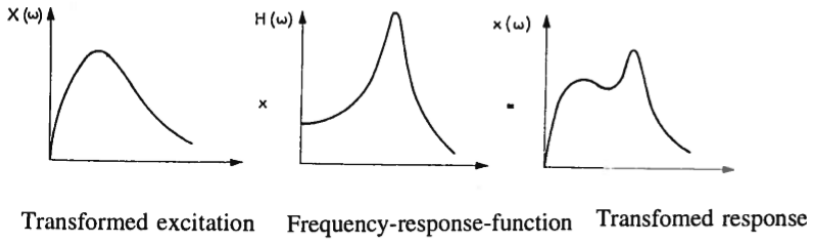

Figure 2.4: Figure illustrating the solution in the frequency domain [25].

The frequency-response method

The method will first be explained for a single degree-of-freedom (SDOF) system, later a multi degree-of-freedom (MDOF). The solution for a harmonic loading can be represented as a complex vector [25]

$$e^{i\omega t} = cos\omega t + isin\omega t \tag{2.4}$$

The load can be written as

$$Q = Xe^{i\omega t} (= Xcos\omega t) \tag{2.5}$$

where it is implicitly understood that it is meant as the real part. X is a complex number and represents the load in the frequency domain. The equation of motion can then be written as

$$m\ddot{u} + c\dot{u} + ku = Xe^{i\omega t} \tag{2.6}$$

The particular solution to this equation will also be harmonic

$$u = xe^{i\omega t} = H(\omega)Xe^{i\omega t} \tag{2.7}$$

where the real part is implied as for the load. Inserting the particular solution into the equation of motion (2.6) gives

$$\begin{aligned} H(\omega) &= \frac{1}{-m\omega^2 + i\omega c + k} \\ &= \frac{1}{m(\omega_0^2 - \omega^2 + i2\lambda\omega\omega_0)} \\ &= \frac{1}{k(1-\beta^2 + i2\lambda\beta)} \end{aligned} \tag{2.8}$$

where ω_0 is the natural frequency, β is the frequency ratio (ω/ω_0) and $H(\omega)$ is the complex frequency-response function. Figure 2.5 shows an example of the real and imaginary part of $H(\omega)$ normalised by the static displacement $H(0)$. The real part is the component of the response which is in-phase with the excitation, and the imaginary part is the component of the response which is $\pi/2$ out-of-phase. Important to notice that the imaginary part will dominate at resonance (β=0) and the real part changes sign and will be in opposite phase to the excitation. The dynamic amplification factor (DAF) is defined

as the ratio between the dynamic and static displacement

$$DAF = \frac{(u_{max})_{dyn}}{(u)_{stat})} = \frac{|H(\omega)|}{H(0)} = \frac{1}{((1-\beta^2)^2 + (2\lambda\beta)^2)^{\frac{1}{2}}} \tag{2.9}$$

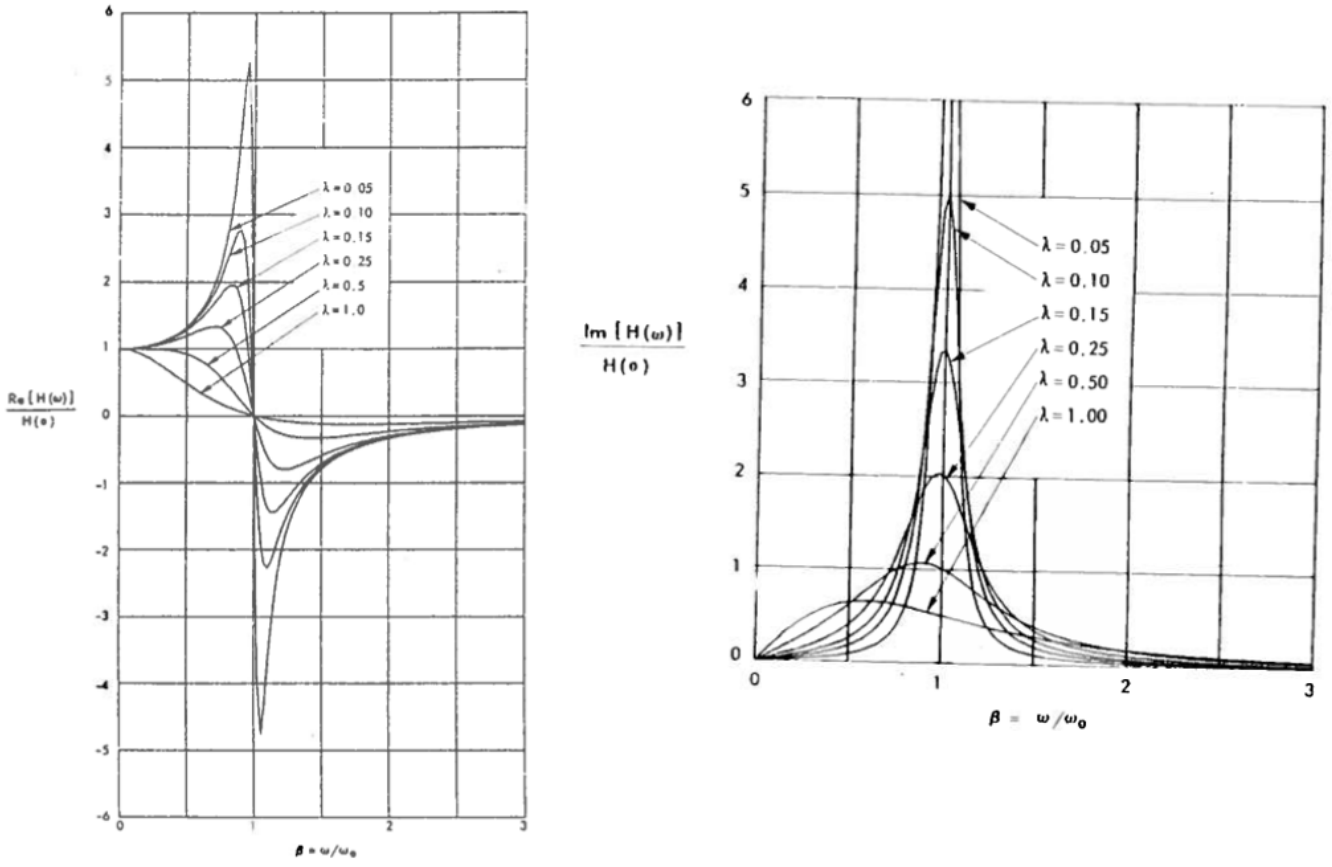

Figure 2.5: An example of the real and imaginary part of $H(\omega)$ as a function of the frequency ratio β [25].

The complex response function $H(\omega)$ can be written in polar form as

$$H(\omega) = |H(\omega)|e^{-i\theta} = |H(\omega)|(cos\theta - isin\theta) \tag{2.10}$$

which gives

$$\theta = arctan\frac{Im[H(\omega)]}{Re[H(\omega)]} = arctan\frac{2\lambda\beta}{1-\beta^2} \tag{2.11}$$

The solution can then be written as

$$u = XRe[|H(\omega)|e^{-i\theta}e^{i\omega t}] = X|H(\omega)|cos(\omega t - \theta) \tag{2.12}$$

An arbitrary periodic loading with a given period can written as a sum of harmonic loads as mentioned earlier. This is called a Fourier series. The response to each harmonic component is solved as mentioned

above, and the solution is then obtained by summing the contributions from all the frequencies. If the loading is aperiodic the Fourier transformation is used. The solution in the frequency domain can then be written as

$$x(\omega) = H(\omega)X(\omega) \tag{2.13}$$

$x(\omega)$ is usually complex and expresses both the amplitude magnitude and the phase angle.

Now, lets consider a multi degree-of-freedom (MDOF) system. An arbitrary component of a harmonic loading can be written as

$$\begin{aligned} Q_j(t) &= Q_{0j}e^{i(\omega t+\alpha_j)} \\ &= Q_{0j}(cos\alpha_j + isin\alpha_j)e^{i\omega t} \end{aligned} \tag{2.14}$$

where Q_{0j} is the amplitude value for the j'th component, ω is the frequency of the load and α_j is the phase angle of the j'th component. By introducing the complex load vector $\boldsymbol{X}$ with components

$$X_j = Q_{0j}(cos\alpha_j + isin\alpha_j) = X_{Rj} + iX_{Ij} \tag{2.15}$$

the dynamic equilibrium equation with viscous damping can be written as

$$\boldsymbol{M\ddot{r} + C\dot{r} + Kr = Xe^{i\omega t}} \tag{2.16}$$

The particular solution to this equation can be given as

$$\boldsymbol{r = xe^{i\omega t}} \tag{2.17}$$

where the complex response vector $\boldsymbol{x}$ is determined by the equation system

$$\begin{aligned} [\boldsymbol{K - \omega^2 M + i\omega C}]\boldsymbol{x} &= \boldsymbol{X} \\ \boldsymbol{Bx} &= \boldsymbol{X} \end{aligned} \tag{2.18}$$

where $\boldsymbol{B}$ is a complex symmetric and banded matrix. This gives a system of equations that can be solved by complex arithmetic. By introducing the complex frequency-response function

$$\boldsymbol{H(\omega)} = \frac{1}{[\boldsymbol{K - \omega^2 M + i\omega C}]} \tag{2.19}$$

the solution can be written as

$$\boldsymbol{x(\omega) = H(\omega)X(\omega)} \tag{2.20}$$

Each component $H_{ij}(\omega)$ of the matrix $\boldsymbol{H(\omega)}$ is a transfer function for the response at d.o.f i due to a harmonic load with unit amplitude at d.o.f j at a given frequency. $\boldsymbol{H(\omega)}$ can be determined by solving eq. (2.18) repeatedly for different frequencies and setting $\boldsymbol{X}$ equal to the identity matrix.

2.1.4 Time domain and frequency domain

A brief introduction to the connection between the time domain and frequency domain. The two domains are different ways to describe processes and performing dynamic analyses. The connection between them is commonly known as the Fourier transform (and inverse Fourier transform) and it makes it possible to switch between the time domain and the frequency domain. The Fourier transform decomposes a function of time into the different frequencies that make it up [26]. An illustration of this can be seen in Figure 2.6 which will be further discussed later on. The function itself is a complex function of frequency. The absolute value of the function gives the amount of that frequency in the original function, and the complex argument gives the phase offset. The formal definition of the Fourier transform is given by

$$X(\omega) = \frac{1}{2\pi}\int_{-\infty}^{\infty} x(t)e^{-i\omega t}dt \tag{2.21}$$

where x(t) is the function of time and ω is the frequency. The calculations in the Fourier transform is time consuming for a computer to perform due to a large number of calculations needed. An algorithm have been developed to make the computation more efficient. This algorithm is known as the fast Fourier transform (FFT), and is based on the constant time increments and frequency intervals [27]. Further details of FFT will not be described here.

The connection between the time domain and frequency domain is used for statistical description of waves. Irregular sea and statistical estimates can be obtained by using linear theory [22]. An important consequence of using linear theory is that superposition principle is valid, which means that the problem can be split into single elements. The wave elevation of a long-crested irregular sea propagating along the positive x-axis can then be written as the sum of a large number of wave components as

$$\zeta = \sum_{j=1}^{N} A_j sin(\omega_j t - k_j x + \epsilon_j) \tag{2.22}$$

where A_j is the wave amplitude, ω_j is the circular frequency, k_j is the wave number and ϵ_j is the random phase angle for wave component number j. The relationship between ω_j and k_j are given by the dispersion relationship (equation 2.39). The random phase angles ϵ_j are uniformly distributed between 0 and 2π and constant with time. The wave amplitude A_j are connected to the wave spectrum $S(\omega)$ as

$$\frac{1}{2}A_j^2 = S(\omega)\Delta\omega \tag{2.23}$$

where $\Delta\omega$ is a constant difference between successive frequencies. So, if the wave spectrum is known, then it's possible to make a realization by inverse Fourier transform formally given by eq. (2.22) and (2.23). It's common to assume that the wave process is stationary and ergodic. Other common assumptions are that the instantaneous wave elevation is Gaussian distributed with zero mean and variance

equal to $\int_0^\infty S(\omega)d\omega$, which can be shown [28]. This means that the response to irregular waves can be obtained by studying the sum of responses to regular waves. The connection between the frequency domain represented by a wave spectrum and a time domain solution of the waves is illustrated by Figure 2.6.

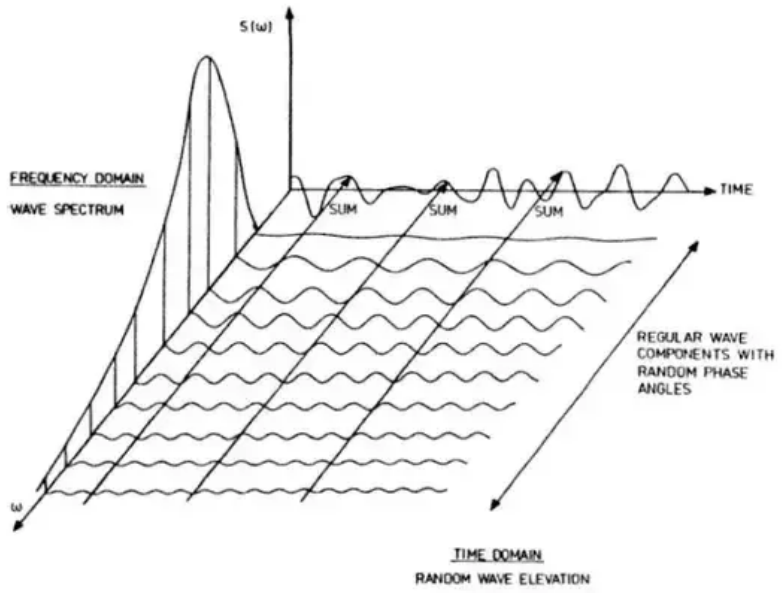

Figure 2.6: Figure illustrating the connection between a frequency domain and time domain representation of waves in a long-crested short term sea state [22].

.

2.1.5 Response amplitude operator (RAO)

For model test results it is convenient to transform measured time series from the time domain to the frequency domain in order to analyse the results. This section will be a short explanation about the different steps from a measured time history to obtain the Response Amplitude Operator (RAO). The connection to regular waves test will also be explained.

A common way to transform a measured time history signal x(t) into the frequency domain is a spectral analysis [29]. This analysis is usually done by the Fast Fourier transform (FFT) technique, which obtain the spectral density of the signal.

It's assumed that the process takes place over the time interval (0<t<T) when T$\rightarrow \infty$. The power spectrum of x(t), denoted as $S_{xx}(\omega)$, is defined as the Fourier transform of the auto correlation function $R_{xx}(\tau)$

$$S_{xx}(\omega) = \int_{-\infty}^{\infty} R_{xx}(\tau) e^{-i\omega\tau} d\tau \tag{2.24}$$

The cross spectrum between two signals, x(t) and y(t) where x(t) is the reference signal (wave elevation) and the y(t) is the measured response (body motion), is defined as

$$S_{xy}(\omega) = \int_{-\infty}^{\infty} R_{xy}(\tau) e^{-i\omega\tau} d\tau \tag{2.25}$$

The linear transfer function between the response and input can then be found as

$$H(\omega) = \frac{S_{xy}(\omega)}{S_{xx}(\omega)} \tag{2.26}$$

$H(\omega)$ is the complex transfer function. The RAO is defined as the modulus of $H(\omega)$ and the phase $\epsilon(\omega)$ is defined as the phase angle of $H(\omega)$. Alternatively the RAO can be calculated from the input and response spectrum directly as

$$|H(\omega)|^2 = \frac{S_{yy}(\omega)}{S_{xx}(\omega)} \tag{2.27}$$

By using this formulation no information about the phase $\epsilon(\omega)$ is obtained. Figure 2.7 shows an illustration of the relation between the input spectrum, the transfer function and the response spectrum.

The RAO for a structure can be determined in several ways. One way is the regular wave tests, where regular incident waves with a given frequency ω are generated in each test and the motions and loads are measured [29]. It's important that the steepness of the waves are small enough so linear theory is valid. The given frequency for the waves in each test is varied to cover the relevant range for body motions. Mathematically, this is done by making harmonic input wave signal

$$x(t) = X_A sin(\omega_1 t) \tag{2.28}$$

where X_A is the wave amplitude and ω_1 is the wave frequency. Assuming linear system the measured response signal y(t) will also be harmonic. The response amplitude Y_A is found from maxima and minima of the y(t) signal. The phase angle is found from the phase lag between x(t) and y(t). The RAO (or transfer function) is then defined as the ratio between the response amplitude and the input wave amplitude

$$RAO = \frac{Y_A}{X_A} \tag{2.29}$$

In practise, the input wave may not be completely harmonic and the system may have non-linearities.

This is usually solved by Fourier analysis of the measured results. The Fourier analysis gives the amplitude and phase of the different harmonic components, Y_i and ϵ_i. The fundamental component is at the wave frequency ω_1 and the higher order components are at frequencies ω_n = nω_1, n=2,3,... The RAO's will now be defined as the ratio between the fundamental component of the measured response and the wave

$$RAO = \frac{Y_1}{X_1} \tag{2.30}$$

There are a lot of challenges connected to performing regular wave tests for a model in real life. Examples of this are that the generated waves a sufficiently close to sinusoidal, that the waves a stable and stationary long enough to obtain steady state body motions, waves not to steep and many more. Luckily, these challenges are not a problem for simulations of regular wave tests for a model in a computer program, which is the case in this thesis.

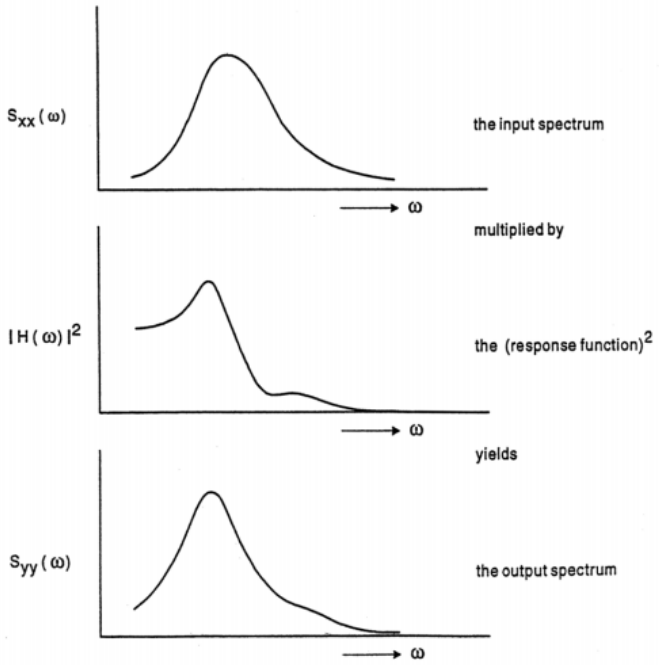

Figure 2.7: Figure illustrating the connection between a frequency domain and time domain representation of waves in a long-crested short term sea state [22]

.

2.2 Environmental loads

An offshore wind turbine will experience a lot of different environmental loads. An illustration of some of these loads are shown in Figure 2.8. The focus in this report will be the implementation of the hydrodynamic loads induced by waves. Hydrostatic loads will be considered to a certain degree. Other

environmental loads, such as aerodynamic, current and tides, ship and ice impact, marine growth etc will not be further discussed in this report.

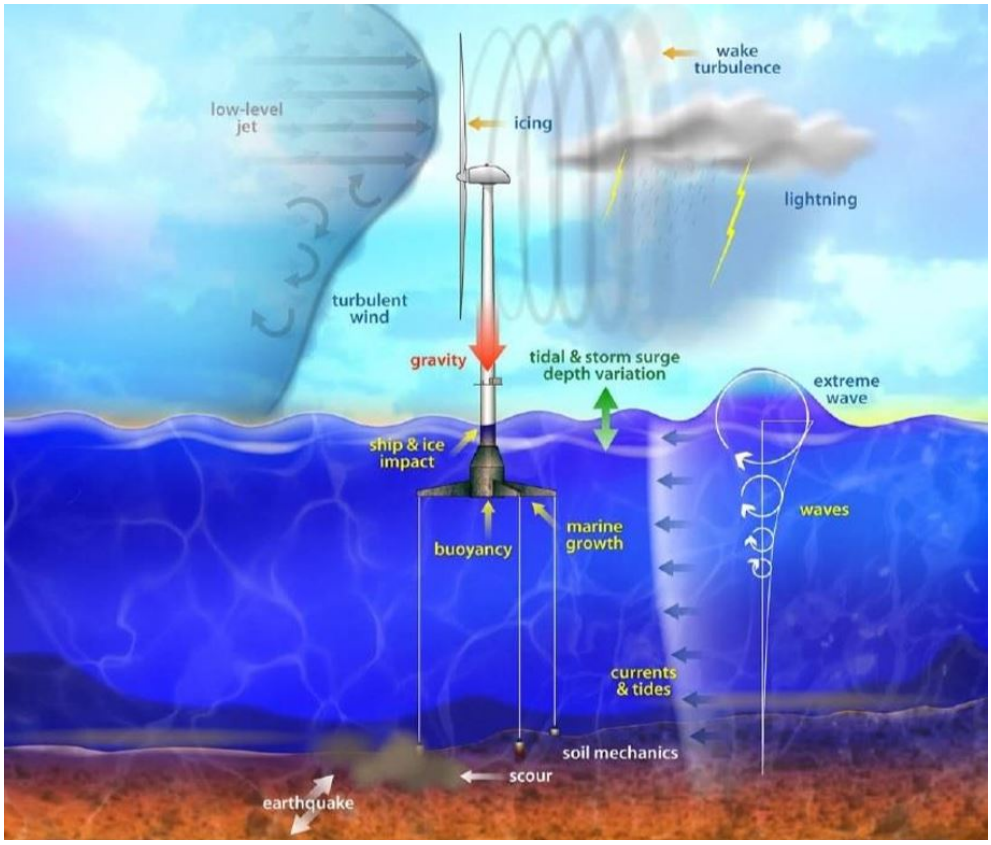

Figure 2.8: Load sources on a floating wind turbine [30].

2.3 Hydrodynamic loads

2.3.1 Potential flow theory

Linear theory can, to a large extent, represent the wave induced motions and loads on semi-submersibles, ships and other large volume structures [22]. Linear theory means that the wave induced motions and loads on a structure are linearly proportional to the amplitude of the incoming wave. Linear wave theory also implies that the wave steepness, which is the wave amplitude divided on the wave length, is small i.e. the waves are far from breaking. Also, the wave kinematics are only valid up to the mean water level. Potential flow theory, which describes the velocity field in a fluid as a gradient of a scalar function; the velocity potential ϕ, is assumed to be representative for the fluid in this study. The assumptions behind potential flow theory to be valid for a fluid are the triple i's: inviscid, irrotational and incompressible [31].

Results from a structure in irregular seas can be obtained by linearly superimposing results from regular wave components. This means that it is good enough from a hydrodynamic point of view to analyze a

structure in incident sinusoidal waves with small wave steepness [22]. The hydrodynamic problem in regular waves are usually divided into two sub-problems which is illustrated in Figure 2.9:

- The diffraction problem, which is the forces and moments on the body when the structure is fixed from oscillating and there are incident regular waves. The hydrodynamic loads, which causes the forces and moments, are called wave excitation loads and divided into Froude-kriloff and diffraction forces and moments.
- The radiation problem, which is the forces and moments on the body when the structure is forced to oscillate with wave excitation frequency in any rigid-body motion mode. There are no incident waves and the hydrodynamic loads are divided into added mass, damping and restoring terms.

This implies that the total velocity potential, ϕ_{tot}, can be divided into two components, one for the diffraction problem and one for the radiation problem, due linearity.

$$\phi_{\text{tot}} = \phi_{\text{diff}} + \phi_{\text{rad}} \tag{2.31}$$

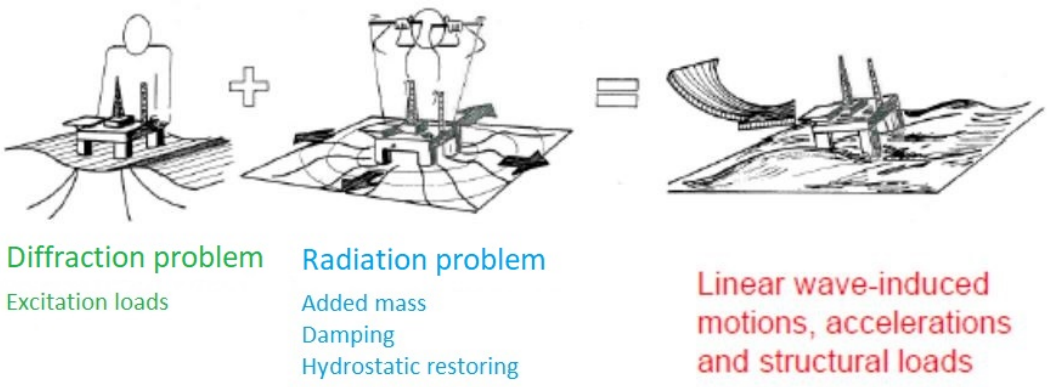

Figure 2.9: Superposition of wave excitation, added mass, damping and restoring loads [31].

The diffraction problem

As mentioned before, the forces and moments on the structure when it is fixed from oscillating and there is incident waves are called wave excitation loads [22]. These loads can be explained by dividing the unsteady fluid pressure into two different effects. One effect is the unsteady pressure induced by the undisturbed incident waves. The loads from this pressure field is called Froude-Kriloff loads. The second effect is the change in the pressure field due to the presence of the structure. These loads are called diffraction loads and may be found in similar way as the added mass and damping coefficients. An illustration of the two effects is shown in Figure 2.10.

$$\phi_{\text{diff}} = \underbrace{\phi_0}_{\text{incident wave}} + \underbrace{\phi_D}_{\text{diffraction}} \tag{2.32}$$

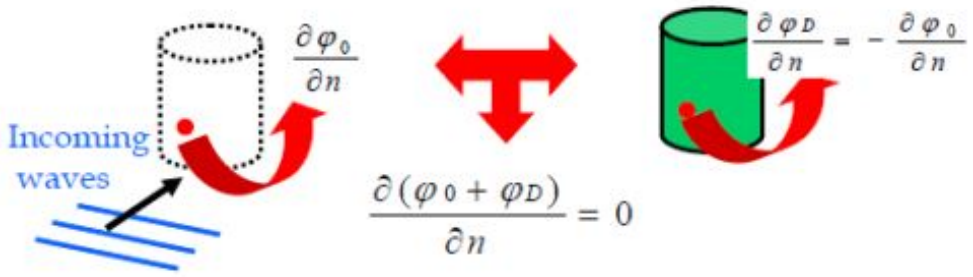

Figure 2.10: Splitting of the diffraction problem [31]

The calculations of the velocity potential for the diffraction problem starts with dividing the potential into the two components, one for the incident waves and one for the diffraction waves. The incident waves potential, ϕ_0, acts like the body was not there. These hydrodynamic loads are the Froude-Krillof loads. To recover the body impermeability and satisfy the impermeability condition, the body presence causes a velocity potential, which again causes waves called diffraction waves, known as ϕ_D. These hydrodynamic loads are the diffraction loads.

The sum of these two loads gives the wave excitation loads. These are calculated by integrating, respectively, the incident-wave dynamic pressure and the diffraction dynamic pressure along the mean wetted hull surface, S_{0B}:

$$F_{\text{exc,k}}(t) = \underbrace{-\int_{S_{0B}} \rho \frac{\partial \phi_0}{\partial t} n_k dS}_{\text{Froude-Kriloff loads}} \underbrace{-\int_{S_{0B}} \rho \frac{\partial \phi_D}{\partial t} n_k dS}_{\text{diffraction loads}} \tag{2.33}$$

where ρ is water density and n is the normal vector. The pressure in the fluid, p, are found from the Bernoulli equation [22]. It consist of three different terms, the static, linear dynamic and quadratic dynamic pressure.

$$p - p_a = \underbrace{-\rho g z}_{\text{static}} \underbrace{-\rho \frac{\partial \phi}{\partial t}}_{\text{dyn.lin.}} \underbrace{-\frac{1}{2}\rho |\nabla \phi|^2}_{\text{dyn.quad.}} \tag{2.34}$$

The radiation problem

The velocity potential component from the radiation problem can be split into six sub-problems, one for each degree of freedom for a floating rigid body (surge, sway, heave, roll, pitch and yaw):

$$\phi_R = \text{Re}\left\{ \sum_{j=1}^{6} \dot{\eta}_j \phi_j \right\} \tag{2.35}$$

where $\dot{\eta}_j$ are the velocity in mode j and ϕ_j are the complex velocity potential for the body oscillating in the j-th mode. The moving body generate waves, known as radiated waves, when it's forced to oscillate

with the wave excitation frequency. These waves are associated with the radiation velocity potential and the hydrodynamic loads on the body are recognized as the added-mass, damping and restoring terms. The restoring terms are connected to the buoyancy and will be discussed in the hydrostatic loads section. The added-mass and damping terms are connected with the dynamic pressure made by the moving body, i.e:

$$F_{\text{rad,k}}(t) = -\int_{S_{0B}} \rho \frac{\partial \phi_R}{\partial t} n_k dS = \sum_{j=1}^{6} \{-A_{kj}\ddot{\eta}_j - B_{kj}\dot{\eta}_j\} \quad k = 1,..,6 \tag{2.36}$$

with the added-mass (A_{kj}) and damping (B_{kj}) coefficients as:

$$A_{kj}(\omega) = \text{Re}\left\{\rho \int_{S_{0B}} \phi_j n_k dS\right\} \quad B_{kj}(\omega) = -\omega\,\text{Im}\left\{\rho \int_{S_{0B}} \phi_j n_k dS\right\} \tag{2.37}$$

Panel methods

The hydrodynamic solver Wadam was used in HydroD for calculating the wave-structure interaction for the OO-Star Wind floater Semi 10MW. Wadam solves the hydrodynamic problem in the frequency domain and finds the frequency-dependent added-mass coefficients, damping coefficients and wave excitation. Wadam uses 3D radiation-diffraction theory employing a panel model (created by GeniE/HydroD). A brief description of panel methods will be presented here.

Panel methods are numerical methods for calculating the linear wave-induced motions and loads on a structure. The problem to be solved is to obtain the the correct velocity potential when the structure is a complicated 3D structure. There exist several different panel methods, such as the source technique or using Green's second identity, but they are all based on potential theory. The surface of the structure is divided into discrete elements, which is called panels. Each of them fulfill the Laplace equation with boundary conditions from the structure [22]. The different methods have different approaches in order to find the velocity potential. For panel methods that are based on Green's second identity, the 3D Laplace equation is transformed into a 2D surface integral equation. The discretized panels makes it possible to solve this surface integral numerically.

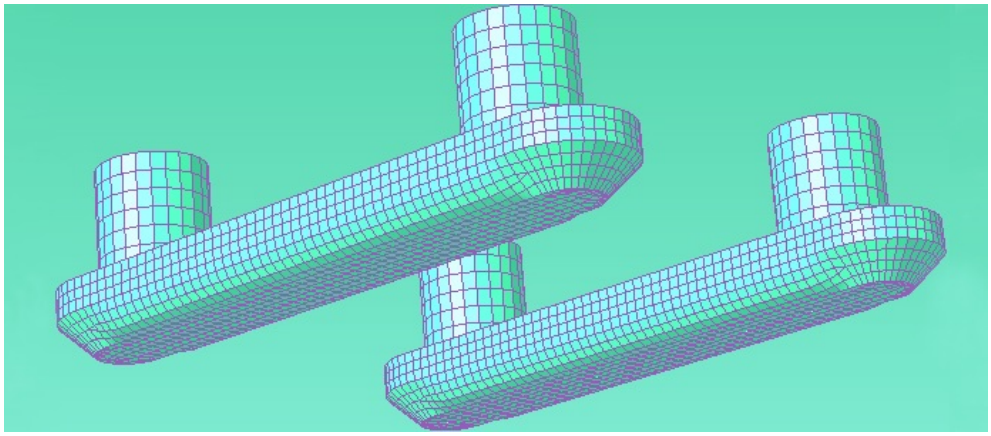

Figure 2.11: Illustration of grid for potential flow panel method [32].

Panel methods are the most common techniques used to analyze the linear steady state response of large-volume structures in regular waves [22]. Panel methods are based on potential theory and therefore the effect of flow separation is neglected. This means that they should not be applied to slender structures like jackets, riser etc. The methods can also only predict damping due to radiation of surface waves and motions where viscous effect are important will therefore be inaccurate.

2.3.2 Morison's equation

Morison's equation is often used to calculate the wave forces on a structural part with circular cross section [33]. It can be written in a lot of different ways, but the most basic consist of two terms known as the mass force and the viscous drag force. The mass force is based on potential theory and is proportional to the undisturbed fluid acceleration $\dot{u}$. The mass force can be further extended to two terms if the body is moving. These terms are known as Froude–Krylov force and hydrodynamic mass force. The horizontal force dF on a unit length of circular cross section can be calculated according to Morison's equation as:

$$dF = \underbrace{\rho\frac{\pi}{4}D^2\dot{u}}_{\text{Froude–Krylov}} + \underbrace{\rho C_a\frac{\pi}{4}D^2(\dot{u}-\dot{v})}_{\text{Hydrodynamic mass}} + \underbrace{\frac{1}{2}\rho C_d D|u-v|(u-v)}_{\text{Drag}} \tag{2.38}$$

where ρ is the water density, D is the cylinder diameter and u and $\dot{u}$ are the horizontal undisturbed fluid velocity and acceleration at the mid point of the strip. v and $\dot{v}$ are the velocity and acceleration of the cross section. C_a and C_d are the added mass and drag coefficients, respectively. These coefficients are dependent on many parameters, such as Reynolds number and Keulegan-Carpenter number, and are therefore determined empirically [22]. Positive force direction is in the wave propagation direction. It is assumed that the wave length is relatively large compared to the diameter of the cylinder. Morison's equation do not account for diffraction effects and the wavelength should be five times the diameter as a rule of thumb for Morison's equation to be valid. For smaller wave lengths can the linear analytical solution by McCamy Fuchs be used which is valid for arbitrary wave lengths. This theory is based on

potential flow and is valid for a circular cylinder fixed to the sea floor and penetrating the free-surface [22]. Figure 2.12 shows which forces are important for different wave length-diameter ratios for a fixed cylinder.

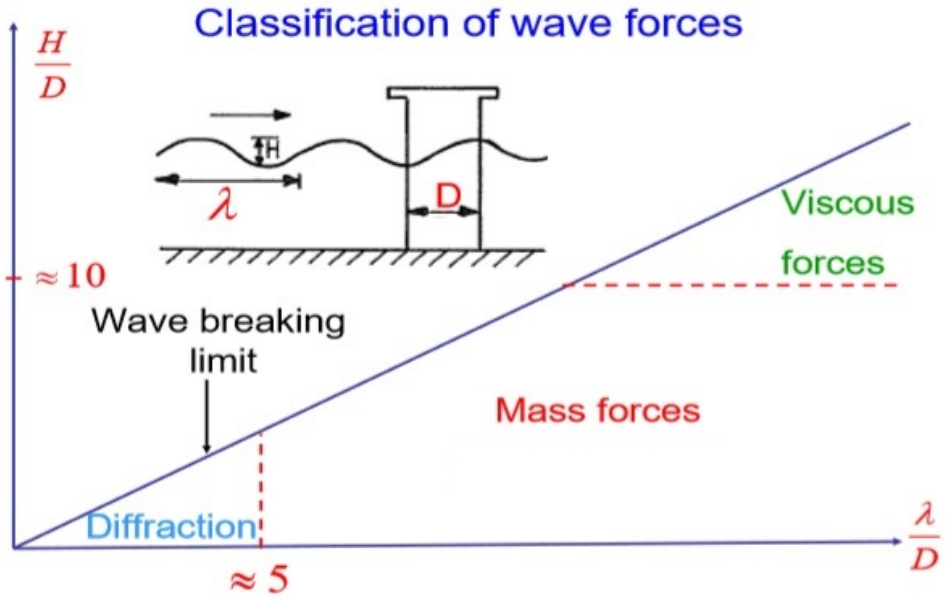

Figure 2.12: Relative importance of mass, viscous drag and diffraction forces on marine structures [22].

Lets assume regular sinusoidal waves, deep water conditions and constant mass and drag coefficients with respect to water depth. Then it can be shown that the mass force in Morison's equation reduces with depth as $e^{2/\lambda}$, where z is the vertical coordinate. The drag force reduces with depth as $e^{4/\lambda}$, and is therefore more concentrated around the free surface. The mass force on a strip will have absolute maximum value when a rest position of the wave is on the cylinder axis (x=0). The drag force will be zero. The drag force on a strip will have absolute maximum value when a wave top is on the cylinder axis.

The largest diameter part of the outer columns of the floating substructure to OO-Star Wind Floater Semi 10MW is 15.8 m, hence, the wave length needs to be larger than 79 m for Morison's equation to be valid. The dispersion relation, which gives the relation between the circular frequency, ω, the wave number, k, and the water depth ,h, is used to calculate the wave length ,λ:

$$\omega^2 = kg \tanh kh \tag{2.39}$$

$$k = \frac{2\pi}{\lambda} \tag{2.40}$$

Several sea states have been tested in the D4.2 report [15] with significant wave heights and peak periods varying from 1.67-8.31m and 8-12 s, respectively. The water depth is given as 130 m, and by solving

the dispersion relation equation, the wave number k = 0.0280-0.0629m^{-1} assuming wave periods to be between wave peak periods. This corresponds to wave length λ = 100-224 m. Since the possible wave lengths are larger than 79 m, Morison's equation is assumed to be valid. However, the assumption of wave periods to be between wave peak periods may be a inaccurate assumption. Also, in irregular sea states there may be a significant portion of shorter waves than the waves considered here and therefore will the Morison equation not be valid in that case. Also, the fact that there are several columns in the water plane will affect the water around the floating platform and hence, less suitable for using Morison equation.

2.3.3 Comparison of hydrodynamic models

Two common options for calculating the hydrodynamic loads in a global analysis are potential flow theory and Morison's equation. In this thesis have first-order potential flow theory been used, which gives the linear solution. In the linear solution, both the free-surface condition and body boundary condition are satisfied on the mean position of the free-surface and the submerged hull surface, respectively[22]. In addition, the fluid pressure and velocity of fluid particles on the free-surface are linearized. By using a panel method solution are the Froude-Krylov forces and diffraction effects for large volume structures accounted for. This results in a linear solution which is frequency-dependent. Morison's equation is another calculation method for calculating wave loads on slender structures. It is a semi-empirical method, and is equivalent to the potential flow solution for a fixed cylinder which is slender and viscous effects are negligible [22]. Slender means that the wavelength-diameter ratio is large. Morison's equation do not account for diffraction effects. The formulation of Morison's equation contains quadratic drag force and relative velocities and accelerations. It is therefore solved in the time domain with frequency-independent coefficients.

The starting point to compare the hydrodynamic models is best illustrated by considering a single degree-of-freedom (SDOF) system. With potential flow theory including viscous drag this can be written as[34]:

$$(M + A_\infty)\ddot{x}(t) + \int_{-\infty}^{\infty} \kappa(t-\tau)\dot{x}(\tau)d\tau + Cx(t) + K(x(t)) = F^{FK} + F^D + C_q|u - \dot{x}|(u - \dot{x}) \tag{2.41}$$

where M is the mass, A_∞ is the added mass for high frequencies, and x, $\dot{x}$ and $\ddot{x}$ are the system displacement, velocity and acceleration, respectively. $\kappa(t-\tau)$ is the retardation function accounting for frequency added mass and damping, C is the hydrostatic stiffness and K(x(t)) is the nonlinear restoring forces from the mooring system. C_q is the quadratic damping term to approximate viscous effects, u is the water particle velocity, F^{FK} is the Froude-Krylov force and F^D is the diffraction force. The same system described by Morison's equation, same quadratic damping and no retardation function, can be

written as [34]:

$$M\ddot{x} + Cx(t) + K(x(t)) = (\rho_w V + m_a)\dot{u} - m_a\ddot{x} + C_q|u - \dot{x}|(u - \dot{x}) \tag{2.42}$$

where ρ_w is the water density, V is the displaced water volume, m_a is a constant added mass and $\dot{u}$ is the water particle acceleration. By comparing eq. (2.41) and (2.42) it can be seen that it is possible to adjust Morison's equation coefficients to obtain the same results from both equations for a SDOF system in regular waves with a given frequency with constant amplitude. A weakness of the Morison model compared the potential flow model is that it cannot necessarily capture the equivalent hydrodynamic coupling effects for a multi degree-of-freedom (MDOF) system. Also, the frequency-dependence and linear damping is lost in the Morison model. A weakness of the potential flow model is that it does not consider the water particle accelerations above the waterline, and requires solving the Cummins equation, which can results in some computational cost. Applying Morison's equation makes it possible to account for non-linear effects from calculating the wave forces in the instantaneous position of the floater. These effects could potentially be important. The main reason for neglecting higher-order potential flow theory loads in this study is to not make the assignment more difficult. First-order potential theory can represent the loads to a large extent, and higher-order potential flow theory are left to future work.

2.3.4 Hydrostatic loads

The hydrostatic loading on a submerged body is the hydrostatic pressure from the fluid at rest. The linear hydrostatic pressure, which is the first term in the Bernoulli equation (2.34), depends only on the depth z. This pressure can for deep submerged parts result in a significant compressive load which can be important design factor in terms of buckling of shells and plates.

The hydrostatic pressure also gives an important contribution in terms of restoring forces and moments. It is the pressure difference over and under a floating structure that gives the buoyancy and the hydrostatic pressure is the main difference. So in general, the hydrostatic pressure is important for the buoyancy and stability of a floating structure, and particularly for freely floating structures. For a rigid floating structure with six degrees of freedom (surge, sway, heave, roll, pitch and yaw), there will only be non-zero coefficients for heave, roll and pitch in the hydrostatic stiffness matrix [22]. For a freely floating body we can write the force and moment components as:

$$F_k = -C_{kj}\eta_j \qquad k, j = 1, .., 6 \tag{2.43}$$

This defines the restoring coefficients C_{kj}. If the body has the x-z plane as symmetry plane for the submerged part, the non-zero restoring coefficients are:

$$C_{33} = \rho g A_{WP} \tag{2.44}$$

$$C_{35} = C_{53} = -\rho g \int_{A_{WP}} x ds \tag{2.45}$$

$$C_{44} = \rho g V (z_B - z_G) + \rho g \int_{A_{WP}} y^2 ds = \rho g V \overline{GM_T} \tag{2.46}$$

$$C_{55} = \rho g V (z_B - z_G) + \rho g \int_{A_{WP}} x^2 ds = \rho g V \overline{GM_L} \tag{2.47}$$

where A_{WP} is the waterplane area, V is the displaced volume of water, z_B and z_G are the vertical coordinates from the centre of buoyancy and gravity, respectively. $\overline{GM_T}$ and $\overline{GM_L}$ are the transverse and longitudinal metacentric height, respectively. For a moored structure additional restoring force have to be added, but the effect of a spread mooring system on the linear wave induced motion is generally quite small [22].

2.4 Hydro-aero-servo-elastic coupling

A hydrodynamic load on a structure with an elastic body will cause a structural response in terms of an elastic deformation. The hydrodynamic load will, however, depend on the structural response, and this means that there will be a dependency between them both ways. This interaction is called hydro-elasticity. This effect can be difficult to capture properly and therefore it is strongly desirable to have a model which can. Two hydrodynamic models which could capture the elasticity effect were supposed to be made in this study. One of them was the flexible beam model with Morison-type loading only and this was made RIFLEX beam elements. The second one was the flexible beam model using distributed loads from first order potential theory.

Similar effect, in terms of external load and elasticity, can be seen for aerodynamic loading on a structural model. The aerodynamic loads will cause elastic deflection of structural components such as the blades and the tower. On the other hand, the deflection of the blades and the tower will change the effective wind velocity at the blades which again leads to change in the aerodynamic loads. This interaction is called aero-elasticity and describes the relationship between the aerodynamic loads and the structural response.

Most global dynamic analysis of FWTs have modelled the platform hull as rigid, and the tower, blades, and mooring lines with nonlinear beam elements. This type of model is commonly called a aero-hydro-elastic model. If the controller logic is also implemented in the model, the name changes to aero-hydro-servo-elastic model. This type of model couples the interaction between the loads from hydro- and aerodynamics with the structural response and the controller. Few global dynamic analysis of FWTs have modelled the platform hull as flexible and this leads to the lack of a proper name for this type of model. In this thesis will the hydrodynamic models where the hull is modelled elastic be referred to as hydro-elastic models.

The coupled global dynamic analyses of the different hydrodynamic models in this study were performed in SIMA. SIMA is a workbench which offers a complete solution for simulation and analysis of marine operations and floating systems developed by SINTEF [35]. An example of the advantage of using SIMA is that a RIFLEX model could be developed to capture the structural dynamics, while a SIMO-body could capture the hydrodynamic loads. This could be connected in SIMA together with a model capturing the aerodynamic loads and a wind turbine controller, and thereby result in a aero-hydro-servo-elastic coupled time-domain global dynamic analysis model. More detailed explanation regarding the hydrodynamic models are presented in chapter 4.

2.5 Decay tests

Decay tests will give important information regarding natural periods, added mass and damping of a dynamic system. They are performed in software by simulations, experimentally on models, and on full size floating structures. Decay tests are often used to verify natural periods, damping and general dynamic performance [29]. A brief introduction to theory behind decay tests in terms of natural frequency and damping will be presented here.

The starting point is the dynamic equilibrium equation for a 1-DOF free oscillating system with nonlinear damping given by:

$$M\ddot{\eta} + B_1\dot{\eta} + B_2\dot{\eta}|\dot{\eta}| + C\eta = 0. \tag{2.48}$$

Here M is the mass including the added mas, B_1 is the linear damping coefficient, B_2 is the quadratic damping coefficient and C is the restoring stiffness of the system. $\ddot{\eta}$, $\dot{\eta}$ and η are the acceleration, velocity and motion of the system, respectively. Dividing eq.(2.48) by the mass M gives the equation:

$$\ddot{\eta} + b_1\dot{\eta} + b_2\dot{\eta}|\dot{\eta}| + \omega_0^2\eta = 0. \tag{2.49}$$

Here $\omega_0 = \sqrt{\frac{C}{M}}$ is the natural frequency of the undamped system and b_1 and b_2 are the mass specific damping coefficients. One way to solve the equation is by energy considerations which are needed in order to represent the damping of the system correctly by the use of damping coefficients [36]. The mass specific energy of the system can be written as a function of time, V(t), and consist of the mass specific kinetic and potential energy:

$$V(t) = \frac{1}{2}\dot{\eta}^2 + \frac{1}{2}\omega_o^2\eta^2, \tag{2.50}$$

The term for the mass specific potential energy is found by comparing it to the potential energy from a spring $V_{pot} = \frac{1}{2}\frac{k}{m}x^2$ with $\omega_o = \sqrt{\frac{k}{m}}$.

The dissipated energy of the system is found by taking the average energy loss over a natural period. This is done by integrating the product of the damping terms and the velocity. Eq.(2.5) can now be written as the change of energy in the system $\dot{V}$:

$$\dot{V} = \dot{\eta}\ddot{\eta} + \omega_o^2\eta\dot{\eta} = -\dot{\eta}(b_1\dot{\eta} + b_2\dot{\eta}|\dot{\eta}|). \tag{2.51}$$

The integration is done from one peak of the response curve to next one and divided by the period of oscillations. In a decay test this will be the natural damping period, close to the natural undamped period if the damping is small. The dissipated energy from the system over a cycle is then represented by the energy loss function $L(V)$:

$$L(V) = \frac{1}{T_0}\int_0^{T_0} \dot{V}\,dt = \frac{\omega_o}{2\pi}\int_0^{\frac{2\pi}{\omega_o}} \dot{V}\,dt \tag{2.52}$$

Solving this integral gives the solution as:

$$L(V) = b_1 V + b_2\frac{8}{3}\pi 2\sqrt{2}V^{\frac{3}{2}}. \tag{2.53}$$

A cubic fit of the natural logarithm of the mass specific energy in the system $V(t)$ is made to estimate b_1 and b_2.

$$P = ln(V) = a_3 t^3 + a_2 t^2 + a_1 t + a_0. \tag{2.54}$$

The reason for a cubic fit is that it is easy to differentiate. The change of energy can then be found and compared to the energy loss function L(V) to determined b_1 and b_2. An example of the cubic fitting is shown for heave in Figure 2.13. The blue dots are the peaks or trough of the energy in the system. The kinetic energy is zero in a peak or trough due to zero velocity and therefore the energy is only given by the potential energy.

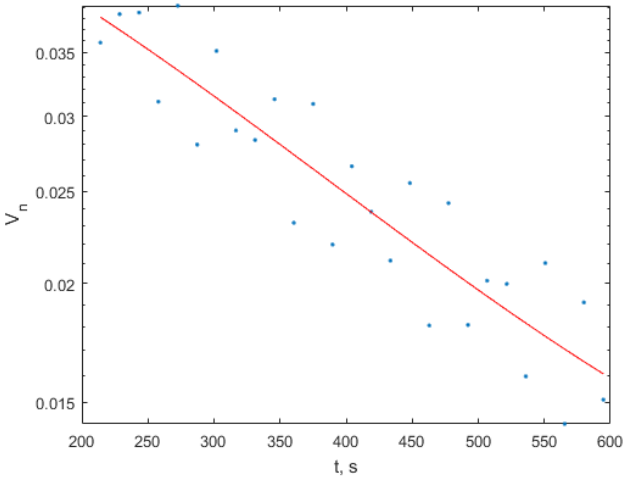

Figure 2.13: Example of a cubic fit of the mass specific energy of a system in pitch.

3 Platform design: OO-Star wind floater semi 10MW

The OO-Star Wind Floater Semi 10 MW is a semi-submersible concept with star-shaped base pontoon, which connects three outer columns to a central column. The floating structure is built out of post-tensioned concrete. The mooring system is a catenary mooring system with tree mooring lines, each connect to one of the outer columns. The structural properties of the floating platform will be described in the following section. The mooring system will also be introduced. These sections are based on the information given in the LIFES50+ result report *Deliverable D4.2:. Public definition of the two LIFES50+ 10 MW floater concepts (Summary)* [**oostar**]. The properties of the DTU 10 MW reference wind turbine will only be presented briefly due to simplifications done in the hydrodynamic models. Explanation of these simplifications will be discussed later.

Figure 3.1: OO-Star Wind Floater Semi 10MW.

3.1 DTU 10MW reference wind turbine data

Table 3.1 contains the overall mass properties together with the inertia values for the combined tower top masses. This includes the rotor and the nacelle. The inertia values are calculated assuming a locked rotor. More characteristics of the DTU 10MW reference wind turbine data can be found in reference [37].

Table 3.1: Properties of the DTU 10MW reference wind turbine.

Property	Unit	Value
Rotor mass	[kg]	230717
Rotor COG	[m, m, m]	[-7.07, 0, 119]
Nacelle mass	[kg]	446006
Nacelle COG	[m, m, m]	[2.69, 0, 118.08]
Nacelle, rotor and hub vertical COG	[m]	118.39
Combined tower top masses	[kg]	676 723
Combined tower top masses COG	[m, m, m]	[-0.939, 0, 2.789]
Roll moment of inertia of tower top masses around tower top	[kg m^2]	$1.659 \cdot 10^8$
Pitch moment of inertia of tower top masses around tower top	[kg m^2]	$1.062 \cdot 10^8$
Yaw moment of inertia of tower top masses around tower top	[kg m^2]	$1.014 \cdot 10^8$

3.2 Tower properties

The tower of the OO-Star Wind Floater Semi 10MW have been modified compared to the land based tower developed for standard DTU 10MW on land. It is defined in segments, each having a constant wall thickness. Hence, the tower thickness cannot be interpolated across the tower and the properties for each segment needs to be considered. The properties for each segment can be seen in Table 3.2 However, the diameter can be linearly interpolated for each segment. The tower top connects directly to the rotor nacelle assembly (RNA). A sketch of the tower setup is shown in Figure 3.2.

Table 3.2: OO-Star Wind Floater Semi 10MW distributed tower properties (elevation given w.r.t 11 m above MSL).

Section	Lower elevation	Upper elevation	Outer diameter	Wall thickness	Cross sectional area	Section mass
-	[m]	[m]	[m]	[m]	[m^2]	[kg]
1	0	3.946	11.385	0.075	2.665	$8.667 \cdot 10^4$
2	3.946	7.892	11.154	0.074	2.576	$8.378 \cdot 10^4$
3	7.892	11.838	10.923	0.072	2.454	$7.983 \cdot 10^4$
4	11.838	15.785	10.692	0.07	2.336	$7.598 \cdot 10^4$
5	15.785	19.731	10.462	0.068	2.220	$7.222 \cdot 10^4$
6	19.731	23.677	10.231	0.066	2.108	$6.855 \cdot 10^4$
7	23.677	27.623	10.000	0.065	2.029	$6.599 \cdot 10^4$
8	27.623	31.569	9.769	0.063	1.921	$6.248 \cdot 10^4$
9	31.569	35.515	9.538	0.061	1.816	$5.908 \cdot 10^4$
10	35.515	39.462	9.308	0.059	1.714	$5.576 \cdot 10^4$
11	39.462	43.408	9.077	0.057	1.615	$5.254 \cdot 10^4$
12	43.408	47.354	8.846	0.056	1.546	$5.030 \cdot 10^4$
13	47.354	51.300	8.615	0.054	1.452	$4.724 \cdot 10^4$
14	51.300	55.246	8.385	0.052	1.361	$4.428 \cdot 10^4$
15	55.246	59.192	8.154	0.050	1.273	$4.140 \cdot 10^4$
16	59.192	63.138	7.923	0.048	1.188	$3.863 \cdot 10^4$
17	63.138	67.085	7.692	0.047	1.129	$3.672 \cdot 10^4$
18	67.085	71.031	7.462	0.045	1.048	$3.410 \cdot 10^4$
19	71.031	74.977	7.231	0.043	0.971	$3.158 \cdot 10^4$
20	74.977	78.923	7.000	0.041	0.896	$2.916 \cdot 10^4$
21	78.923	82.869	6.769	0.039	0.825	$2.682 \cdot 10^4$
22	82.869	86.815	6.538	0.038	0.776	$2.524 \cdot 10^4$
23	86.815	90.762	6.308	0.036	0.709	$2.307 \cdot 10^4$
24	90.762	94.708	6.077	0.034	0.645	$2.099 \cdot 10^4$
25	94.708	98.654	5.846	0.032	0.585	$1.901 \cdot 10^4$
26	98.654	102.600	5.615	0.030	0.526	$1.712 \cdot 10^4$
27	102.600	104.630	5.441	0.029	0.484	$0.810 \cdot 10^4$

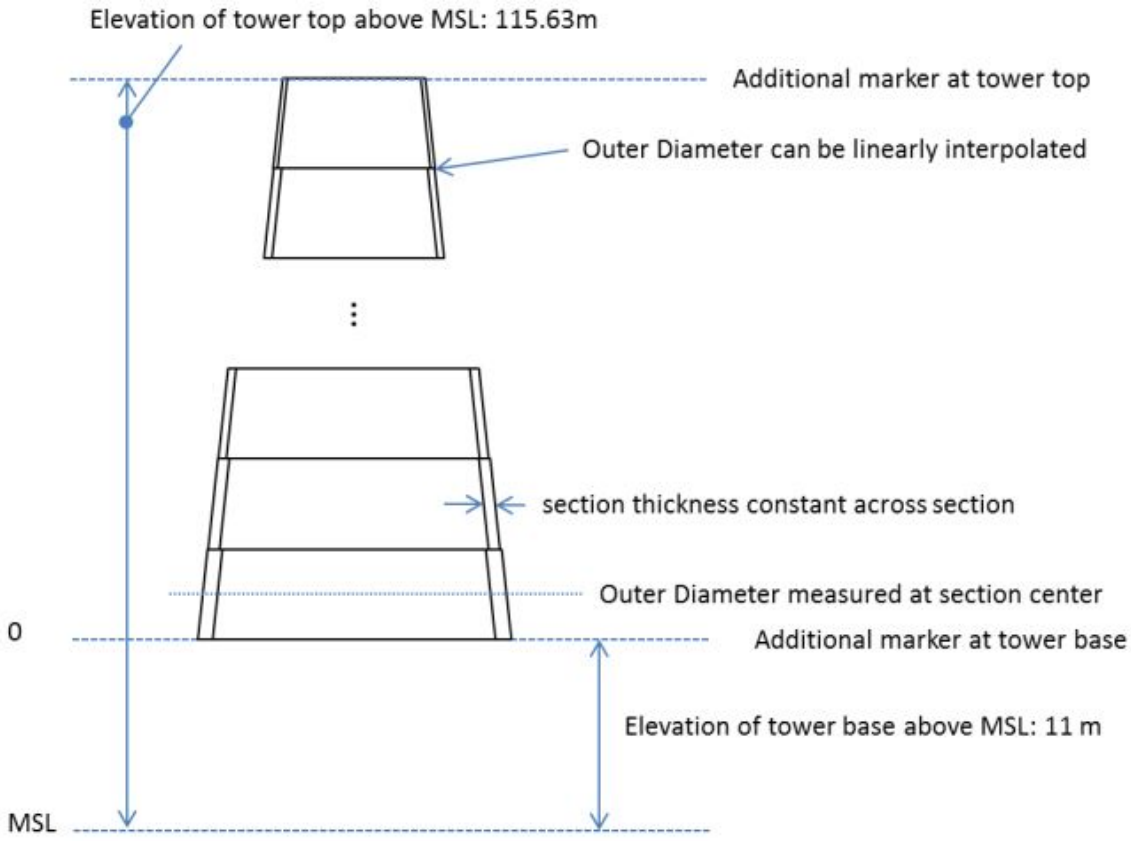

Figure 3.2: Sketch of OO-Star Wind Floater Semi 10MW tower definition.

3.3 Platform structural properties

The floating platform consist of a lower star-shaped pontoon connecting three outer columns to a central column. The outer columns have different dimensions than the central column, both in diameter and height. The columns have cylindrical upper part and tapered lower part, like a cone. The main material used for the platform are post-tensioned concrete. This means that the tendons are tensioned after the surrounding concrete structure has been cast. By making the platform in concrete yields a higher displaced volume compared with steel as the main material.

The geometrical properties of the platform are shown in Figure 3.3. The distance between the center of the outer columns and the center of the center column are 37 m. The horizontal pontoon elements connecting the outer columns and the center column have a height of 7 m. It's important to notice that the pontoon elements are slightly tapered from a width of 16 m at the center column to a width of 15.8 m at the outer columns. The slabs attached at the bottom part of the pontoon elements have a width of 17 m, adding 0.5 m extra on each side. The slabs from the pontoon elements are connected underneath the center column with a curvature radius of 10 m. The top part of the center column have a constant

diameter of 12.05 m for a height of 8.225 m. The lower part of the center column have a linearly varying diameter from 12.05 m to 16.2 m for a height of 17.775 m. The top part of the outer columns have a constant diameter of 13.4 m for a height of 13.5 m. The lower part of the outer columns have a linear varying diameter from 13.4 m to 15.8 m for a height of 11 m. The circular part of the slabs on the outer columns have a diameter of 22.8 m.

The platform has an overall mass of 21709 tonnes including ballast. The displaced water volume is 23509 m^3. The mass moments of inertia have been calculated about the centre of mass with a value of 9.43E+09 kgm^2 about x- and y-axis and 1.63E+10 kgm^2 about z. All of the important structural properties are listed in Table 3.3.

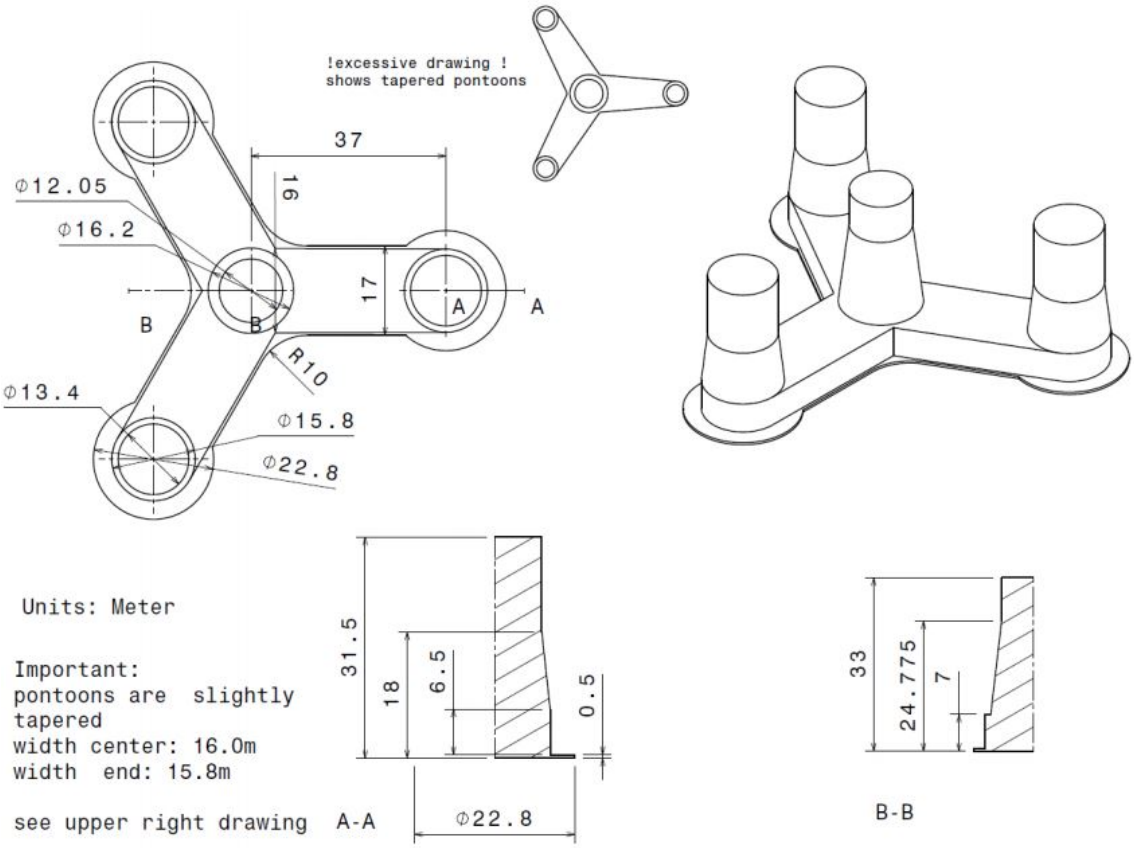

Figure 3.3: OO-Star Wind Floater Semi 10MW main dimensions, drawings.

Table 3.3: OO-Star Wind Floater Semi 10MW platform parameters including ballast.

Property	Unit	Value
Overall substructure mass	[kg]	$2.1709 \cdot 10^7$
Substructure vertical COG below MSL	[m]	15.225
Substructure roll inertia about COG	[kg m^2]	$9.43 \cdot 10^9$
Substructure pitch inertia about COG	[kg m^2]	$9.43 \cdot 10^9$
Substructure yaw inertia about COG	[kg m^2]	$1.63 \cdot 10^{10}$
Tower base interface above MSL	[m]	11
Draft at equilibrium position with moorings (no thrust)	[m]	22
Displaced water volume	[m^3]	$2.3509 \cdot 10^4$
Centre of buoyancy below MSL	[m]	14.236

3.4 Mooring system properties

The layout of the mooring system is given in Figure 3.4, with the top view on the left side and the side view on the right side. It is a catenary mooring system with three lines with a horizontal angle of 120 degrees between them. The fairleads are at the top of each of the outer columns, which is 9.5 m above the mean water level. Each of the lines have a clump mass attached to it. The upper segment, from the fairlead to the clump mass, have a length of 118 m. The lower segment, from the clump mass to the anchor, have a length of 585 m, which gives the total length of a line to be 703 m. The chain parameters are equal for the upper and lower segment of a line. Important parameters of the mooring system are listed in Table 3.4.

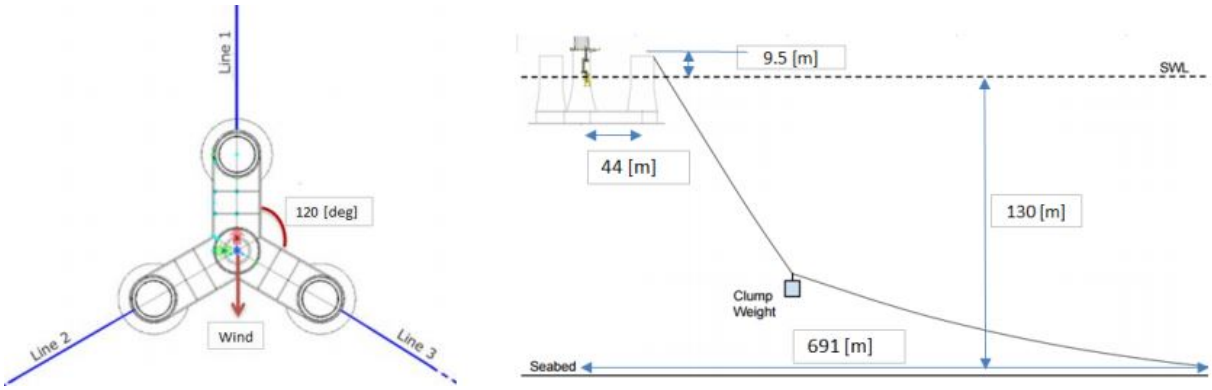

Figure 3.4: OO-Star Wind Floater Semi 10MW mooring line arrangement in the top view (left) and side view (right).

Table 3.4: OO-Star Wind Floater Semi 10MW mooring system properties.

Property	Unit	Value
Number of lines	-	3
Angle between adjacent lines	deg	120
Equivalent total mass in water of the clump mass	kg	50000
Unstretched mooring line length, upper part	m	118
Unstretched mooring line length, lower part	m	585
Vertical position of fairleads above MSL	m	9.5
Radius to anchors from platform centreline	m	691
Anchor position below MSL	m	130
Radius to fairleads from platform centreline	m	44
Initial vertical position of clump mass below MSL	m	90.45
Initial radius to lump mass from centreline	m	148.6
Pretension	N	$1.670 \cdot 10^6$
Soil stiffness	Pa/m	$3.00 \cdot 10^6$
Soil damping	PaS/m	$3.00 \cdot 10^5$
Equivalent mass per length in air	kg/m	375.38
Equivalent weight per length in water	N/m	3200.6
Extensional stiffness EA	N	$1.506 \cdot 10^9$
Hydrodynamic added mass coefficient	-	0.8
Hydrodynamic drag coefficient	-	2
Effective hydraulic diameter of the chain	m	0.246
Physical chain diameter	m	0.137

4 Hydrodynamic models and results

As mentioned before, the main objectives with this study were to evaluate the expected internal forces in the structure and the structural dynamics of a large-volume floating wind turbine (FTW) with different wave theories to check possible modelling strategies. Also, the development of a framework for a fully coupled model, including floater dynamics and possibly hydro-elasticity, was an objective. The semi-submersible wind turbine (SSWT) concept OO-Star Wind Floater Semi 10MW were chosen as the concept to be examined, see chapter 3 for more information. Four different hydrodynamic models were supposed to be made and evaluated in this study. These were:

1. Rigid body model using first order potential theory. Referred to as rigid body potential (RBP) model.
2. Rigid body model using Morison's equation. Referred to as rigid body Morison (RBM) model.
3. Flexible beam model using Morison's equation. Referred to as flexible body Morison (FBM) model.
4. Flexible beam model using distributed loads from first order potential theory. Referred to as flexible body potential (FBP) model.

All of the hydrodynamic models were made except the FBP model due to software problems. A lot of time and effort were used on the FBP model to try to finish the model without success. This made it difficult to reach some of the objectives in this study. The main focus of this report was therefore to investigate wave loading on the SSWT and to what extent, and when, wave loads can be represented with the different modelling strategies. The modelling procedure of the different hydrodynamic models were different from each other, but had some parts that were the same. Information regarding parts that were the same will be presented in the following paragraphs.

Viscous effects

Viscous effects in terms of quadratic drag were included in all of the four models to properly describe the hydrodynamics loads. Potential flow theory cannot capture viscous effects since one of the assumptions behind it is inviscid flow. The quadratic drag was calculated by Morison's equation for each of the structural parts representing the substructure of the FWT and set to be equal in all of the four models. The structural parts representing the substructure were simplified to cylinders due to limitations in RIFLEX. The cone parts of the columns were simplified to cylinders with constant diameter. The diameter was chosen to be the mean value between the diameter at the top and the diameter at the bottom of the cone part. The pontoons were simplified to cylinders, but different reference areas were used for the quadratic drag depending on direction. Slender elements were used in the RBP model and the RBM model to contain the quadratic drag, while flexible beam elements were used in the FBM model and the FBP model. Table 4.1 shows the drag coefficients together with diameters taken from the D4.5 report [38]. The drag coefficients were based on the Reynolds number (Re) and Keulegan-Carpenter number

(KC). The drag coefficients for the cone parts of the columns were estimated to be the mean value between the drag coefficients for the top parts and the the drag coefficients for the bottom parts.
D4.5 report [38]

Table 4.1: OO-Star Wind Floater Semi 10MW drag coefficients.

Structural part	**Diameter[m]**	**Drag coefficient C_D[-]**
Outer column top part	13.400	0.7200
Outer column cone part	14.600	0.7130
Outer column bot part	15.800	0.7060
Outer column shirt part	22.800	10.0000
Central column top part	12.050	0.7290
Central column cone part	14.125	0.7165
Central column bot part	16.200	0.7040
Pontoons vertical	7.000	2.0500
Pontoons horizontal	17.000	2.0500

Wind turbine simplifications

Multiple simplifications were done to the DTU 10 MW reference wind turbine in all the models. The blades of the wind turbine, which usually are modelled with RIFLEX beam elements, were removed. The SIMO-bodies representing the nacelle, rotor and hub were replaced with a single SIMO-body with the tower top properties listed in Table 3.1. The tower sections were simplified from cone sections with different diameters for top and bottom to a constant diameter for each section. The main reasons for this simplification was:

- Narrow done the objectives in this thesis. The main focus in this study was on the hydrodynamics of FWT. This could still be analysed with the simplifications done to the reference wind turbine. The simplifications removed the focus on the aerodynamics and allowed more focus on the hydrodynamics.
- Faster simulations. The time step in SIMA needs to be low when DTU 10MW reference wind turbine is part of the model. The reason for this is to be able to capture high velocity of the blade tips. The simplifications allowed the time step in the simulations to be increased from 0.005 s to 0.01 which reduced the simulation time substantially.
- Reduce the work load. The aerodynamics was not a field of expertise for the author of this thesis and would require time to learn and understand.
- Leave to future work. The models were made such that the DTU 10MW reference wind turbine could be inserted back again relatively easy. To insert the wind turbine back again will be an obvious recommendation for future work.

The following sections will present detailed explanations of the modelling procedures of the hydrody-

namic models. Discussion of results, discrepancies, and possible explanations from analyses performed on the models are also presented. The software problems and how far the FBP model was developed will be shown as well.

4.1 Rigid model using first order potential theory

Four different hydrodynamic models were to be developed in this thesis. The first model to be made was the rigid body model using fist order potential theory, referred to as rigid body potential (RBP) model. The RBP model was generated as a SIMO-RIFLEX model. A SIMO-body was used to model the hydrodynamic loads using potential flow theory on the hull and RIFLEX elements were used to model the tower and the mooring system. The hull was modelled as rigid. The SIMO-body contained the hydrostatic stiffness, frequency-dependent added mass and damping, force and motion transfer functions, and retardation functions for the hull. A number of different engineering software were used in order to do this. GeniE was used to create a 3D geometry model of the hull of the floating substructure. This model was taken into HydroD in order to generate a 3D panel model of the hull. Added mass and radiation damping coefficients together with first-order wave excitation for the different motions were then calculated for the hull using Wadam in HydroD. A MATLAB script was developed to calculate the hydrostatic stiffness of the hull. A SIMO-RIFLEX model of the total structure (tower, floating substructure and mooring system) was then created in SIMA. Slender elements were created to account for viscous effects in terms of quadratic drag as mentioned before. Finally, the calculated data from HydroD and MATLAB were implemented in the SIMO-body representing the hull. Figure 4.1 shows the RBP model in SIMA. Figure 4.2 shows a schematic of the modelling procedure. Decay tests and a regular waves test were performed on the RBP model to analyse the motion response of the model. The results from the decay tests were also compared against the results from the results in the D4.2 report [15]. Hand calculations of the natural period and cancellation period in heave for the OO-Star Wind Floater Semi 10MW were done for comparison. The following sections will give more details on how each of the steps in the modeling procedure were done to create the rigid hull model and the reasoning behind it. The results from the tests with discussion will also be presented.

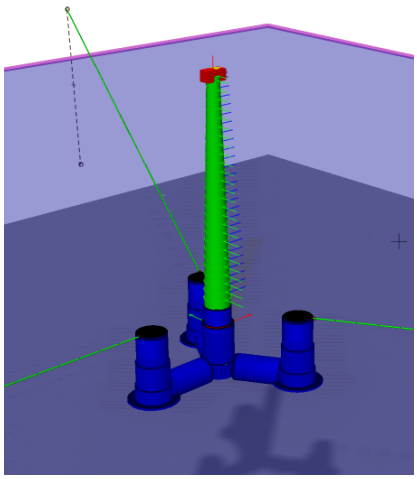

Figure 4.1: The rigid body with fist order potential theory (RBP model) in SIMA.

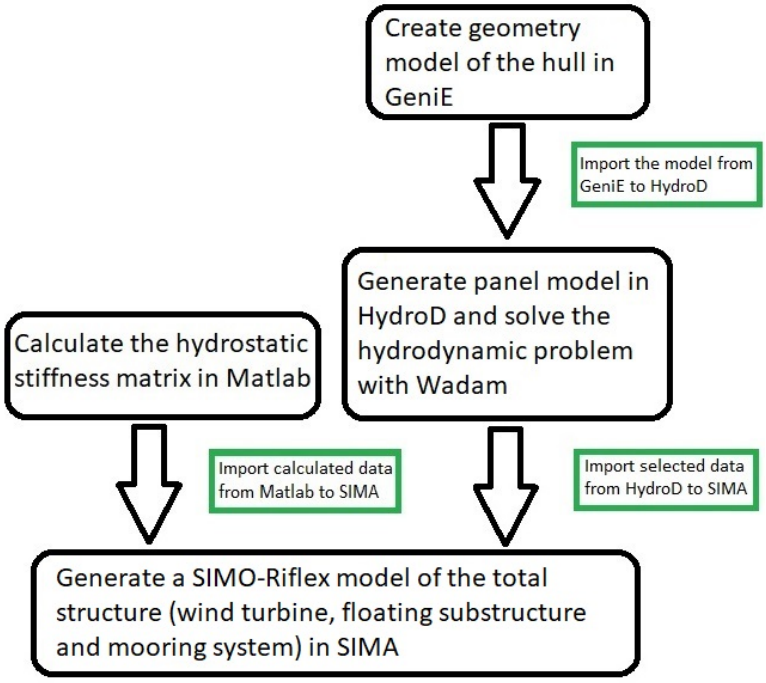

Figure 4.2: Schematic of the modelling procedure.

4.1.1 Geometry model of the hull

The starting point of creating the RBP model was the D4.2 report [15]. The geometrical description of the floater for the OO-Star Wind Floater Semi 10MW was used to generate a 3D geometry model in GeniE. GeniE is a structural design analysis computer program part of the Sesam package [39]. The software is fully owned, maintained and supported by DNV GL - Software. The modeling was done by programming a JavaScript which GeniE could read directly and create the model. A simplification was done for the connection of the pontoon elements underneath the center column. A straight line was used instead of a curvature. The final step in GeniE was to generate a mesh of the geometry model. Only half of the hull was modelled and meshed due to symmetry about the x-z plane.

The meshing part turned out to be a bit of struggle in terms of creating a good mesh. There were variations in element size, small elements close to large elements and strange mesh patterns. This problem was solved by defining the number of elements along a lot of the edges. A small convergence study for different mesh refinements was performed to check the dependence of the mesh. Figure 4.3 shows the geometry model in GeniE with three different mesh sizes. The default mesh size of an element was tested to be 1.0 m, 0.7 m and 0.6 m. The specified number of elements along an edge was also changed with respect to the default mesh size. The reason for not having a smaller mesh size was that the panel model in HydroD would not run with it. The different mesh sizes will be referred to as low, medium and high mesh, see Figure 4.3. The results from the mesh convergence study together with the results from

the D4.2 can be seen in Figure 4.6, 4.8 and 4.10. The figures will be more discussed in later sections, but the results showed that the medium mesh size was accurate enough and was therefore used for further work. The largest mesh length of an element for this mesh was approximately 1.75m due to the specified number of elements along edges. The total number of surface elements was in the end 2588.

A mistake in the geometry model in GeniE was later found. The mistake was that the shirt along the pontoons was not tapered as the pontoons. This means that the width of the bottom part of the pontoons was 17 m instead of going from 17 m to 16.8 m along the pontoons. The mistake was found late in the study and therefore not fixed for any of the hydrodynamic models. The impact on the results was assumed to be negligible.

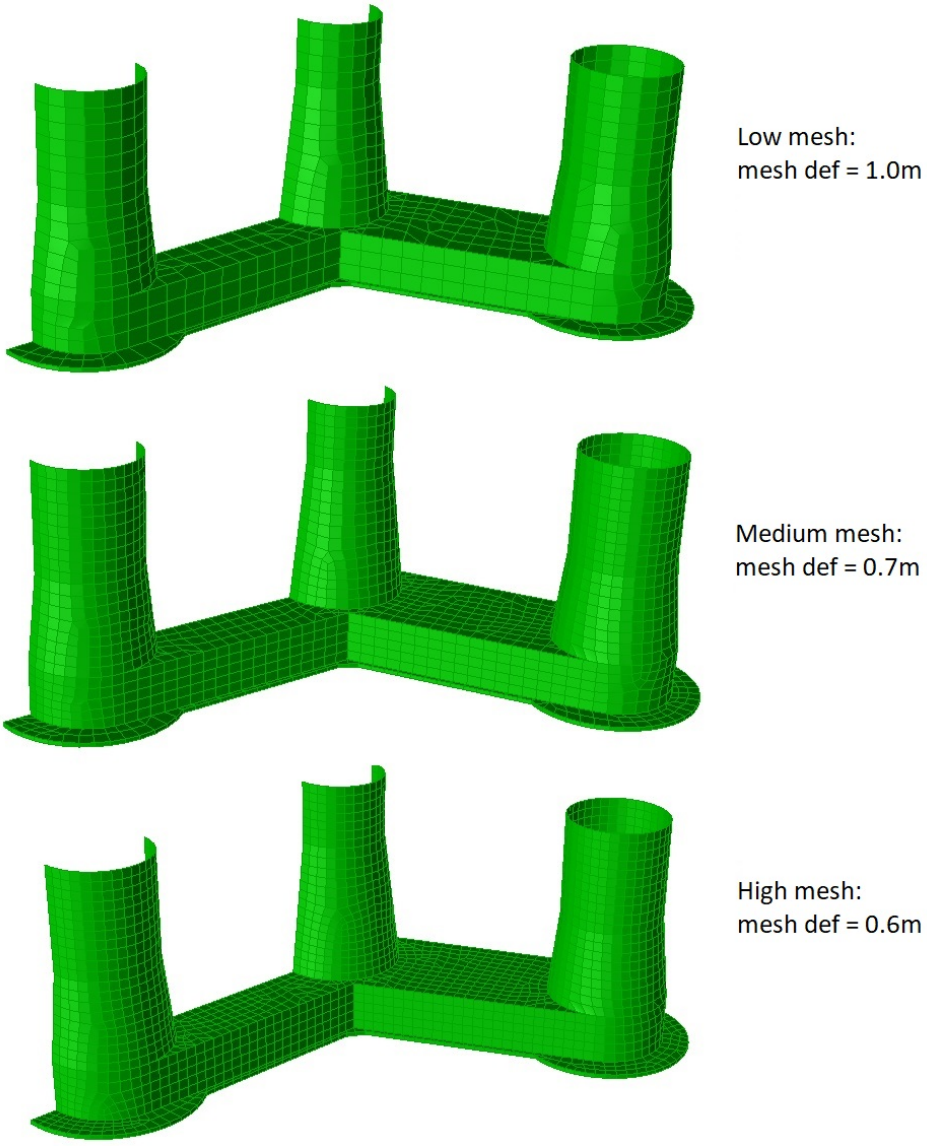

Figure 4.3: Comparison of different mesh sizes in GeniE for the OO-Star Wind Floater Semi 10MW. Low, medium and high mesh are different mesh sizes.

4.1.2 Panel model of the hull

The 3D geometry model of the hull of the OO-Star Wind Floater Semi 10MW was imported from GeniE into HydroD to generate a 3D panel model of the hull. This procedure was done for the three different mesh sizes, but will be explained for the medium mesh size. HydroD is a computer program for computation of hydrostatics and stability for ships and offshore structures [32]. It's also part of the SESAM package and fully owned, maintained and supported by DNV GL - Software as GeniE. Importing a meshed geometry model into HydroD gives a panel model with the same number of panels as elements in the geometry model. Hence, the total number of panels was also 2588. A recommendation is given in *Sea loads on ships and offshore structures* by Faltinsen [22] that in general about 1000 panels should be sufficient. This recommendation is given for comparable structures to the OO-Star Wind Floater Semi 10MW. Thus, 2588 panels was assumed to be enough. Another recommendation was found in DNV-RP-C205, which is a recommended practice for environmental conditions and loads made by DNV GL, that for a low-order panel method, which was the case here, the diagonal length of panel mesh should be less than 1/6 of smallest wave length analyzed [40]. The largest diagonal lengths of the panel mesh in the model was approximately 2.47m. This means that the smallest wave length should be larger than approximately 14.8m for the given panel mesh. The wave period, T, can be calculated for a given wave length, λ, by the dispersion relation and assuming deep water conditions, eq. (4.1). From this equation it was found that the wave period should be larger than approximately 3.1 s based on the recommendation. This should be kept in mind regarding the accuracy of the results obtained from analyses with wave periods smaller than 3.1 s.

$$\omega^2 = kg \qquad k = \frac{2\pi}{\lambda} \quad \Rightarrow T = \sqrt{\frac{2\pi\lambda}{g}} \tag{4.1}$$

The next step in HydroD was to define an environment in terms of air and water density, viscosity, water depth, wave frequencies and gravity acceleration. The environment needed to be defined in order to solve the potential problem for the panel model. 60 different wave frequencies were chosen, ranging from 0.01 rad/s all the way up to 3.20 rad/s. The frequency interval varied between the wave frequencies in order to have more frequencies in the important parts of the frequency spectrum. The environmental variables are listed in Table 4.2.

Table 4.2: Environment in HydroD.

Variable	Unit	Value
Wave frequencies	rad/s	0.01-4.00
Water depth	m	130
Water density	kg/m^3	1025
Water viscosity	m^2/s	$1.19 \cdot 10^{-6}$
Air density	kg/m^3	1.226
Air viscosity	m^2/s	$1.462 \cdot 10^{-5}$
Gravity acceleration	m/s^2	9.80665

The panel model of the hull was generated with HydroD and is shown in Figure 4.4. The displaced water volume was checked in HydroD to verify that it was the same as the reported value in the D4.2 report [15]. This was found to be 23534 m^3 in the model compared to 23509 m^3 in the report. The difference was probably due to the simplifications of the geometry of the hull in GeniE. The difference in displaced water volume was assumed to be acceptable. The center of buoyancy was also checked to be (0,0,-14.238m) compared to (0,0,-14.236). HydroD offers two different hydrodynamic solvers, Wadam and Wasim, where the first one was used in this study. Wadam solves the radiation and diffraction problems in the frequency domain using the frequency response method, see chapter 2 for information. A MATLAB script, which was given by the supervisor, was further developed to read the results from Wadam and plot the frequency-dependent added-mass, radiation damping and first-order wave excitation for the hull.

Table 4.3: Comparison of results from D4.2 report [15] and HydroD.

Variable	Unit	D4.2 report	HydroD
Displaced water volume	m^3	23509	23534
Center of buoyancy below MSL	m	-14.236	-14.238

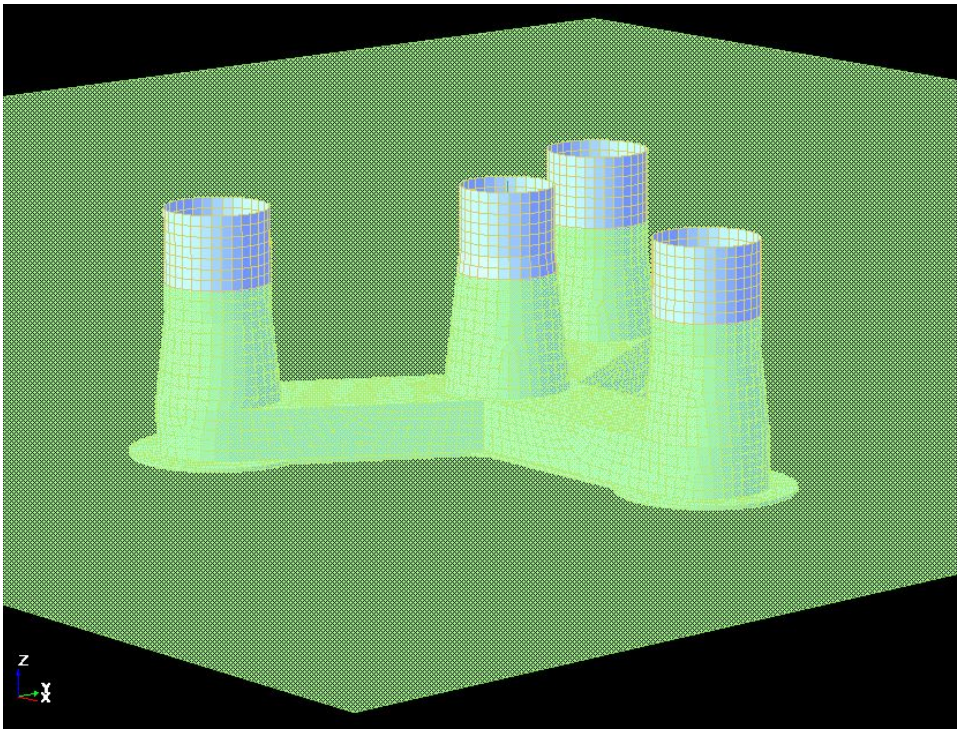

Figure 4.4: Panel model of the hull of the OO-Star Wind Floater Semi 10MW in HydroD.

4.1.2.1 Added mass for the hull

The results of the frequency-dependent added mass coefficients for the medium mesh size are shown in Figure 4.5. There is a total of 36 added mass coefficients A_{kj} where k,j = 1,..,6. If a structure has zero speed and the submerged part has a vertical symmetry plane, half of the coefficients are zero [22]. Also, $A_{kj} = A_{kj}$. This is the case for the the OO-Star Wind Floater Semi 10MW. It is therefore expected to see a lot of added mass coefficients that are zero and others that are identical to each other. First thing to notice in figure 4.5 is that the added mass in surge, A_{11}, and roll, A_{44}, are the same as the added mass in sway, A_{22}, and pitch, A_{55}, respectively. This seems correct due to symmetry of the hull. The added mass coefficients for all of the motions (surge (A_{11}), sway (A_{22}), heave (A_{33}), roll (A_{44}), pitch (A_{55}) and yaw (A_{66})) shows frequency variation up to 2 rad/s. The coupled added mass coefficients A_{24} and A_{42} are identical to each other as expected and show frequency variation up to 2 rad/s as well. Similarly, are A_{15} and A_{51}.

The results were compared with the added mass coefficients obtained by the other mesh sizes and the D4.2 report [15], see Figure 4.6. Low, medium and high are the different mesh sizes and OO is the result from the D4.2 report. The results from the D4.2 report were extracted from the report by using WebPlot-Digitizer, a web based tool to extract data from plots. This was done relatively accurate, but have some error margin connected to it. The comparison shows a good match to the D4.2 report in terms shape and values. The limitation in HydroD with only allowing 60 different wave frequencies for one Wadam

run made it difficult to capture all the peaks for the different coefficients. This may also be the case for the results in the D4.2 report with not enough frequencies tested around the peaks. The different mesh sizes shows some difference between them, but the difference is smaller between high and medium mesh size compared to medium and low mesh size. This was part of the reason that the medium mesh size was chosen as the mesh used for future work.

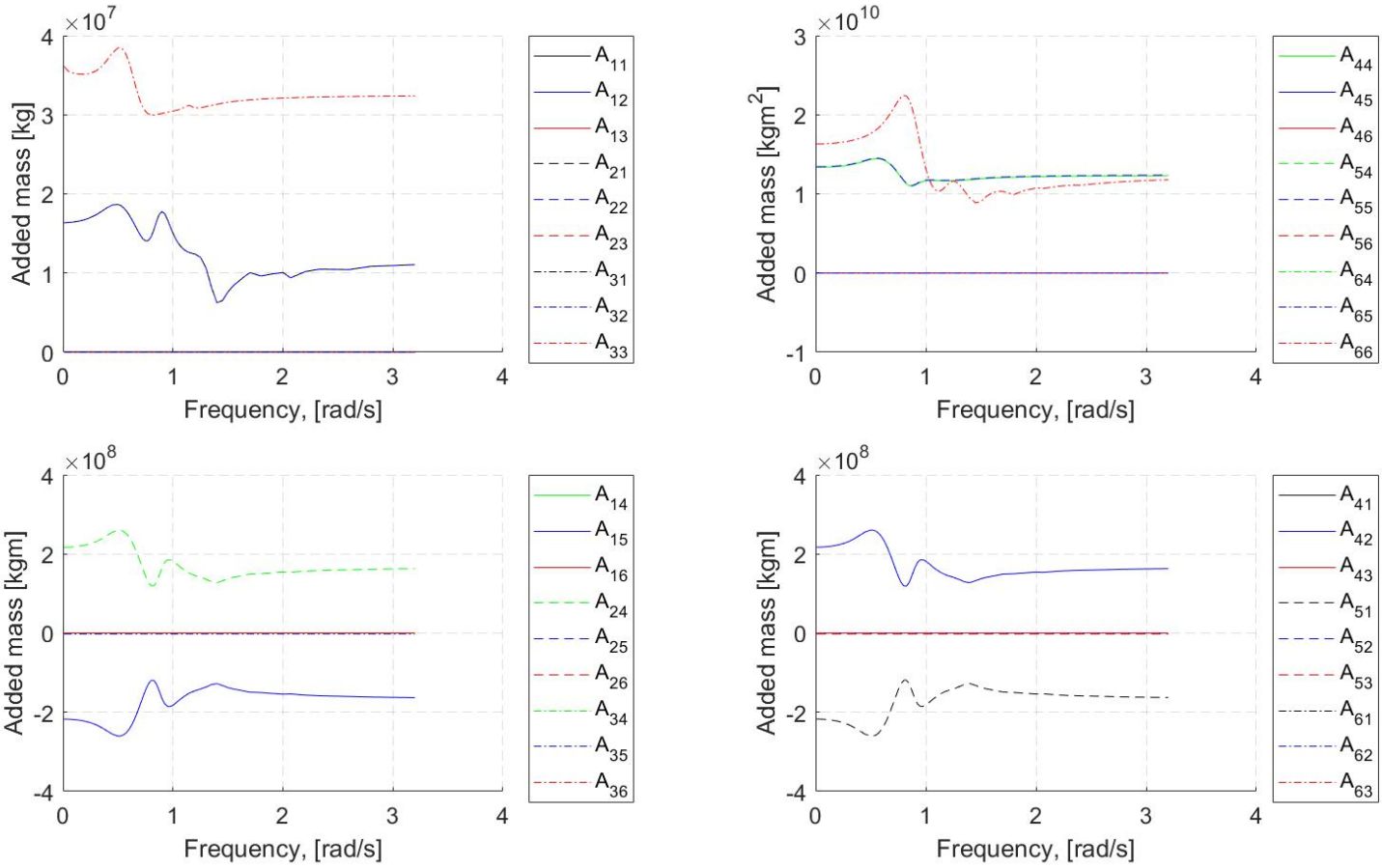

Figure 4.5: OO-Star Wind Floater Semi 10MW hydrodynamic added mass coefficients from Wadam in HydroD.

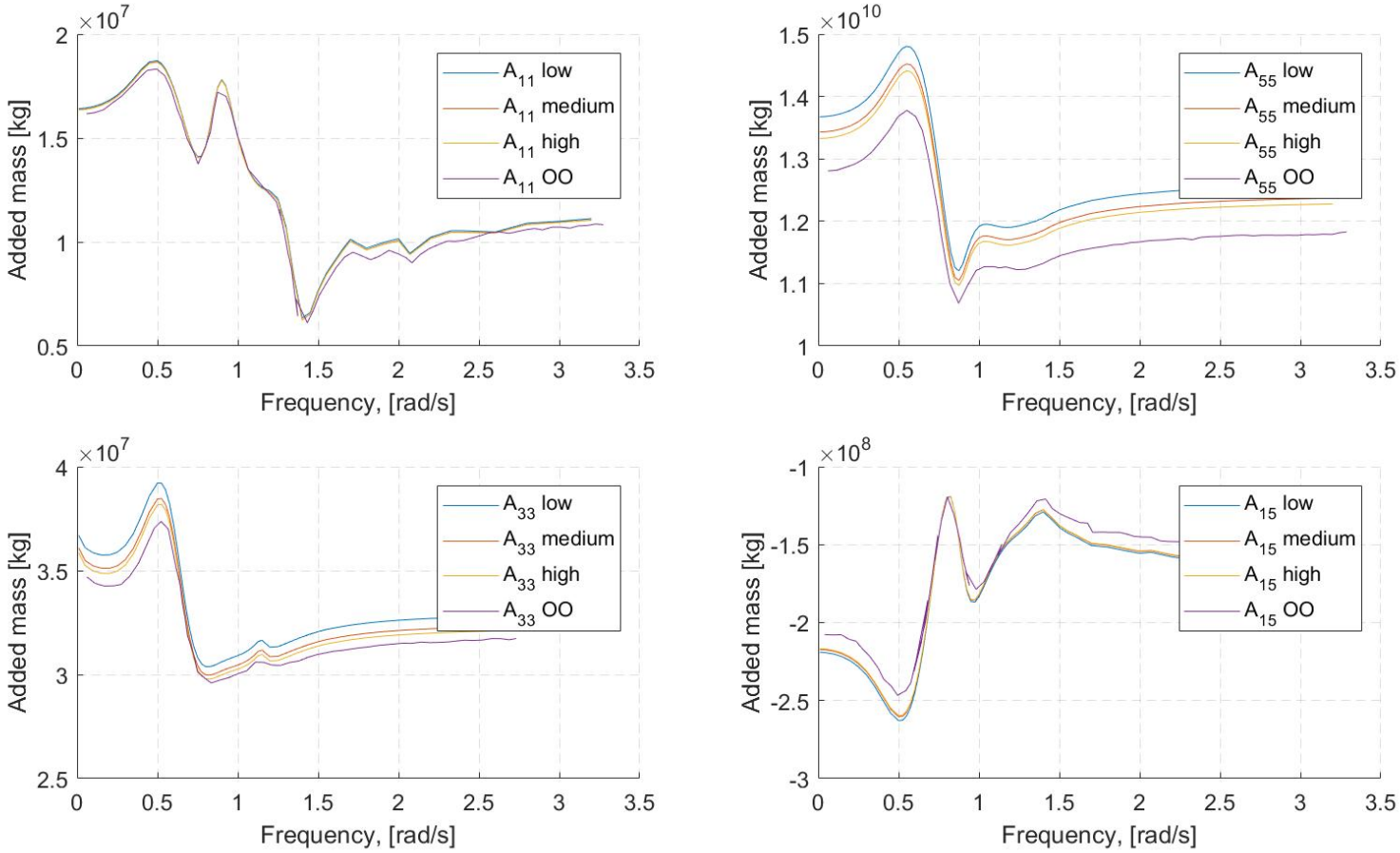

Figure 4.6: Comparison of OO-Star Wind Floater Semi 10MW hydrodynamic added mass coefficients from Wadam in HydroD and the D4.2 report [15]. The results are given for 0° wave heading direction. Low, medium and high are different mesh sizes and OO is the result from the D4.2 report.

4.1.2.2 Linear radiation damping for the hull

The results of the frequency-dependent radiation damping coefficients for the medium mesh size are shown in Figure 4.5. It is expected to see damping coefficients that are zero and others that are identical to each other for the same reasons as mentioned for the added mass coefficients. First thing to notice is that radiation damping in surge, B_{11}, and roll, B_{44}, are the same as added mass in sway, B_{22}, and pitch, B_{55}, respectively. This seems correct due to symmetry of the hull. The radiation damping coefficients for all of the motions (surge (B_{11}), sway (B_{22}), heave (B_{33}), roll (B_{44}), pitch (B_{55}) and yaw (B_{66})) show frequency variation. Especially the damping in surge, sway and yaw which show large frequency variation for large parts of the frequency interval 0-3.2 rad/s. All of the damping coefficients goes towards zero when the frequency goes towards zero or infinity. The coupled radiation damping coefficients B_{24} and B_{42} are identical to each other as expected and shows frequency variation between 0.3 rad/s to 2.2 rad/s. Similarly, are B_{15} and B_{51}.

The results were compared with the radiation damping coefficients obtained by the other mesh sizes and the D4.2 report [15], see Figure 4.8. Low, medium and high are the different mesh sizes and OO is the result from the D4.2 report. The extraction of data from the plots in the D4.2 report was done the same way as for the added mass coefficients in terms of using WebPlotDigitizer. The comparison shows a good match to the D4.2 report with respect to shape and values, same as the added mass coefficients. The differences in the results are largest around the peaks. This is assumed to be a combination of the limitation in HydroD with only allowing 60 different wave frequencies for one Wadam run and the accuracy of the results in the D4.2 report. With accuracy it is meant the number of wave frequencies around the peaks used in the report and the extraction of the results from the report. The different mesh sizes shows more or less the same results.

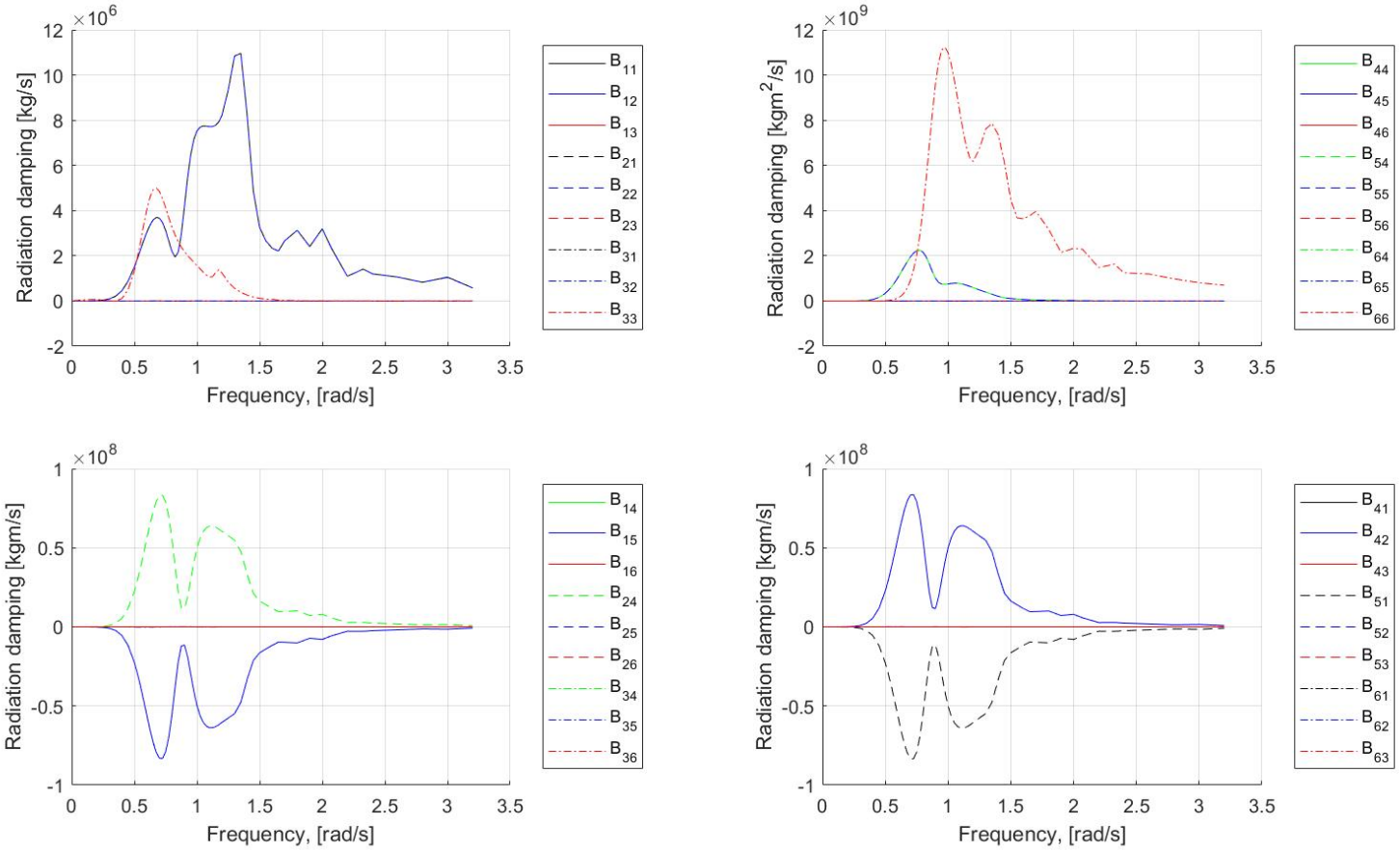

Figure 4.7: OO-Star Wind Floater Semi 10MW hydrodynamic radiation damping coefficients from HydroD-Wadam.

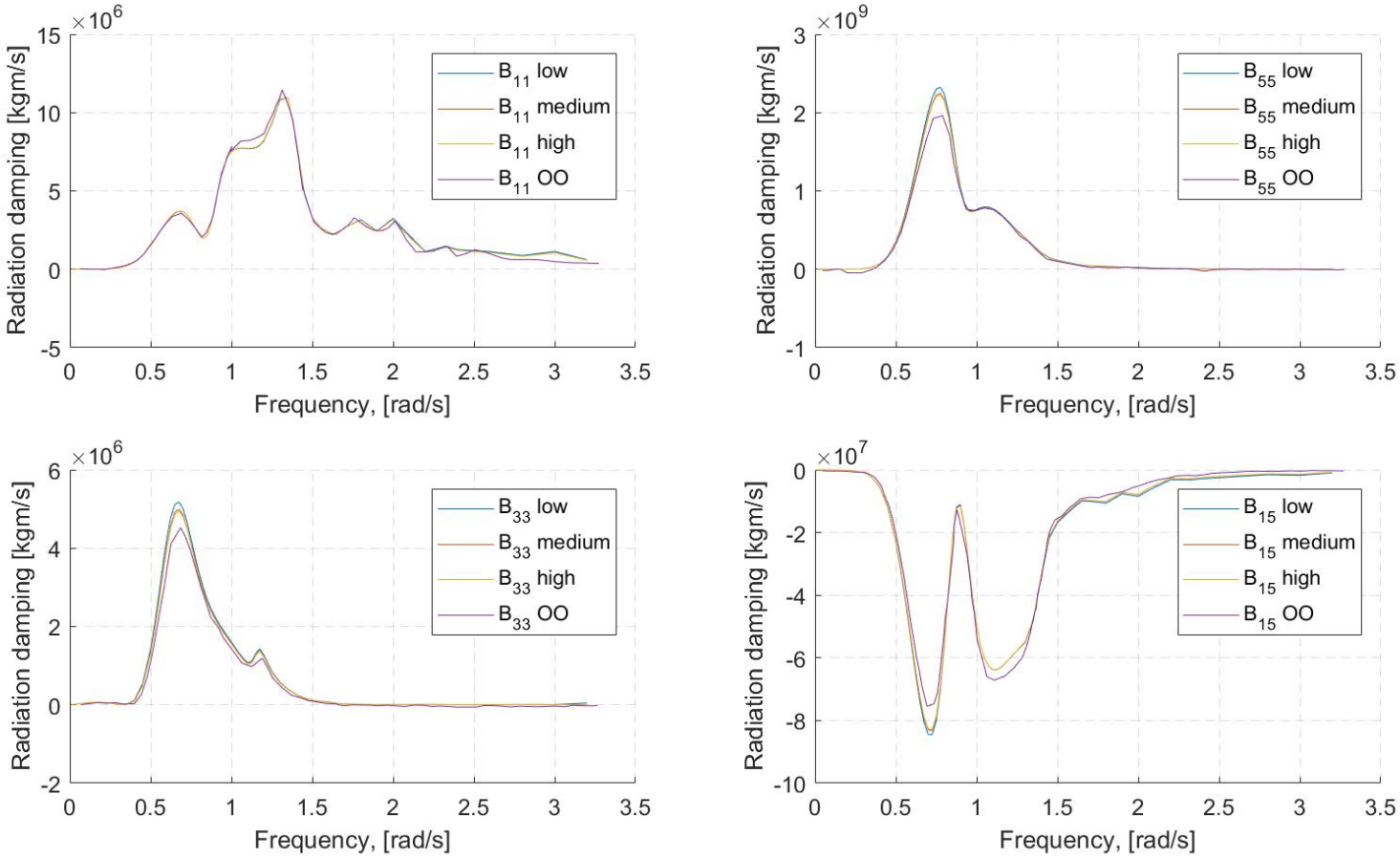

Figure 4.8: Comparison of the OO-Star Wind Floater Semi 10MW hydrodynamic radiation damping coefficients from HydroD-Wadam and the life50+ report [15](results are given for 0° wave heading direction). Low, medium and high are different mesh sizes and OO is from the life50+ report.

4.1.2.3 First-order wave excitation for the hull

The results of the frequency-dependent first-order wave excitation forces for the medium mesh size are shown in Figure 4.9. The plots to the left show the magnitude and the plots to the right show the phase of the wave excitation with the wave incident angle 0°, i.e. the nominal downwind direction. The first-order wave excitation forces are approximately zero for sway, roll and yaw, which is expected for 0° waves in heading direction. Forces for surge, heave and pitch approaches zero for high frequencies. Both surge and pitch approaches zero for low frequencies as well. The maximum force for heave and pitch occurs around 0.6-0.7 rad/s. Surge have also have a peak around 0.6-0.7 rad/s, but its maximum occurs around 1.0 rad/s. There is are a large drop in the excitation force in heave around 0.35 rad/s. This is approximately the same frequency as the cancellation frequency 0.34 rad/s , see section 4.1.5. The drop is therefore expected to be the cancellation effect in heave. The cancellation frequency 0.91 rad/s in heave is also seen to be approximately the following drop after the peak around 0.6-0.7 rad/s. The

excitation force in heave is seen to be zero for frequencies higher than 1.6 rad/s.

The results were compared with the first-order wave excitation forces obtained in the D4.2 report [15]. Low, medium and high are the different mesh sizes and OO is the result from the D4.2 report. The extraction of data from the plots in the D4.2 report was done the same way as for the added mass coefficients in terms of using WebPlotDigitizer. The comparison shows a good match to the D4.2 report with respect to shape and values. The differences in the results are largest in the high frequencies in surge. This is assumed to be mainly the lack of wave frequencies in high frequency region in the Wadam run. HydroD only allows 60 different wave frequencies for one Wadam run and these were more concentrated in the lower frequency regions. The accuracy of the results in the D4.2 report may also be questioned with respect to the number of wave frequencies around the peaks used in the report and the extraction of the results from the report. There is some small difference in the peaks where the results from Wadam have larger values than the D4.2 report. The different mesh sizes shows more or less the same results.

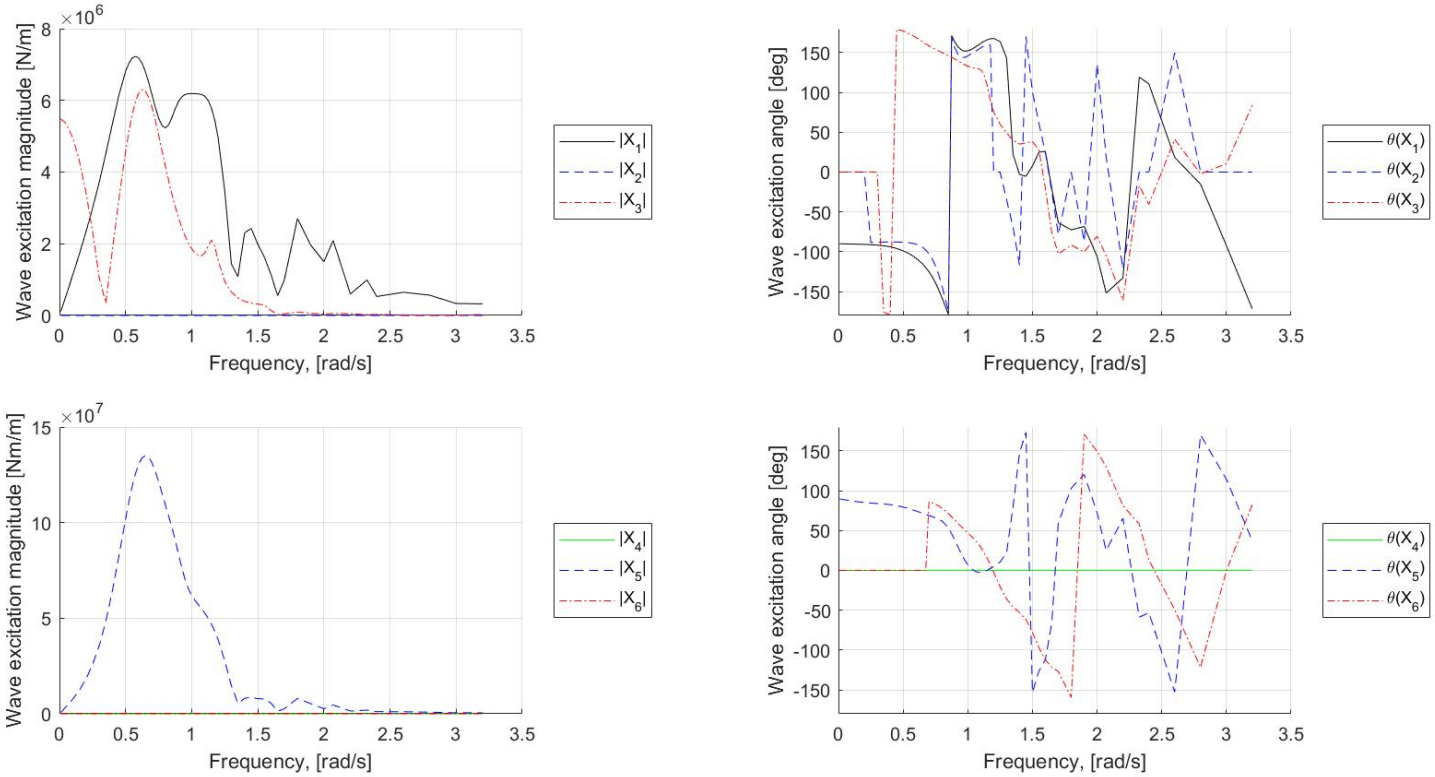

Figure 4.9: OO-Star Wind Floater Semi 10MW hydrodynamic wave excitation forces from HydroD-Wadam (results are given for 0° wave heading direction).

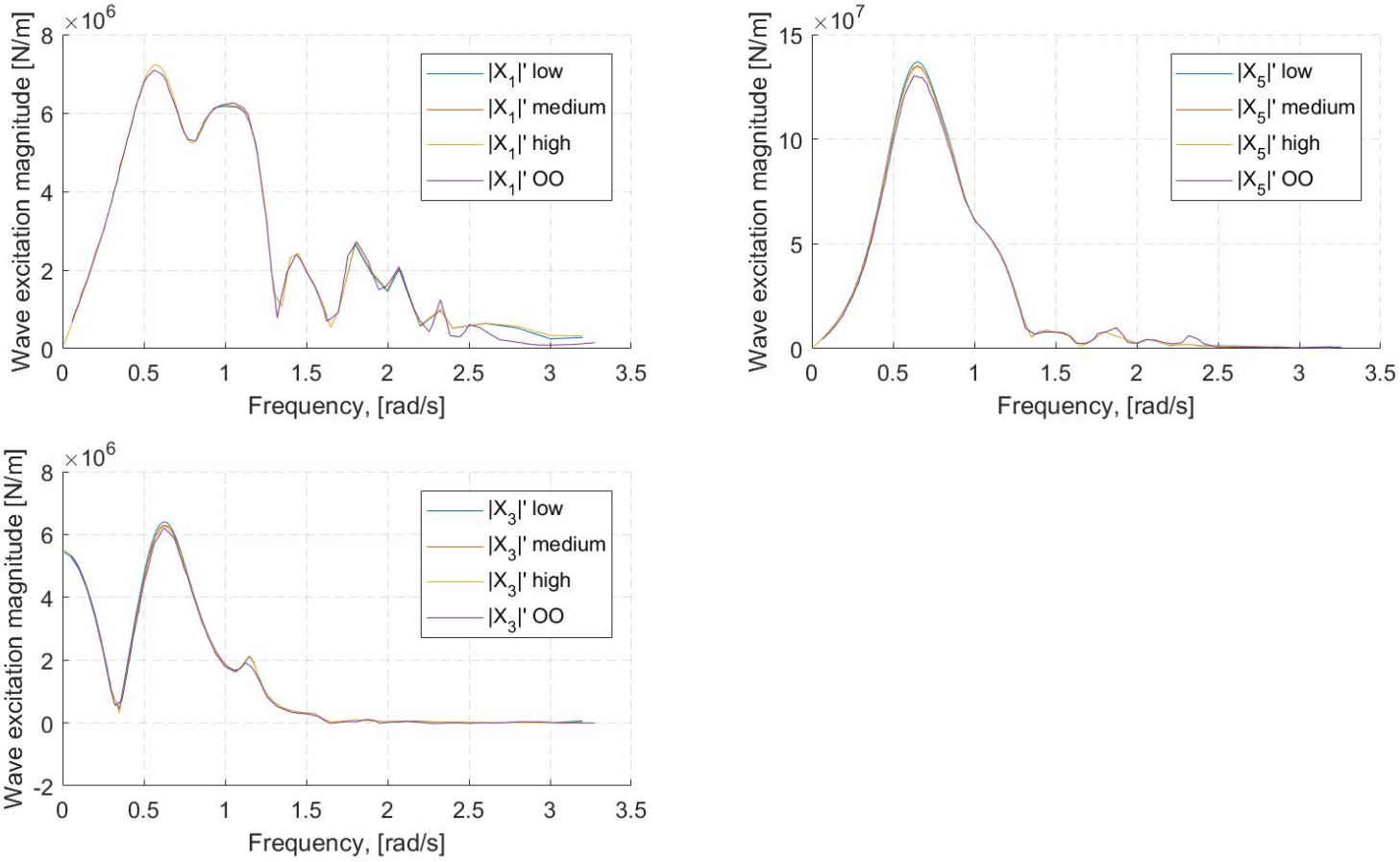

Figure 4.10: OO-Star Wind Floater Semi 10MW hydrodynamic wave excitation forces from HydroD-Wadam (results are given for 0° wave heading direction). Low, medium and high are different mesh sizes and OO is from the life50+ report.

4.1.3 Hydrostatic stiffness

A MATLAB script was developed to calculate the hydrostatic stiffness coefficients for the hull. The calculations were based on eq.(2.44)-(2.47) from the hydrostatic loads section. The restoring term from the difference of center of buoyancy and gravity was excluded from the hydrostatic stiffness matrix. The reason for doing it was that the term got accounted for a different way in the RBP model. This way was to include gravity in the SIMO-body representing the hull and put on a specified force representing the buoyancy of the structure. The center of gravity and the center of buoyancy were set to (0,0,-15.225) and (0,0,14.236), respectively. This meant that the hydrostatic stiffness matrix only accounted for water plane stiffness. The cross terms was set equal to zero due to symmetry of the structure. Input parameters and results can be seen in Table 4.4.

Table 4.4: Input and calculated parameters for hydrostatic stiffness.

Variable	Unit	Value
Displaced water volume	m^3	23509
Center of buoyancy below MSL	m	-14.236
Overall substructure mass	kg	$2.1709 \cdot 10^7$
Center of mass below MSL	m	-15.225
Density water	kg/m^3	1025
Gravity acceleration	m/s^2	9.81
Water plane area (still water)	m^2	549.71
Hydrostatic stiffness coeff. C_{33}	N/m	$5.5275 \cdot 10^6$
Hydrostatic stiffness coeff. C_{44}	Nm/rad	$2.9725 \cdot 10^9$
Hydrostatic stiffness coeff. C_{55}	Nm/rad	$2.9725 \cdot 10^9$

4.1.4 SIMO-RIFLEX model

The computer program SIMA was used for the coupled dynamic analysis. The RBP model was generated in SIMA as a SIMO-RIFLEX model. A SIMO-body was used to represent the hydrodynamic loads on the hull and RIFLEX beam elements were used to represent the tower and mooring system. The wind turbine was simplified to a SIMO-body as well with the properties listed in Table 3.1. The reasons behind this are explained before. The frequency-dependent added-mass, radiation damping and first-order wave excitation for the hull from HydroD was implemented in the SIMO-body representing the hull. The calculated hydrostatic stiffness coefficients from MATLAB were also implemented in the same SIMO-body.

The values used for the different variables in the SIMO-RIFLEX model in SIMA were based on the D4.2 report [15]. Most of the used data can also be seen in Table 3.2-3.4. Gravity was included in the SIMO-bodies representing the hull and the wind turbine. A specified force representing the buoyancy of the structure was included in the SIMO-body representing the hull. The center of gravity for the hull and the center of buoyancy for the specified force were set to (0,0,-15.225) and (0,0,14.236), respectively. The specified force was calculated by eq.(4.2) and input values was taken from Table 4.4. V is the displaced water volume. The specified force was calculated to be 2.3639E+08 N.

$$\text{Specified force} = \rho g V \tag{4.2}$$

The results from one static analysis were checked to get an indication if the modelling was done correct. The coordinates of the SIMO-body representing the hull, the pre-tension in mooring lines and the axial force in the bottom element of the tower were checked. The environment for the analysis was set as a constant wind test with significant wave height Hs=0.001 m, peak period Tp = 20 s and constant wind

speed Ws = 0.001 m/s. The results can be seen in Table 4.5. The results were close to what was expected. A small displacement in the x direction, and a small rotation in pitch. The axial force in the mooring lines were close to the pretension of 1670 kN. The small difference between the pretension in the mooring lines is assumed to be because of the environment. The axial force in the bottom tower element was identical to the 18535 kN calculated from the D4.2 report [15].

Table 4.5: Simple static analysis for constant wind test.

Variable	**Unit**	**D4.2 report**	**RBP model**
Coordinates	m	[-]	[-0.1097,0,0.065]
Angles	deg	[-]	[0,-0.2452, 0]
Pretension line 1	kN	1670	1629
Pretension line 2,3	kN	1670	1631
Axial force tower element	kN	18535	18535

Viscous effects

The hydrodynamic loads on the OO-Star Wind Floater Semi 10MW cannot be properly described using only potential theory. Viscous effects need to be included as well and were accounted for by adding quadratic drag in slender elements in the RBP model. The quadratic drag forces were calculated by the drag term in Morison's equation (2.38) in horizontal and vertical direction. The hull of the OO-Star Wind Floater Semi 10MW was simplified to cylindrical elements. The drag coefficients for each of the structural parts were taken from the D4.5 report [38] and were based on the Reynolds number (Re) and Keulegan-Carpenter number (KC). The drag coefficients together with the quadratic drag terms are listed in Table 4.6. Figure 4.11 shows the RBP model in SIMA. The blue elements are the slender elements which contains the quadratic drag for that structural part, enumerated as in Table 4.6.

Table 4.6: OO-Star Wind Floater Semi 10MW drag coefficients and quadratic drag terms.

Structural part	Number	Drag coefficient C_D[-]	Diameter[m]	Quadratic drag [kg/m^2]
Outer column top part horizontal	1	0.7200	13.400	$4.9446 \cdot 10^3$
Outer column cone part horizontal	2	0.7130	14.600	$5.3350 \cdot 10^3$
Outer column bot part horizontal	3	0.7060	15.800	$5.7168 \cdot 10^3$
Outer column shirt part vertical	4	10.0000	22.800	$116.8500 \cdot 10^3$
Central column top part horizontal	5	0.7290	12.050	$4.5020 \cdot 10^3$
Central column cone part horizontal	6	0.7165	14.125	$5.1868 \cdot 10^3$
Central column bot part horizontal	7	0.7040	16.200	$5.8450 \cdot 10^3$
Pontoons vertical	8	2.0500	7.000	$17.8606 \cdot 10^3$
Pontoons horizontal	8	2.0500	17.000	$7.3544 \cdot 10^3$

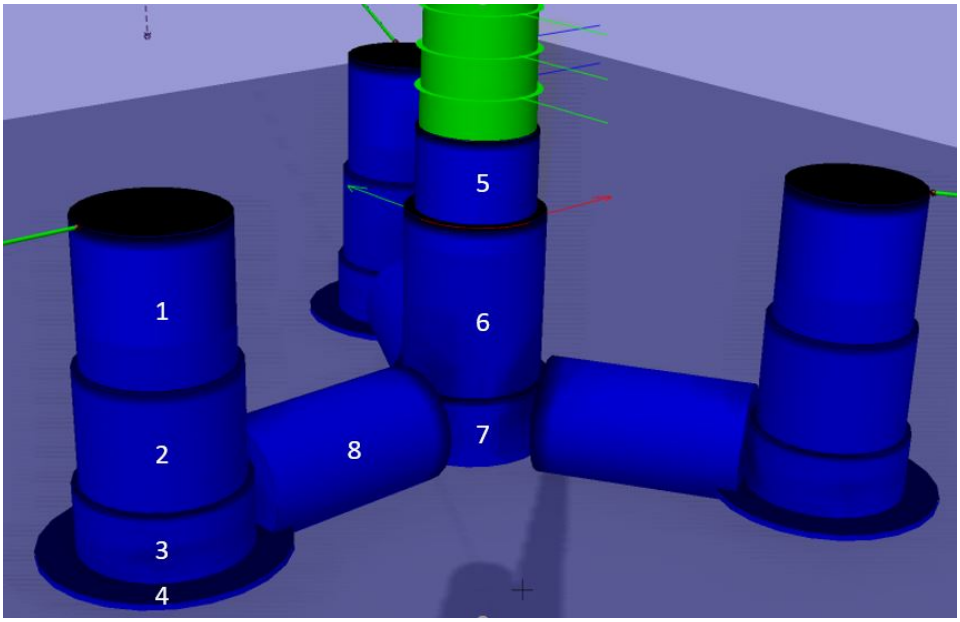

Figure 4.11: Rigid body potential (RBP) model in SIMA. Blue elements are slender elements enumerated as in Table 4.6.

4.1.5 Hand calculations

Natural period in heave

Hand calculations were made to get an estimate for the natural period in heave for the OO-Star Wind Floater Semi 10MW. This was done by simplifying the heave motion η_3 to a linear single degree of freedom system (SDOF), see Figure 4.12. The equation for SDOF can be written as:

$$(M + A_{33})\ddot{\eta_3} + B_{33}\dot{\eta_3} + C_{33}\eta_3 = F_3(t) \tag{4.3}$$

where M is the mass of the system and $F_3(t)$ is the vertical excitation force. A_{33}, B_{33} and C_{33} are the the added mass, damping and restoring coefficients in heave. The undamped natural period (B_{33}=0) can then be found as:

$$T_3 = 2\pi\sqrt{\frac{M_{33} + A_{33}}{C_{33}}} \tag{4.4}$$

The mass of the total structure was taken from the D4.2 report [15] to be M = 2.3618·10^7 kg. This included the mass of the ballasted platform, the tower and the combined tower top masses. The mass of the mooring lines were neglected. The added mass in heave was taken from the added mass plot from Wadam for the RBP model, see Figure 4.5. The added mass value was taken to be A_{33} = 3.56·10^7 kg, the value corresponding to ω = 0.314 rad/s. This value was chosen since most semi-submersibles have approximately T = 20 s as natural period in heave [22]. The restoring stiffness was taken from Table 4.4 as C_{33} = 5.5275·10^6 N/m. By inserting these values into eq. (4.4) the natural period in heave was calculated to be T_3 = 20.57 s. It is therefore expected that the natural period in heave will be relatively close to this value for the OO-Star Wind Floater Semi 10MW.

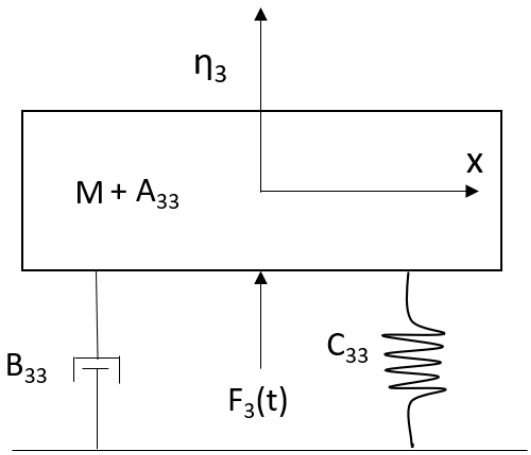

Figure 4.12: Illustration of heave motion as a single degree of freedom system [33].

Cancellation period in heave

The wave cancellation effect can be import for a semi-submersible because it may improve the wave-induced dynamic response. This phenomenon occurs when the wave force acting on the submerged parts of the semi-submersible with different phases canceled each other out because of the phase shift [41]. An estimation of the cancellation period in heave for the OO-Star Wind Floater Semi 10MW was found by considering the vertical excitation force $F_3(t)$. Potential theory, regular sinusoidal waves and long wavelength relative to the cross section is assumed. The main contribution to $F_3(t)$ for a semi-submersible will be the pressure on the pontoons. An example from "Sea loads on ships and offshore structures" [22] for a semi-submersible that consisted of two pontoons with columns on each floater is followed to estimate the cancellation period in heave. The following equations are derived for the example semi-submersible in beam sea, see Figure 4.13a. By a strip theory approach, the vertical excitation force on the semi-submersible from the pressure on the pontoons can be written as:

$$F_3(t) = \rho g \zeta_a sin(\omega t) e^{kz_m} cos(kB/2)(A_w e^{k(z_t - z_m)} - k(V_p + \frac{A_{33}}{\rho})) \tag{4.5}$$

where k is the wave number, z_m and z_t are the z-coordinate for the geometric centre and top of the pontoon, and B is the distance between the centre planes of each pontoon. A_w is the waterplane area and V_p is the total volume of the pontoons. By assuming k(z_t-z_m) to be small an approximation to eq.(4.5) can be done:

$$F_3(t) = \rho g \zeta_a sin(\omega t) e^{kz_m} cos(kB/2)(\rho g A_w - \omega^2(M + A_{33}) - \rho \omega^2 A_w z_m) \tag{4.6}$$

Inserted into eq.4.3, neglecting damping and $C_{33} = \rho g A_w$ it follows:

$$\frac{\eta_3}{\zeta_a} = sin(\omega t) e^{kz_m} cos(kB/2)(1 - \frac{kz_m}{1 - (\frac{\omega}{\omega_n})}) \tag{4.7}$$

where ω_n is the natural circular frequency in heave. From this equation it can be seen that the heave motion goes to infinity if ω=ω_n. This is because viscous effects are neglected and therefore unrealistic. It follows from eq.(4.7) that the heave motion is zero when:

$$\omega = \frac{\omega_n}{(1 - |z_m| \frac{\omega_n^2}{g})^{\frac{1}{2}}} \tag{4.8}$$

or cos(kB/2)=0. The geometry of the semi-submersible in the example and OO-Star Wind Floater Semi 10 MW are different. It is assumed that the cancellation period in heave occurs for OO-Star Wind Floater Semi 10 MW when the wave amplitude on the back pontoons is half of the wave amplitude on the front pontoon, see Figure 4.13b. This leads to B being twice the length from the middle part of the front pontoon to the center column. The cancellation frequency for cos(kB/2)=0 can then be found by using

the dispersion relation eq. (2.39) as:

$$\omega = \sqrt{\frac{g(\pi + 2\pi n)}{B}} \quad n = 0, 1, 2.. \tag{4.9}$$

The smallest frequency where the theoretical heave value is zero is usually found from eq.(4.8). A geometric centre of the pontoons can be approximated to be z_m = -18.5 m and the natural period in heave was calculated to be T_n = 20.57 s. Inserting these values into the eq.(4.8) gives the cancellation frequency ω = 0.34 rad/s. This results in a cancellation period T = 18.48 s. The first and second cancellation frequencies found by eq.(4.9) and B = 37 m are ω = 0.91 rad/s and ω = 1.58 rad/s, respectively. As mentioned in a previous section, a large drop in excitation force in heave was seen around 0.35 rad/s. This is assumed to be the smallest cancellation frequency calculated to be 0.34 rad/s. The cancellation frequency 0.91 rad/s in heave was also seen to be approximately the following drop after the peak around 0.6-0.7 rad/s. The excitation force in heave was seen to be zero from frequency 1.6 rad/s and out. This is probably the reason why the cancellation frequency ω = 1.58 rad/s is not seen.

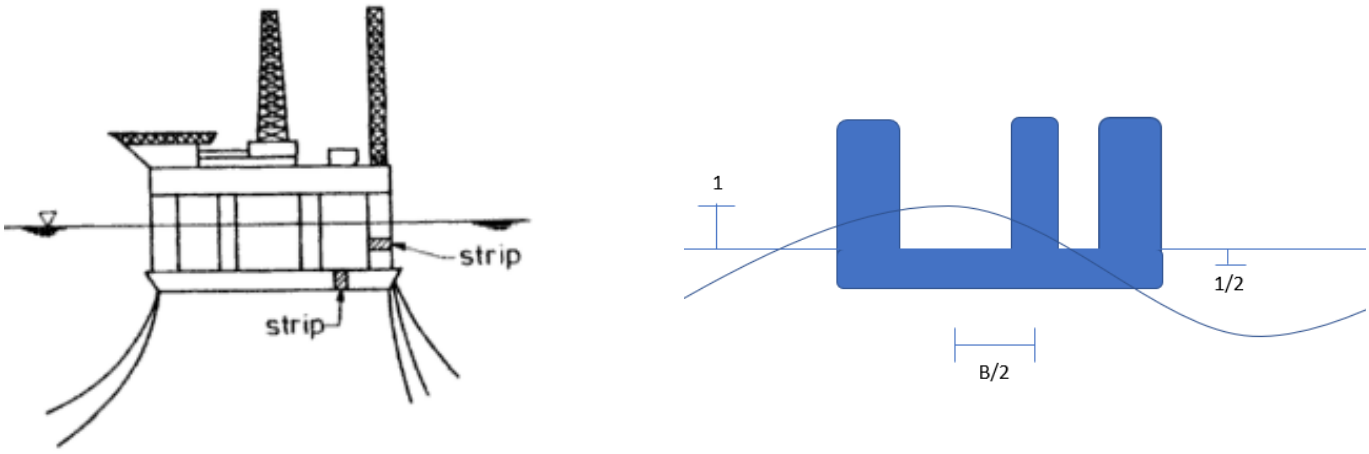

(a) Semi-submersible

(b) OO-Star Wind Floater Semi 10 MW

Figure 4.13: Sketch of the semi-submersible used in the example [22]. Illustration of the cancellation period for OO-Star Wind Floater Semi 10 MW.

4.1.6 Decay tests

Decay tests were performed on the RBP model in SIMA in order to obtain and document the natural periods and damping for the system. The system have been modelled to have both linear and quadratic damping contribution in each degree of freedom (DOF). The damping contributions can be separated into structural and hydrodynamic damping. When it comes to hydrodynamic damping both linear and

nonlinear are included in the SIMO-RIFLEX model in SIMA. The linear damping is included in the SIMO-body representing the floating platform, while nonlinear damping is accounted for by the slender elements of the floating platform with quadratic drag. Surge, heave, pitch and yaw were the motions that were considered for the decay tests due to symmetry of the hull.

Each of the DOFs were considered separately in order to find and evaluate the natural periods and damping coefficients. All simulations were done by applying a ramp force, followed by a constant force for a time period before removing the force and releasing the model. An illustration of this can be seen in Figure 4.14. After releasing the model, the motion will decay and oscillate about the equilibrium with the damped natural frequency. This can be observed in the time series, and the damped natural periods can be calculated together with the damping coefficients. Load, ramp duration, constant force duration and total simulation time for each of the motions are given in Table 4.7.

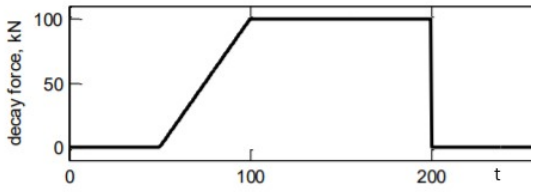

Figure 4.14: Example of a decay force.

MATLAB-scripts provided in the subject module *Integrated dynamic analysis of wind turbines* at NTNU were used for the post-processing part in order to do the calculations for the damped natural periods and damping coefficients. The time series together with the calculated natural period and damping coefficients are presented for each motion in the following paragraphs. T_0 is the natural period, b_1 is the linear damping coefficient and b_2 is the quadratic damping coefficient for the given motion. The recreated motion given by b_1 and b_2 are plotted together with the time series for comparison. See section 2.5 for more theory related to the decay tests.

It was seen that for some motions the recreated curve (red) did not fit well with the time series from the decay tests (blue). The reason for this was that the script took the point after the release of the structure as a peak/trough, even though it was not. This problem was fixed by neglecting the point after the release of the structure. Another problem was that some of the times series did not oscillate around zero and this is one of the assumption behind the script. This was fixed by adding or subtracting a constant value to all values in the time series.

Table 4.7: Simulation specifications for decay tests for the RBP model.

Motion	Force/ moment	Ramp duration	Constant force duration	Total simulation time
Surge	500 kN	100 s	200 s	1200 s
Heave	7000 kN	50 s	100 s	400 s
Pitch	36000 kNm	50 s	100 s	600 s
Yaw	5000 kNm	50 s	100 s	800 s

The natural periods stated in the D4.2 report [15] and the RBP model are compared in Table 4.8. The percentage difference between the natural periods are calculated as:

$$\% = \frac{T_R - T_D}{T_D} \cdot 100\% \tag{4.10}$$

where T_R and T_D are the natural periods for the RBP model and the D4.2 report, respectively. The largest difference is found for the yaw motion with -10.89%. It is assumed that the natural periods in surge and yaw are strongly connected to the mooring system. There may be differences between the mooring system used in the RBP model and the mooring system used in the D4.2 report [15]. The results from static analysis where the pretension in the mooring lines from the RBP model were compared with the pretension stated in the D4.2 report showed a difference. This indicates that the mooring systems are not exactly the same. The differences in natural periods in surge and yaw are not considered to be important since the periods are high and will not be excited by linear wave excitation forces.

The natural periods in heave are seen to be more or less the same and in good agreement with hand calculated natural period T = 20.57 s. The difference in natural periods in pitch is more uncertain. It is not known how the quadratic drag is calculated in the D4.2 report. However, this is not likely to be the reason for the difference since damping rarely change the natural periods much [27]. The restoring stiffness, which includes the effects of water plane area and buoyancy, from the D4.5 report [38] were compared with the RBP model. This showed a difference, $-4.1280 \cdot 10^8$ in the D4.2 report and $-3.9369 \cdot 10^8$ in the RBP model. This difference is approximately -4.6%, but by including the restoring stiffness from the mass distribution it is less than 0.7% of the total restoring stiffness. Therefore, it is assumed that this is not the reason for the difference in the natural periods in pitch. The total mass of the RBP model, excluding the mooring system, were compared with the D4.2 report. This showed a small difference, $2.3618 \cdot 10^7$ kg in the D4.2 report and $2.3642367 \cdot 10^7$ kg in the RBP model, which is less than 0.1%. The difference was not further investigated. Simplifications of the wind turbine or tower, or misinterpretation of values in the D4.2 report [15] could be reasons for the difference, but this is only speculations. The axial force in the bottom tower element was checked in the static analysis, and was identical to the D4.2 report.

Table 4.8: Comparison of natural periods from the D4.2 report [15] and the RBP model.

Motion	Natural period from D4.2 report[s]	Natural period from RBP model[s]	Deviation
Surge	181.82	186.69	2.68%
Heave	20.41	20.60	0.94%
Pitch	31.25	29.27	-6.34%
Yaw	116.28	103.62	-10.89%

Decay test surge

Table 4.9: Natural period and damping coefficients for surge.

Parameter	Unit	Value
T_0	[s]	186.69
b_1	[s^{-1}]	0.000221
b_2	[m^{-1}]	0.017242

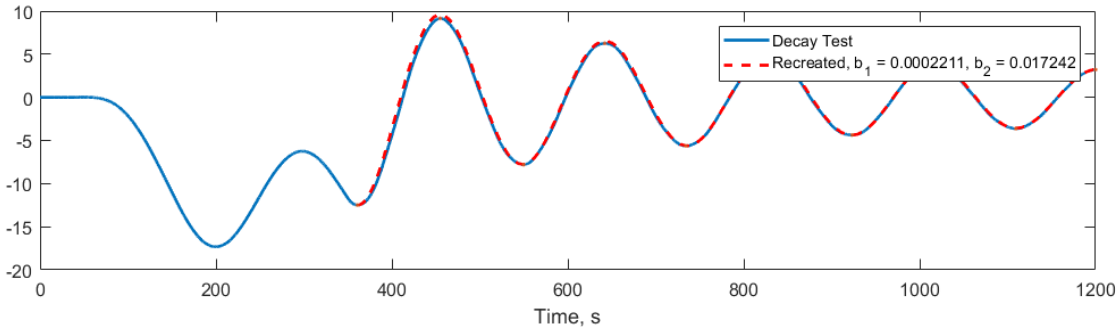

Figure 4.15: Surge motion: Time series plotted together with the recreated motions given by b_1 and $b2$

Decay test heave

Table 4.10: Natural period and damping coefficients for heave.

Parameter	Unit	Value
T_0	[s]	20.60
b_1	[s^{-1}]	0.000012
b_2	[m^{-1}]	0.026731

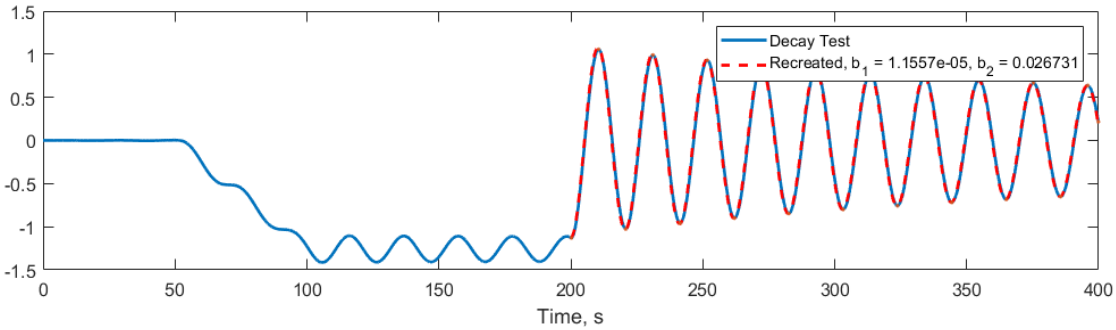

Figure 4.16: Heave motion: Time series plotted together with the recreated motions given by b_1 and $b2$

Decay test pitch

Table 4.11: Natural period and damping coefficients for pitch.

Parameter	Unit	Value
T_0	[s]	29.27
b_1	[s^{-1}]	0.002867
b_2	[m^{-1}]	0 (negative)

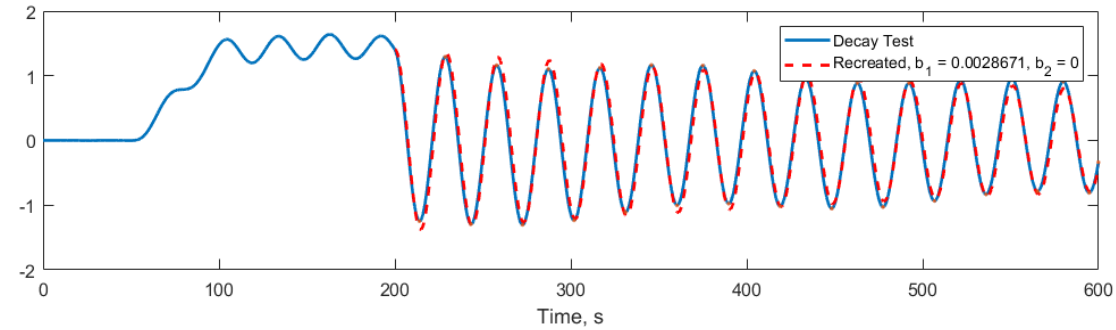

Figure 4.17: Pitch motion: Time series plotted together with the recreated motions given by b_1 and $b2$

Decay test yaw

Table 4.12: Natural period and damping coefficients for yaw.

Parameter	Unit	Value
T_0	[s]	103.62
b_1	[s^{-1}]	0.000217
b_2	[m^{-1}]	0.018417

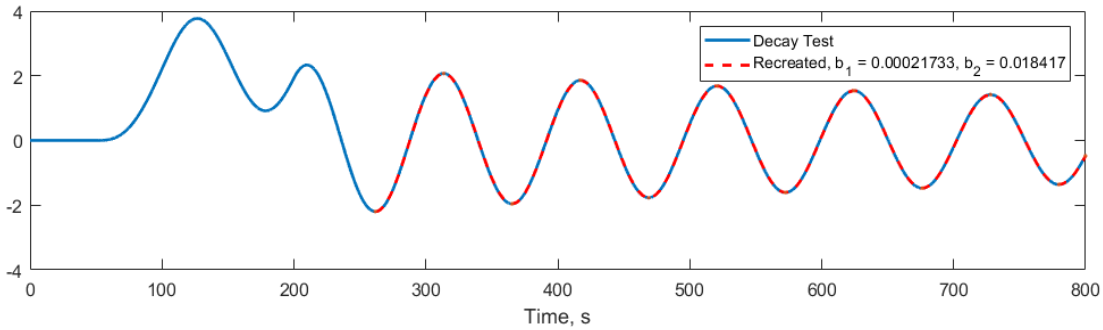

Figure 4.18: Yaw motion: Time series plotted together with the recreated motions given by b_1 and $b2$

4.1.7 Regular waves test

A regular waves test was performed on the RBP model to analyse the response of the model for different wave frequencies. The regular waves test was done by simulations in SIMA. Regular incident waves with a given frequency ω were generated in each simulation run of the test and the motions and loads were measured. The wave direction of the waves was 0°, which is the nominal downwind direction. The wave time series used in a simulation run was made as a harmonic wave signal by eq.(4.11) with unit amplitude, ζ_a=1 m. A text file for each wave time series was generated by a MATLAB script and used in SIMA. The given frequency for the incident waves in each simulation run was varied to cover the dominant wave frequency components usually found in a wave spectrum. A total of 17 different regular waves simulation runs were performed on the RBP model, varying the wave period from 4-20 s. The simulation time for each simulation run was set to 1000 s. An example of a wave time series with period T = 10 s used in a simulation run in the regular waves test is shown in Figure 4.19. In Table 4.13 are the input values for the wave time series used in each simulation run in the regular waves test listed.

$$\zeta = \zeta_a cos(\omega t) \tag{4.11}$$

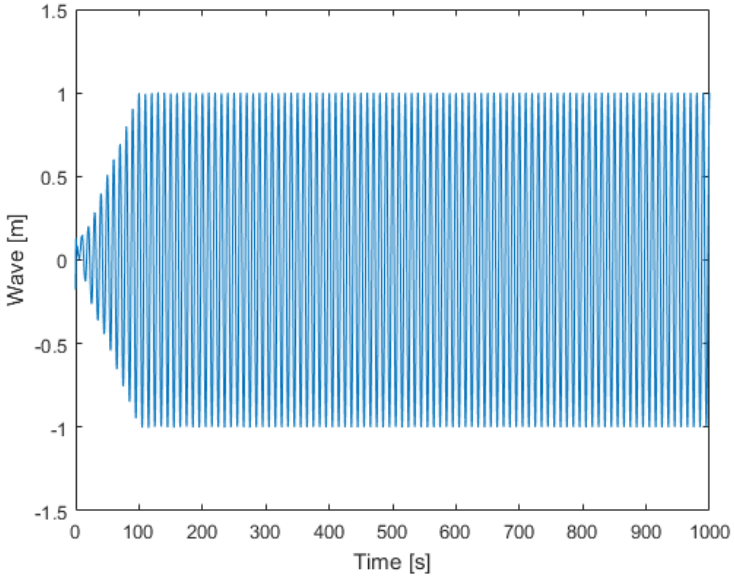

Figure 4.19: Wave time series with period T = 10 s used in a run in the regular waves test.

Table 4.13: Input values for the wave time series in the regular waves test

Simulation run number	**Wave period T [s]**	**Wave frequency ω [rad/s]**	**Wave amplitude ζ_a [m]**
1	4	1.5708	1
2	5	1.2566	1
3	6	1.0472	1
4	7	0.8976	1
5	8	0.7854	1
6	9	0.6981	1
7	10	0.6283	1
8	11	0.5712	1
9	12	0.5236	1
10	13	0.4833	1
11	14	0.4488	1
12	15	0.4189	1
13	16	0.3927	1
14	17	0.3696	1
15	18	0.3491	1
16	19	0.3307	1
17	20	0.3142	1

The response amplitude operator (RAO) for different motions was calculated to analyse the results from the regular waves test. A MATLAB-script was developed for the post-processing of the results. The time

series of the motions had longer transient phases then anticipated. One way to solve this problem for the time series was to increase the simulation time and extract the amplitude of the motions directly from the time series after the transient phases. Another way was to transform the time series into the frequency domain using fast Fourier transform (FFT) and extract the amplitude of the component of the motion with the same frequency as the incident wave. By doing it this way only the linear wave excitation will remain. The last option was chosen. A high-pass filter was used on the time series of motions to remove the frequency below the incident wave frequency. This was seen to be sufficient since the frequencies in the time series were lower or up to the incident wave frequency. A built-in function in MATLAB called "designfilt()" was used in the script. Specifications to the high-pass filter are listed in Table 4.14. f is the frequency of the incident wave in hertz. The time series of heave motion for the RBP model with incident wave period T = 10 s from the regular waves test is shown in Figure 4.20 as an example. The orange and blue lines are the time series with or without filter, respectively.

Table 4.14: Input values for built-in filter function in MATLAB. f is the frequency of the incident wave in Hz.

Parameter	**Unit**	**Value**
Highpassir	[-]	-
Filter order	[-]	6
Passband frequency	[Hz]	f-0.001
Passband ripple	[dB]	0.2
Sample rate	[Hz]	10

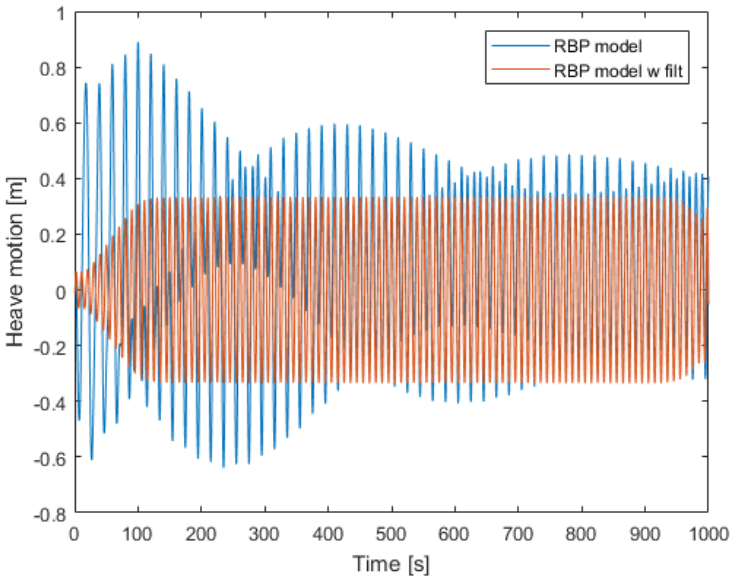

Figure 4.20: Time series of heave motion for the RBP model with incident wave period T = 10 s from the regular waves test. The orange and blue line are the time series with or without filter, respectively.

FFT were used on the time series of motions after they were filtered to transform the results into the frequency domain. The spectral response could then be calculated and a one-sided power spectral density (PSD) were created. PSD refers to the spectral energy distribution that would be found per unit time of a signal, and describes the distribution of energy into frequency components composing the signal [42]. A time series from the regular waves test will only contain energy around the incident wave frequency because of the filter. An example can be seen in figure 4.21 which shows the PSD for surge motion for the RBP model. Each of the peaks corresponds to an incident wave frequency from a simulation run. The height at the peaks are connected to the amplitude of the surge motion. Different frequencies will give different amplitudes in surge. This is similar to a frequency domain solver, but the calculations are based on time domain simulations. The RAO were calculated from the PSD using the following equation [43]:

$$RAO = \sqrt{\frac{m_{peak}}{\zeta_{peak}}} \tag{4.12}$$

where m_{peak} is the peak of the motion PSD and ζ_{peak} was the peak of the wave elevation PSD. The PSD and RAO were calculated for surge, heave and pitch motion since the rest of the motions were zero because of the wave direction. The results can be seen in Figure 4.21 - 4.26.

The RAO for surge motion is increasing for increasing period. The largest value in the RAO for surge motion is seen to be more than 1.6 for period 20 s. This is a large value and may not be realistic. It is believed to be connected to lack of damping. The spectral density for surge motion varies with increasing period, but the trend is increasing spectral density. The RAO for surge motion goes towards zero as the period goes towards 4 s. The spectral density for surge motion for frequencies higher than 0.17 Hz are more or less zero. The RAO for heave motion shows a large value for 20 s period. This is as expected since the natural period in heave is close to this period. However, this value is not realistic and occurs because of lack of damping. Also, the RAO for heave motion is approximately zero around period 15 s. This could be the previous calculated cancellation period 18.48 s which have been moved due to the quadratic drag. There is a peak in the RAO for heave motion at period 11 s. The RAO for heave motion goes towards zero as the period goes towards 4 s. The same trends mentioned for the RAO are seen in the PSD for heave motion. The spectral density for heave motion for frequencies higher than 0.15 Hz are more or less zero. The RAO for pitch motion also shows a large value for 20 s period. There is a peak in the RAO for pitch motion at period 9 s. The RAO for pitch motion goes towards zero as the period goes towards 4 s. The same trends mentioned for the RAO are seen in the PSD for pitch motion. The spectral density for pitch motion for frequencies higher than 0.15 Hz are more or less zero.

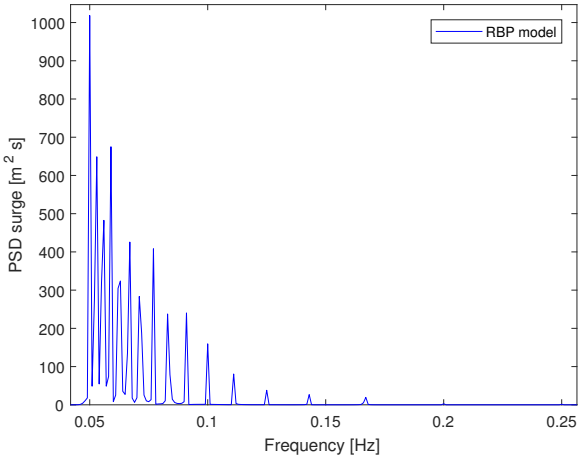

(a) PSD

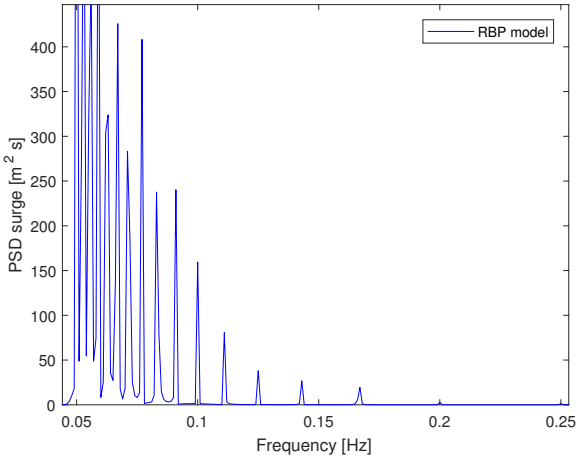

(b) PSD zoom in

Figure 4.21: The PSD for surge motion for the RBP model from the regular waves test.

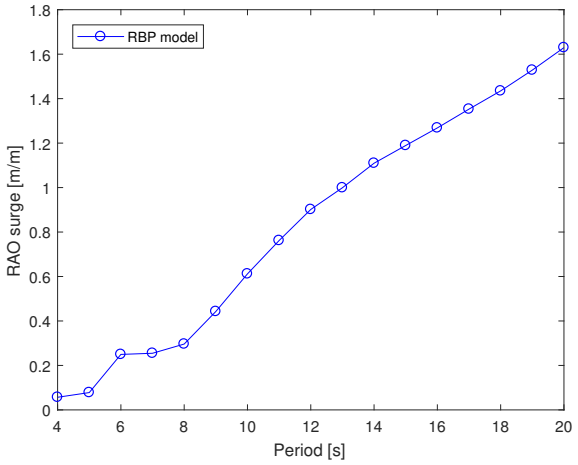

(a) RAO

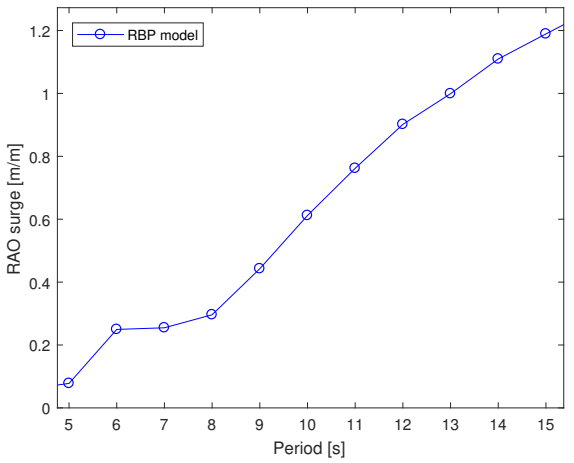

(b) RAO zoom in

Figure 4.22: The RAO for surge motion for the RBP model from the regular waves test.

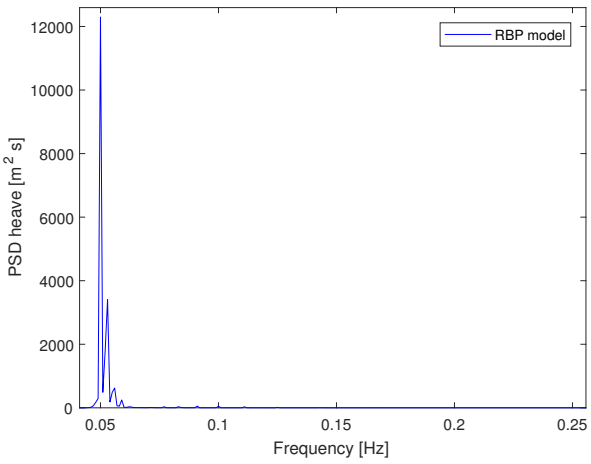

(a) PSD

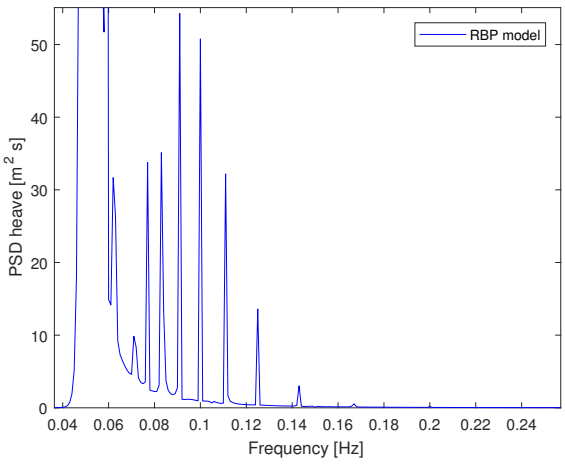

(b) PSD zoom in

Figure 4.23: The PSD for heave motion for the RBP model from the regular waves test.

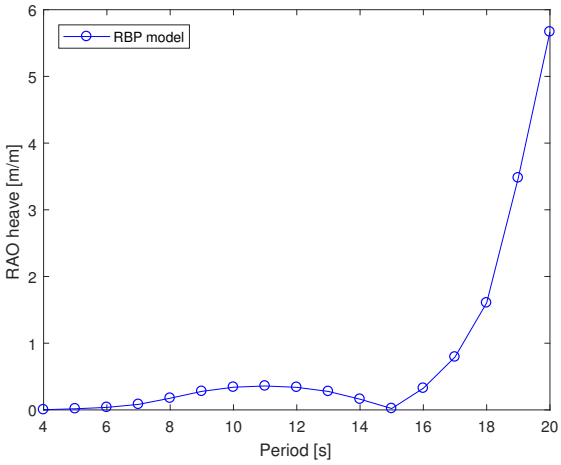

(a) RAO

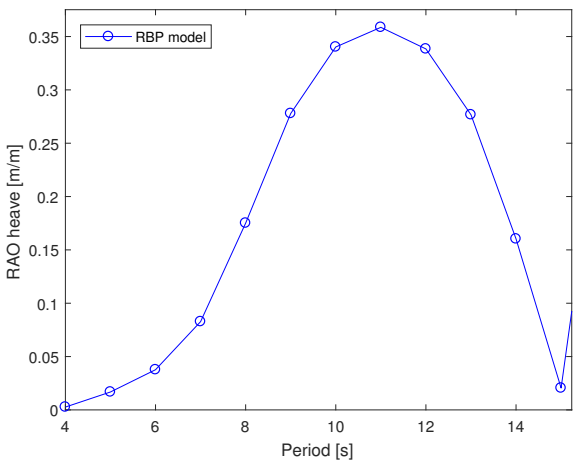

(b) RAO zoom in

Figure 4.24: The RAO for heave motion for the RBP model from the regular waves test.

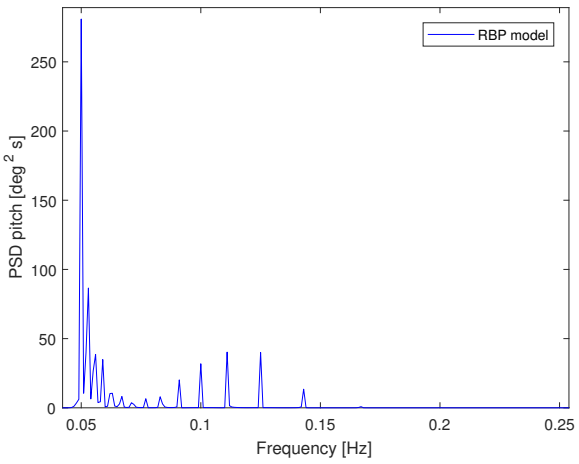

(a) PSD

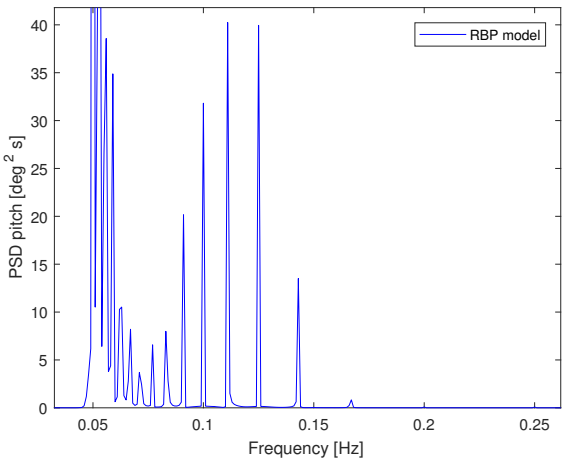

(b) PSD zoom in

Figure 4.25: The PSD for the pitch motion for the RBP model from the regular waves test.

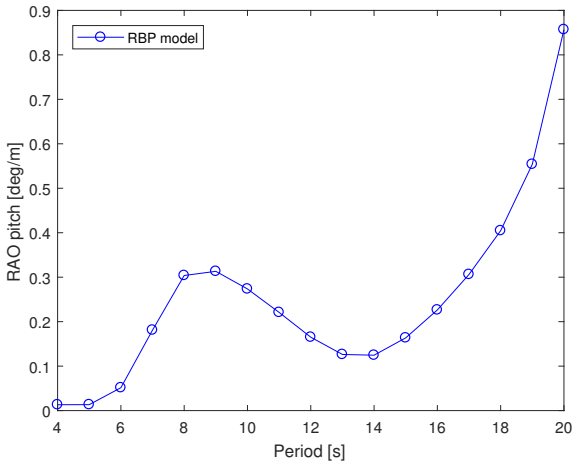

(a) RAO

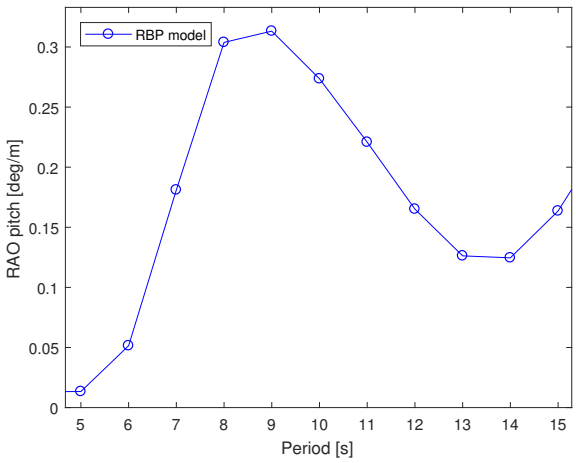

(b) RAO zoom in

Figure 4.26: The RAO for the pitch motion for the RBP model from the regular waves test.

The energy in a wave spectrum $S(\omega)$ is usually calculated by solving the equation [33]:

$$\frac{1}{2}\zeta_a^2 = S(\omega)\Delta\omega \tag{4.13}$$

where ζ_a is the wave amplitude and $\Delta\omega$ is the frequency interval. Theoretically should the PSD for the wave elevation have the same value at the peaks for the different incident wave frequencies in the regular waves test simulations. This is because the wave amplitude was set to 1 m in all the simulations. Ideally would the peaks in the PSD for the wave elevation be impulses. However, this is not the case

in practise. The combination of the filter used on the time series and frequency step makes the values at the peaks different from each other, varying from 197-465 m^2 s. The area around the peaks are the approximately the same, but the width and height are different. Also, the width around the peaks and the frequency interval are similar in size. A small difference between the peak frequencies in the PSD and the frequencies in the regular waves test can make a large difference due to the steepness of the peaks. Figure 4.27a shows the PSD of the wave elevation from the regular waves test for the RBP model. The peaks at frequencies 0.167 Hz and 0.20 Hz illustrates the difference in peak values. A difference between the values of the peaks in the PSDs for wave elevation in different hydrodynamic models were also found. Figure 4.27b shows this for the RBP model and the RBM model. Blue is from the RBP model and red is from the RBM model. However, this difference is relatively small. The problems related the PSDs for wave elevation from regular waves test in the hydrodynamic models were found late in this study and not further investigated. This may had a significant effect on the results from the regular waves tests for the different hydrodynamics models in this study.

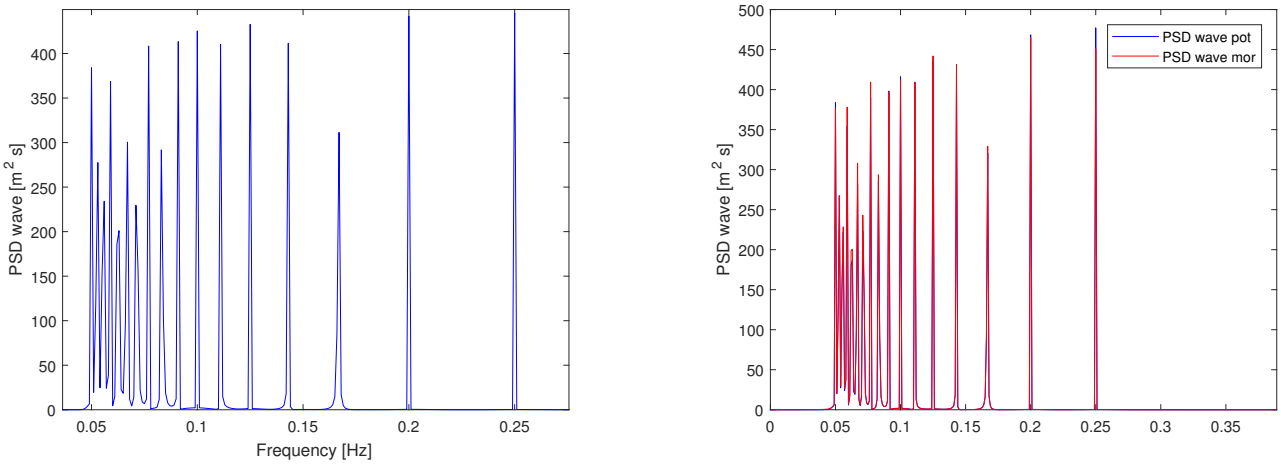

(a) PSD for RBP model

(b) PSD for RBP and RBM model

Figure 4.27: The PSD for wave elevation for the RBP model and the RBM model from the regular waves tests.

4.2 Rigid body model using Morison's equation

The second hydrodynamic model to be made was the rigid body model using Morison's equation, referred to as rigid body Morison (RBM) model. The RBM model was developed from the SIMO-RIFLEX model of the rigid body potential (RBP) model in SIMA. The hydrodynamic loads changed from calculations being based on potential theory to Morison's equation. Added mass, damping and force transfer functions were removed from the SIMO-body representing the floater, and both accelerations terms and quadratic damping terms from Morison's equation were included in the slender elements. Linear damping was not removed from the SIMO-body representing the floater.

The added mass for the acceleration terms in the slender elements representing the hull in SIMA needed to be calculated. First part was to estimate the added mass coefficients in vertical and horizontal direction. Second part was to calculate the added mass for the acceleration terms for each of the structural part represented by slender elements. The RBM model was finished after inserting the acceleration terms into the slender elements. Figure 4.28 shows the RBM model in SIMA which looks the same as the RBP model in Figure 4.1. Decay tests and a regular waves test were performed on the RBM model to analyse the motion responses of the model. The results from the tests were also compared against the results from the RBP model. The following sections will give more details on how each of the steps in the modeling procedure were done to create the rigid hull model and the reasoning behind it. The results from the tests with discussion will also be presented.

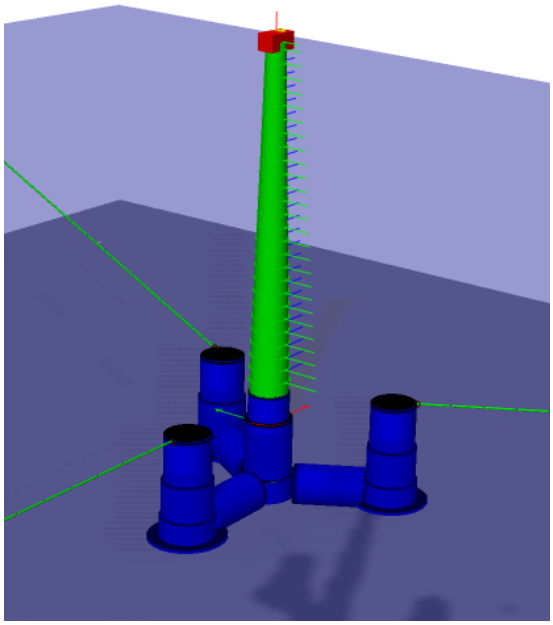

Figure 4.28: The rigid body using Morison's equation (RBM) model in SIMA.

4.2.1 Added mass

SIMA uses an extended formulation of Morison's equation. This is a more complex formulation then previously presented. The longitudinal force component, F_x, together with the transverse force components, F_y and F_z, on a element with length dx subjected to waves and current can be written as:

$$F_i = dx[(\rho A + m_a^i)\dot{u_i}^I - m_a^i \ddot{r}_i + C_D^i \left|U_i^c + u_i^I - \dot{r}_i\right|(U_i^c + u_i^I - \dot{r}_i) + C_D{}_L^i (U_i^c + u_i^I - \dot{r}_i)] \tag{4.14}$$

where

- i : x,y or z depending on direction in local coordinate system.
- A : external cross-sectional area.
- m_a^x, m_a^y, m_a^z : 2D added mass in local x-, y-and z-directions.
- (r_x, r_y, r_z) : translational structural displacement components in the local coordinate system.
- C_D^x, C_D^y, C_D^z : dimensional quadratic drag coefficients in local x-, y- and z-directions.
- $C_{DL}^x, C_{DL}^y, C_{DL}^z$: dimensional linear drag coefficients in local x-, y- and z-directions.
- (U_x^c, U_y^c, U_z^c) : current velocity components in the local coordinate system.
- (u_x^I, u_y^I, u_z^I) : velocity component of undisturbed wave field in the local coordinate system.

From this formulation of Morison's equation it can be seen that it was necessary to calculate the 2D added mass m_a^x, m_a^y, m_a^z in local x-, y-and z-directions for each of the slender elements in the RBM model. There were several steps of calculations in order to obtain the dimensional added mass for each structural part. These calculations were done by programming a MATLAB script. The different steps are described in the following paragraphs.

First, the added mass coefficients Ca for the total body needed to be calculated. This was done for the horizontal and the vertical directions. The calculations in the horizontal direction was done by eq.(4.15) [44]. Here A_{11} is the added mass for the total body in surge, ρ is the water density and $A_i h_i$ is the volume of the structural part i of the floater under water. The added mass in surge, A_{11}, was estimated to an average constant value from the frequency depended added mass in surge from the RBP model, see the green line in Figure 4.29. The average value was taken in the frequency interval [0.523,0.785] which is the peak periods 8-12 s from the D4.2 report [15]. The average value was calculated to be $A_{11} = 1.640 \cdot 10^7$ kg. Only volume of the floater that would make a significant contribution to the added mass in horizontal direction were added to the calculations. This included the three outer columns, the two pontoons in the back with reduced volumes due to the angle and the cone part of the center column. The pontoons were also simplified to cylinders with 7 m diameter in the horizontal direction. By inserting all of these values into the script the added mass coefficient in horizontal direction was calculated to be C_a^{hor} =

1.082.

$$C_a^{hor} = \frac{A_{11}}{\sum_{n=1}^{N} \rho A_i h_i} \tag{4.15}$$

The added mass coefficient for the vertical direction, also known as heave direction, was calculated in similar way as in horizontal direction by eq. (4.16) [44]. Here A_{33} is the added mass for the total body in heave. The added mass in heave was estimated to average constant value of A_{33} = 3.425·10^7, see the green line in Figure 4.29. Only parts of the floater that would make a significant contribution to the added mass in vertical direction were added to the calculations. This included the heave plates, the pontoons, and the bottom part of the center column. A different equation was used to calculate the contribution from the heave plates, eq. (4.19) [18]. This was to increase the contribution from the heave plates. The pontoons were simplified to cylinders with 17 m diameter in the vertical direction. By inserting all of these values into the script the added mass coefficient in vertical direction was calculated to be C_a^{ver} = 1.647.

$$C_a^{ver} = \frac{A_{33}}{\sum_{n=1}^{N} \rho A_i h_i} \tag{4.16}$$

The 2D added mass m_a^x, m_a^y, m_a^z for each of the slender elements in the RBM model was calculated after calculating the added mass coefficients C_a^{hor} and C_a^{ver}. Eq.(4.19) was used for the heave plates in vertical direction and eq.(4.17) and (4.18) were used for the other parts [18]. m_a^y and m_a^z were the same for the column parts due to symmetry in the horizontal plane. The pontoons were simplified to cylinders with 7 m diameter in horizontal direction and 17 m in vertical direction. All of the calculated 2D added mass for each of the slender elements are listed in Table 4.15. Figure 4.11 shows the slender elements enumerated. Important to remember that the values were assigned to the local coordinate system of the element which means x-axis was longitudinal and y- and z-axis were transverse.

$$m_{a_{col}}^{hor} = \rho C_a^{hor} \pi R^2 \tag{4.17}$$

$$m_{a_{col}}^{ver} = \rho C_a^{ver} \pi R^2 \tag{4.18}$$

$$m_{a_{plate}}^{ver} = \rho C_a^{ver} \frac{2\pi}{3} R^3 \tag{4.19}$$

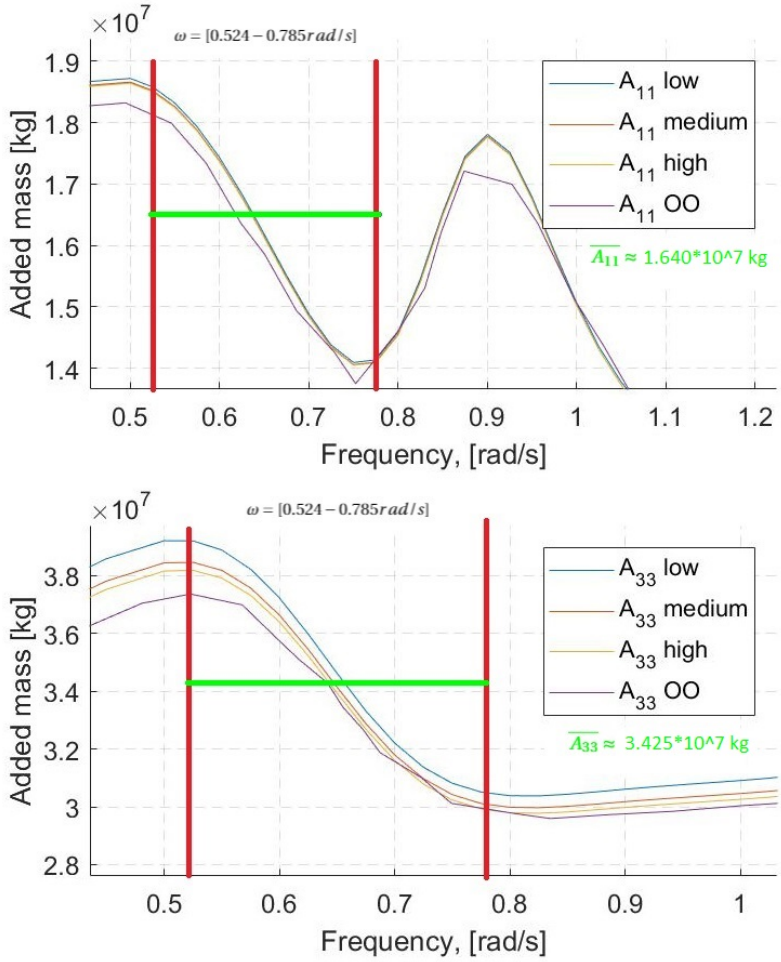

Figure 4.29: Added mass for different frequencies from Wadam in HydroD. Results are given for 0° wave heading direction. Low, medium and high are different mesh sizes, and OO is from the D4.2 report [15].

Table 4.15: Calculated 2D added mass for the different structural parts in the rigid body Morison (RBM) model.

Structural part	**Number**	m_a^x **[kg]**	m_a^y **[kg]**	m_a^y **[kg]**
Outer column top part	1	-	$1.5637 \cdot 10^5$	$1.5637 \cdot 10^5$
Outer column cone part	2	-	$1.8563 \cdot 10^5$	$1.8563 \cdot 10^5$
Outer column bot part	3	-	$2.1740 \cdot 10^5$	$2.1740 \cdot 10^5$
Outer column shirt part	4	$52.3682 \cdot 10^5$	-	-
Central column top part	5	-	$1.2645 \cdot 10^5$	$1.2645 \cdot 10^5$
Central column cone part	6	-	$1.7375 \cdot 10^5$	$1.7375 \cdot 10^5$
Central column bot part	7	$3.4787 \cdot 10^5$	-	-
Pontoons	8	-	$0.4267 \cdot 10^5$	$3.8307 \cdot 10^5$

The calculations of the added mass for the slender elements have uncertainties connected to them. Some of the assumptions and arguments behind them may be questionable. These were:

- Calculations of the added mass coefficients. Assuming an average value from frequency-dependent added mass as a constant value will not be accurate. The frequency-dependent added mass shows large value differences in the frequency interval. The frequency interval was also based on the peak periods from the D4.2 report [15] which is questionable. The volume of the floater and the simplifications of the pontoons used in the calculations could have been chosen differently. Another way to find added mass coefficients could have been to read related literature and chose added mass coefficients from a similar structure.
- Calculations of the 2D added mass. The equations used in the calculations are questionable in terms of which slender elements they were used on and in which direction.

4.2.2 Decay tests

Decay tests were performed on the RBM model in SIMA in order to obtain and document the natural periods and damping for the system. This was done in the same way as for the RBP model. Both linear and nonlinear hydrodynamic damping were still included by the SIMO-body and quadratic drag, respectively. Surge, heave, pitch and yaw were the motions that were considered for the decay tests due to symmetry of the hull. See the decay tests section 4.1.6 for the RBP model for more information regarding the decay tests.

The natural periods for the RBP model and the RBM model are compared in Table 4.16. The percentage difference between the natural periods are calculated with eq.(4.10. The natural periods in surge, heave, and pitch are more or less the same in both models. It is expected to be a small difference between the natural periods in surge and heave because of the calculations of the added mass for the slender elements. The added mass in surge and heave were estimated to be $A_{11} = 1.640 \cdot 10^7$ and $A_{33} = 3.425 \cdot 10^7$ in the RBM model, respectively. These values are different than the added mass used in the RBP model, which were $A_{11} = 1.636 \cdot 10^7$ and $A_{33} = 3.558 \cdot 10^7$. The difference in added mass is larger in heave compared to surge, and therefore it is expected to see a larger difference in heave. The natural periods in pitch are the same and it shows that the distribution of the added mass have not affected the natural period in pitch. The natural periods in yaw have some difference. The mooring system have not been changed, and it is therefore assumed that this is connected to distribution of the added mass in surge.

Table 4.16: Comparison of natural periods from the D4.2 report [15] and the RBP model.

Motion	Natural period from RBP model[s]	Natural period from RBM model[s]	Deviation
Surge	186.69	186.20	-0.12%
Heave	20.60	20.40	-0.97%
Pitch	29.27	29.24	-0.03%
Yaw	103.62	105.80	2.10%

4.2.3 Regular waves test

A regular waves test was performed on the RBM model to analyse the response of the model for different wave frequencies. This was done the same way as for the RBP model in terms of calculating the PSD and RAO. For more information regarding the regular waves test and how the PSD and RAO were calculated, see the regular waves test section 4.1.7 for the RBP model. The PSD and RAO from the regular waves test for the RBM model were compared against the RBP model. The results can be seen in Figure 4.30 - 4.35.

The RAO for surge motion for the RBM model is increasing for increasing period except for a small part between periods 6-8 s where it is slightly decreasing. The largest value is seen to be less than 1.0 for period 20 s. This is a more realistic value than the RAO value in the RBP model. The spectral density for surge motion for the RBM model varies with increasing period, but the trend is increasing spectral density. The spectral density for surge motion for the RBM model for frequencies higher than 0.17 Hz are more or less zero. The added mass in surge in the RBM model was estimated to an average value between the peak periods of the D4.2 report [15] from the frequency-dependent added mass in the RBP model. The added mass in the RBM model will therefore be above and below the added mass in the RBP model. However, the RAOs and the spectral densities for surge motion are larger for the RBP model compared the RBM model for all periods. The difference between the models starts from period 6 s and seems to increase with increasing period. This indicates that the hydrodynamic loads in surge are larger on the RBP model compared to the RBM model.

The RAO for heave motion for the RBM model shows a large value for 20 s period. This is as expected since the natural period in heave is close to this period. This value is less than half of the RAO value for heave motion for the RBP model. Also, the RAO for heave motion for the RBM model has a trough around period 17-18 s. This is closer to the calculated cancellation period 18.48 s. There is a peak in the RAO for heave motion for the RBM model at period 13 s. The RAO for heave motion goes towards zero as the period goes towards 4 s. The same trends mentioned for the RAO are seen in the PSD for heave motion for the RBM model. The spectral density for heave motion for the RBM model for frequencies

higher than 0.15 Hz are more or less zero. The added mass in heave in the RBM model was estimated to an average value between the peak periods of the D4.2 report [15] from the frequency-dependent added mass in the RBP model. The added mass in the RBM model will therefore be above and below the added mass in the RBP model. By comparing the RAO for heave motion for the RBM model with the RBP model it is seen that they are more or less the same for periods up to 7 s. For periods between 7-11 s are the RAO for the RBP model larger than the RAO in the RBM model. For periods between 12-15 s are the RAO for the RBP smaller than the RAO in the RBM model. For periods larger than 16 s are the RAO for the RBP larger than the RAO in the RBM model. The peak periods in the RAOs for heave are different in the models, but similar in value. This is also the case for the troughs. The same trends mentioned for the comparison of the RAOs for heave motion for the hydrodynamic models are seen in the PSDs for heave motion for the hydrodynamic models. This indicates that the hydrodynamic loads in heave may be larger on the RBP model for some periods and for other periods are the hydrodynamic loads in heave larger for the RBM model.

The RAO for pitch motion for the RBM model has no large value for a specific period compared to the other periods. It has a peak at period 10 s and a trough at period 18 s. The RAO value for pitch motion for the RBM model is increasing for increasing period until it reaches the peak period. Then a decrease in the RAO values is seen for increasing period until it reaches the trough period. After that is an increase in the RAO value for increasing period seen again. The RAO value for pitch motion for the RBM model goes towards zero as the period goes towards 4 s. Also, the RAO values for periods 9 s and 10 s are more or less the same, but a significant difference can be seen in the PSD for pitch motion for the RBM model for these periods. This may be an indication of the effect of the problem related the PSD for wave elevation presented in section 4.1.7. Other than that are the same trends as mentioned for the RAO seen in the PSD for pitch motion for the RBM model. The spectral density for pitch motion for the RBM model for frequencies higher than 0.15 Hz are more or less zero. By comparing the RAO for pitch motion for the RBM model with the RBP model it is seen that they are more or less the same for periods up to 7 s. For periods roughly between 8-10 s are the RAO for the RBP model larger than the RAO in the RBM model. For periods between 10-14 s are the RAO for the RBP smaller than the RAO in the RBM model. For periods larger than 15 s are the RAO for the RBP larger than the RAO in the RBM model. The difference in the RAO values between the models is rapidly increasing after period 15 s. The peak periods in the RAOs for pitch motion are different in the models, but similar in value. This is also the case for the troughs. The same trends mentioned for the comparison of the RAOs for pitch motion for the hydrodynamic models are seen in the PSDs for pitch motion for the hydrodynamic models. This indicates that the hydrodynamic loads in pitch may be larger on the RBP model for some periods and for other periods are the hydrodynamic loads in pitch larger for the RBM model. For periods above 15 s are the difference in hydrodynamic loads believed to be larger than for smaller periods.

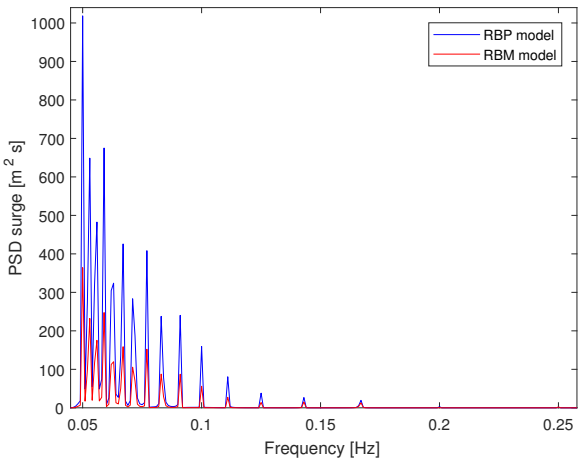

(a) PSD

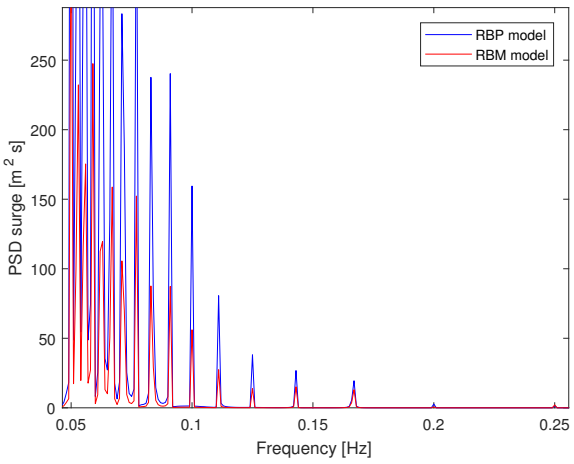

(b) PSD zoom in

Figure 4.30: Comparison of the PSD for surge motion for the RBM model and the RBP model from the regular waves test.

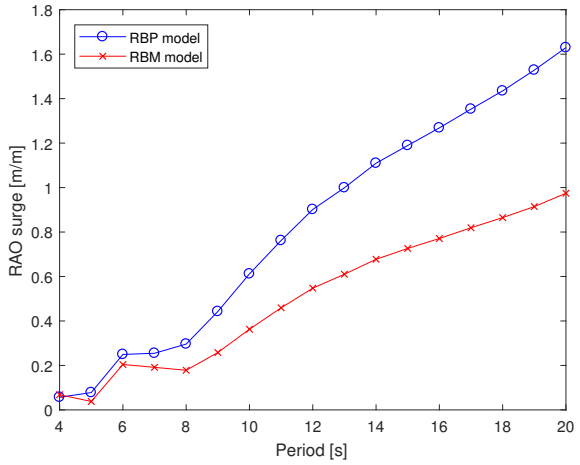

(a) RAO

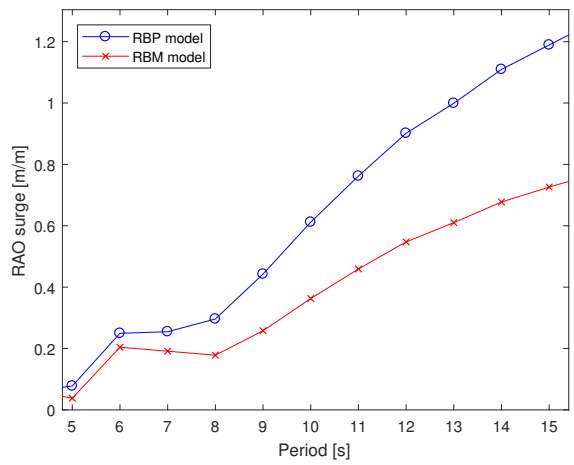

(b) RAO zoom in

Figure 4.31: Comparison of the RAO for surge motion for the RBM model and the RBP model from the regular waves test.

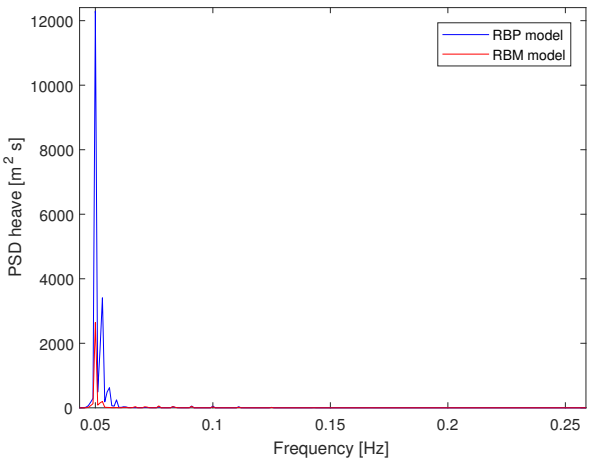

(a) PSD

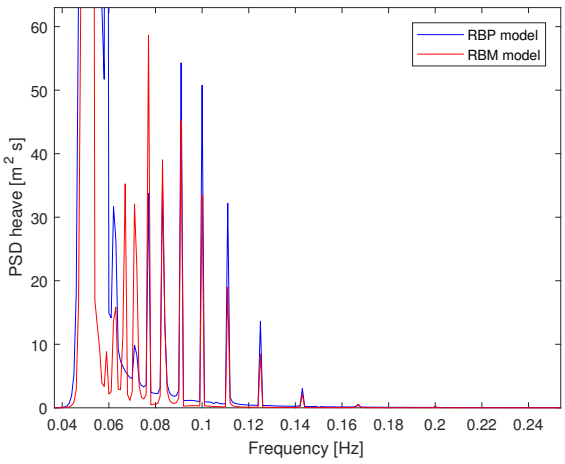

(b) PSD zoom in

Figure 4.32: Comparison of the PSD for heave motion for the RBM model and the RBP model from the regular waves test.

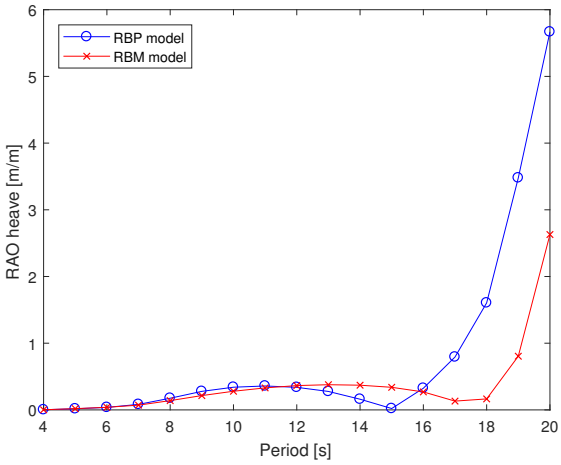

(a) RAO

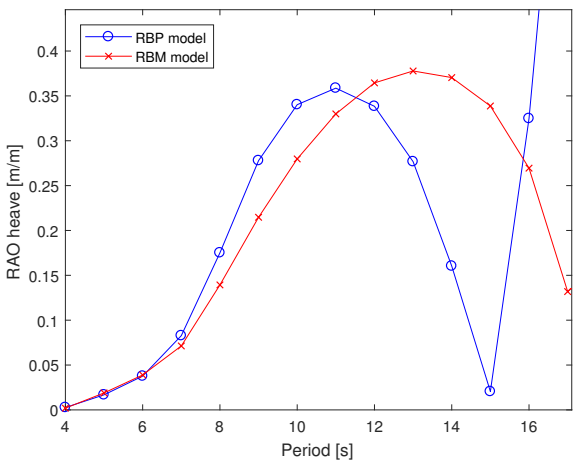

(b) RAO zoom in

Figure 4.33: Comparison of the RAO for heave motion for the RBM model and the RBP model from the regular waves test.

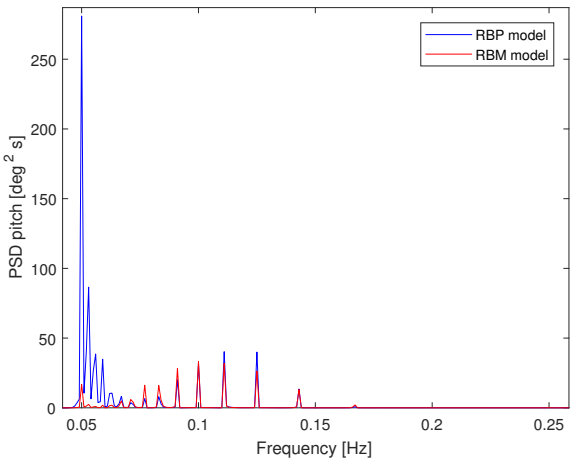

(a) PSD

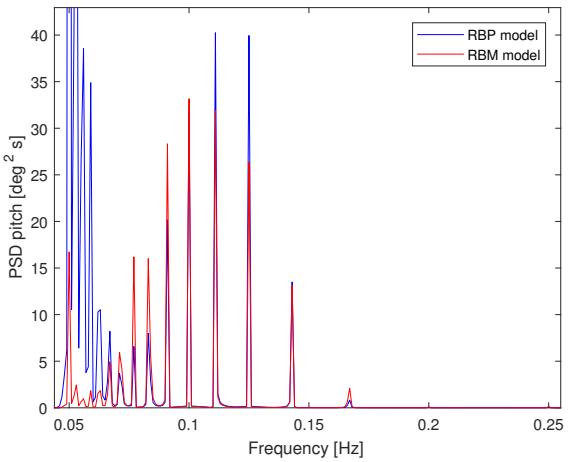

(b) PSD zoom in

Figure 4.34: Comparison of the PSD for pitch motion for the RBM model and the RBP model from the regular waves test.

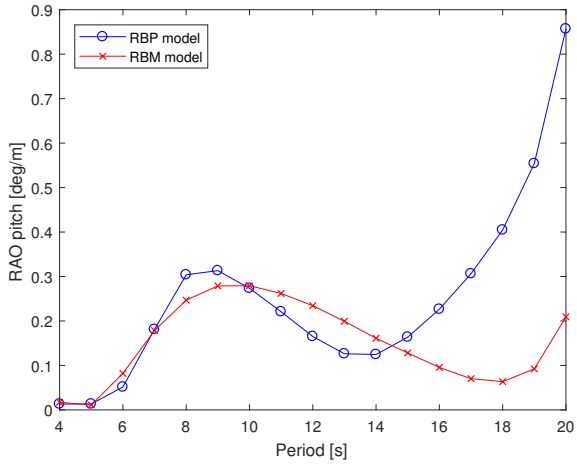

(a) RAO

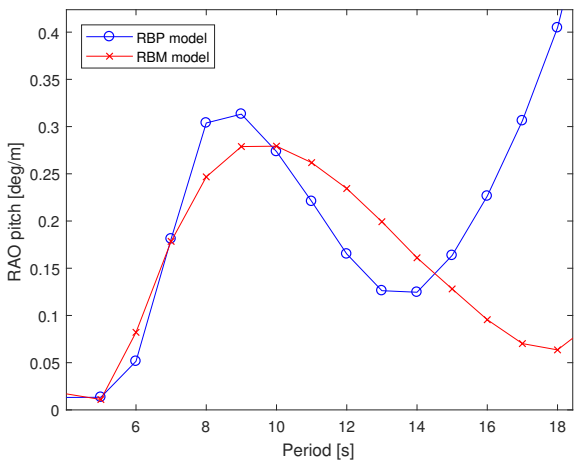

(b) RAO zoom in

Figure 4.35: Comparison of the RAO for pitch motion for the RBM model and the RBP model from the regular waves test.

4.3 Flexible beam model using Morison's equation

The third hydrodynamic model to be made was the flexible beam model using Morison's equation, referred to as flexible body Morison (FBM) model. The FBM model was developed from the SIMO-RIFLEX model of the rigid body Morison (RBM) model in SIMA. The hydrodynamic loads were still calculated by Morison's equation, but the slender elements were changed to flexible RIFLEX beam elements. Everything in the SIMO-body representing the hull was removed except the linear damping. The beam elements were inserted with structural properties from the D4.2 report [15]. The displaced water volume, mass, center of buoyancy, and center of mass were different for the FBM model compared to the RBM model. Extra volume were added to the pontoons to have the same buoyancy and masses were moved to have the same center of mass. The added mass and quadratic drag for the slender elements in the RBM model were kept the same in the RIFLEX beam elements for the FBM model. Figure 4.47 shows the FBM model in SIMA.

Decay tests and a regular waves test were performed on the FBM model to analyse the motion responses of the model. The results from the tests were compared against the results from the RBM model. The following sections will give more details on how each of the steps in the modeling procedure were done to create the FBM model and the reasoning behind it. The results from the tests with discussion will also be presented.

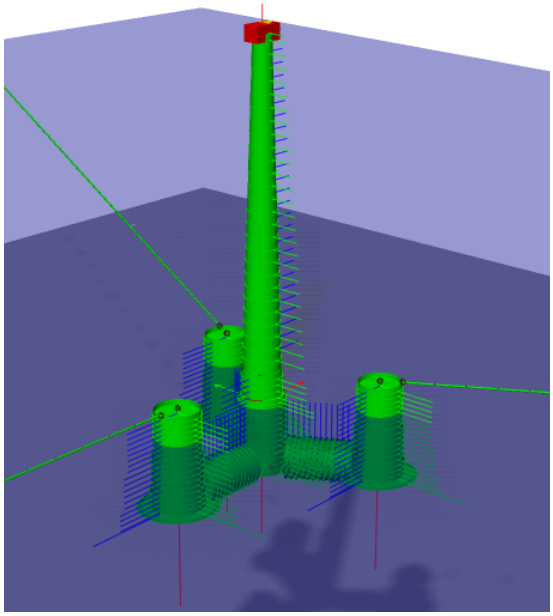

Figure 4.36: The flexible body using Morison's equation (FBM) model in SIMA.

4.3.1 Structural properties

The structural properties for the different parts of the floater of the OO-Star Wind Floater Semi 10MW were taken from the D4.2 report [15]. The background for these numbers were not specified in report. A MATLAB script was developed to calculate the mass, buoyancy, center of gravity and center of buoyancy when these values were used in the beam elements representing the hull in the FBM model. The calculated values were compared with the values used in the RBM model, which were taken from the D4.2 report.

First step was to calculate the buoyancy of the FBM model. The difference was 1006.9 m^3 less displaced water volume compared to the RBM model, which is less than 4.3%. The missing displaced water volume was evenly added to the three pontoons and increased the cross section area of the pontoons from 112 m^3 to 128 m^3. Next step was to calculate the center of buoyancy in vertical direction. This was calculated to be -14.141 m in the FBM model compared to -14.236 m in the RBM model. This difference was assumed to be small enough to not needing to redistribute the displaced water volume. The reason for not calculating the center of buoyancy in the other directions was due to symmetry of the hull. The next step was to calculate the mass of the FBM model. The difference compared to the RBM model was 106963 kg additional mass, which is less than 0.5%. The mass difference was taken from the cone parts of the outer columns and the center column. Center of mass for the FBM model was next to be calculated. This was -14.071 m in the FBM model compared to -15.225 m in the RBM model. The majority of this difference is assumed to be connected to the simplification of the pontoons and the cone parts of the columns. These structural parts have lower center of mass than in the FBM model. This was seen as to large of a difference to neglect and therefore redistribution of masses were needed. This was done by moving masses from the top and cone parts of the outer and inner columns to the pontoons. The masses were removed equally as much from the different parts and ended up being approximately 26% reduction of mass for each part. This gave the center of gravity to be -15.225 m in the FBM model, which was exactly the same as in the RBM model. To sum things up, the mass, buoyancy and center of mass were exactly the same in both models, and the center of buoyancy was slightly closer to the free surface in the FBM model compared to the RBM model.

Table 4.17 shows the final input values for structural properties for the beam elements after the calculations and redistribution. It was assumed that other structural properties, such as axial stiffness EA, did not change by the adding or removing of volume or mass. The structural properties of the outer column shirt part were not given in the D4.2 report [15]. These values were taken to be the same as the values for the outer column bottom part or estimated from them. The reason for this was that all beam elements needed structural properties values for SIMA to work.

Table 4.17: OO-Star Wind Floater Semi 10MW distributed structural properties. Taken from the D4.2 report [15].

Structural part	**Radius**	**Mass density**	**Element length**	**EA**	**EI$_y$**	**EI$_z$**	**GJ**
Unit	[m]	[kg/m]	[m]	[N]	[N m^2]	[N m^2]	[N m^2]
Pontoon	-	$20.10 \cdot 10^4$	21.000	$6.39 \cdot 10^{11}$	$5.53 \cdot 10^{12}$	$19.70 \cdot 10^{12}$	$10.50 \cdot 10^{12}$
Central column top part	6.025	$4.27 \cdot 10^4$	8.225	$5.96 \cdot 10^{11}$	$9.88 \cdot 10^{12}$	$9.88 \cdot 10^{12}$	$8.23 \cdot 10^{12}$
Central column cone part	-	$6.32 \cdot 10^4$	17.775	$7.39 \cdot 10^{11}$	$18.40 \cdot 10^{12}$	$18.40 \cdot 10^{12}$	$15.30 \cdot 10^{12}$
Central column bot part	8.100	$11.70 \cdot 10^4$	7.000	$8.82 \cdot 10^{11}$	$26.90 \cdot 10^{12}$	$26.90 \cdot 10^{12}$	$22.40 \cdot 10^{12}$
Outer column top part	6.700	$3.37 \cdot 10^4$	13.500	$4.90 \cdot 10^{11}$	$10.40 \cdot 10^{12}$	$10.40 \cdot 10^{12}$	$8.64 \cdot 10^{12}$
Outer column cone part	-	$6.72 \cdot 10^4$	11.500	$5.36 \cdot 10^{11}$	$16.20 \cdot 10^{12}$	$16.20 \cdot 10^{12}$	$13.50 \cdot 10^{12}$
Outer column bot part	7.900	$14.00 \cdot 10^4$	8.225	$5.81 \cdot 10^{11}$	$22.00 \cdot 10^{12}$	$22.00 \cdot 10^{12}$	$18.30 \cdot 10^{12}$
Outer column shirt part	11.400	$29.15 \cdot 10^4$	0.5	$5.81 \cdot 10^{11}$	$22.00 \cdot 10^{12}$	$22.00 \cdot 10^{12}$	$18.30 \cdot 10^{12}$

More structural properties than the listed values in the D4.2 report [15] were needed for the beam elements in the FBM model. These were calculated on the basis of the values given in the D4.2 report [15] and three assumptions which were:

- Concrete was used as a material for the hull with a density 2400 kg/m^3.
- The mass was evenly distributed.
- The cylinders were hollow.

The structural properties that were calculated are listed in Table 4.18. The adding or removing of volume or mass were accounted for in these values. The added mass and quadratic drag from the slender elements in the RBM model were kept the same in the beam elements for the FBM model. Radius of gyration R_g were calculated with eq.(4.20), where A is the cross section area and I is the second moment

of area.

$$R_g = \sqrt{\frac{I}{A}} \tag{4.20}$$

Table 4.18: OO-Star Wind Floater Semi 10MW calculated distributed structural properties.

Structural part	**Outer area**	**Area**	**Inner area**	**Second moment of area**	**Radius of gyration**
Unit	[m^2]	[m^2]	[m^2]	[m^4]	[m]
Pontoon	127.98	83.75	44.23	457.33	2.337
Central column top part	114.04	17.80	96.25	297.80	4.091
Central column cone part	156.70	26.32	130.38	601.30	4.780
Central column bot part	206.12	48.75	157.37	1410.12	5.378
Outer column top part	141.03	14.06	126.97	299.80	4.618
Outer column cone part	167.42	28.02	139.40	684.12	4.941
Outer column bot part	196.07	58.33	137.73	1549.51	5.154
Outer column shirt part	408.28	121.47	286.81	6719.00	7.437

4.3.2 Decay tests

Decay tests were performed on the FBM model in SIMA in order to obtain and document the natural periods and damping for the system. This was done in the same way as for the RBP model. Both linear and nonlinear hydrodynamic damping were still included by SIMO-body and quadratic drag, respectively. Surge, heave, pitch and yaw were the motions that were considered for the decay tests due to symmetry of the hull. See the decay tests section 4.1.6 for the RBP model for more information regarding the decay tests.

The natural periods for the FBM model and the RBM model are compared in Table 4.19. The percentage difference between the natural periods are calculated with eq.(4.10. The natural periods in surge are seen to be more or less the same. The difference between the natural periods in heave are -2.60% and can be explained by difference in the water plane area in the two models. The RBM model have exact water plane area because it was calculated in MATLAB and the exact water plane area of the cone part of the center column were used in the calculations. In the FBM model, the cone parts of the outer and center columns were simplified to a constant diameter which were calculated as the average diameter between the top and bottom part of the cone parts. This made a difference in the water plane area for the center column. The water plane areas in the RBM model and the FBM model are 550 m^2 and 580 m^2, respectively. Inserting these values into the hand calculations of the natural period in heave gives the period in the FBM model to be 0.535 s less than the RBM model. This is approximately -2.60% difference previously stated.

The largest difference is found between the natural periods in pitch with 7.32%. As mentioned before, there is a difference between the center of buoyancy in the FBM model and the RBM model. This results in a 9.6% difference in the mass-buoyancy contribution in the hydrostatic restoring stiffness. However, this difference have small effect on the hydrostatic restoring stiffness since the second moment of area is ten times larger then the mass-buoyancy contribution. It is assumed that the difference between the natural periods in pitch are connected to mass, inertia or flexibility of the pontoons and columns. Inertia seems to be the most likely one due to the redistribution of masses in the FBM model. The beam elements representing the substructure are simplifications of the actual substructure and leads to limitations in the distribution of masses. The D4.2 report states that "*the flexibility of the pontoons and columns have an important influence on the system natural frequencies*". The flexibility in the beam elements may influence the natural period in pitch. A lot of structural properties were inserted into the FBM model. Misinterpretation or human error could be the reason for the difference. The difference was not further investigated. There is also a difference in the natural periods in yaw. The mooring system have not been changed, and it is therefore assumed that this is connected to the same reasons as stated above in terms of inertia or flexibility.

Table 4.19: Comparison of natural periods from the D4.2 report [15] and the RBP model.

Motion	**Natural period from RBM model[s]**	**Natural period from FBM model[s]**	**Deviation**
Surge	186.20	186.89	0.37%
Heave	20.40	19.87	-2.60%
Pitch	29.24	31.38	7.32%
Yaw	105.80	102.80	-2.84%

4.3.3 Regular waves test

A regular waves test was performed on the FBM model to analyse the response of the model for different wave frequencies. This was done the same way as for the RBP model in terms of calculating the PSD and RAO. For more information regarding the regular waves test and how the PSD and RAO were calculated, see the regular waves test section 4.1.7 for the RBP model. The PSD and RAO from the regular waves test for the FBM model were compared against the RBM model. The results for the surge, heave and pitch motion can be seen in Figure 4.37-4.42.

The RAO and the PSD for surge motion for the FBM model is more or less exactly the same as the RBM model. The FBM model have slightly larger values than the RBM model for periods above 10 s, but this difference is assumed to be negligible. This indicates that the surge motion are the same on the FBM model compared to the RBM model.

The RAO and PSD for heave motion for the FBM model is seen to be similar to the RBM model. The FBM model have higher values than the RBM model for periods above 10 s. The difference in values between the models seems to be relatively the same for the periods between 12-17 s, and increasing for longer periods. The water plane area is larger in the FBM model compared to the RBM model. This will give more stiffness in the heave motion. However, the values are larger in the FBM model and this could indicate that the elastic hull have an effect on the motion in heave compared to the rigid hull. This indicates that the motion of the FBM model will be equal or larger than the motion of the RBM model.

The RAO and PSD for pitch motion for the FBM model is seen to be similar to the RBM model. The FBM model have smaller values than the RBM model for periods equal or above 6 s. The difference in values between the models seems increase for increasing period until it reaches the peak period at 10 s. From there, the difference starts to decreases until it reaches the period 17 s, which is the period before the trough period at 18 s. The difference starts to increase again after this period. The natural period in pitch was smaller for the RBM model compared to the FBM model. The reason for this is still uncertain. This indicates that there is a difference related to the inertia in the models. This may be the reason for the difference in pitch motion.

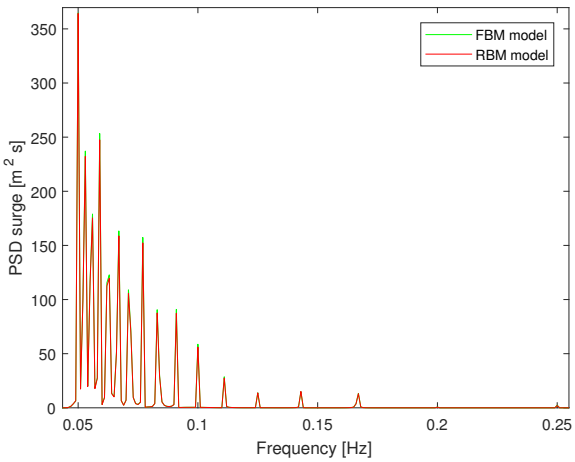

(a) PSD

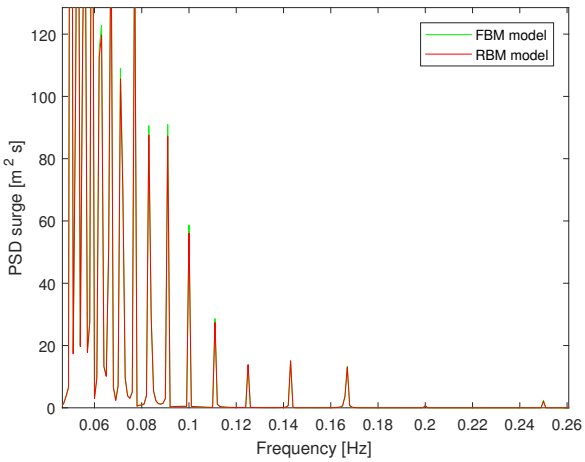

(b) PSD zoom in

Figure 4.37: Comparison of the PSD for surge motion for the FBM model and the RBM model from the regular waves test.

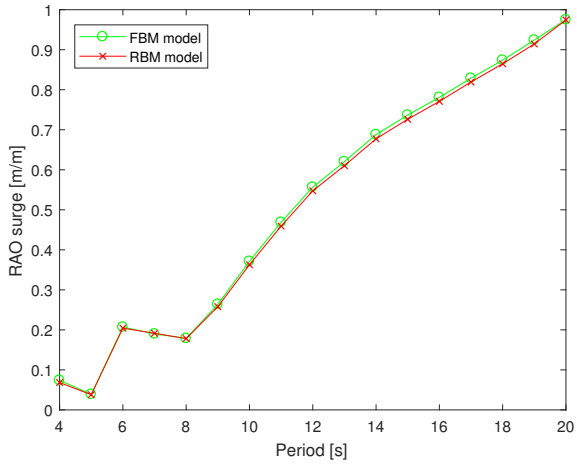

(a) RAO

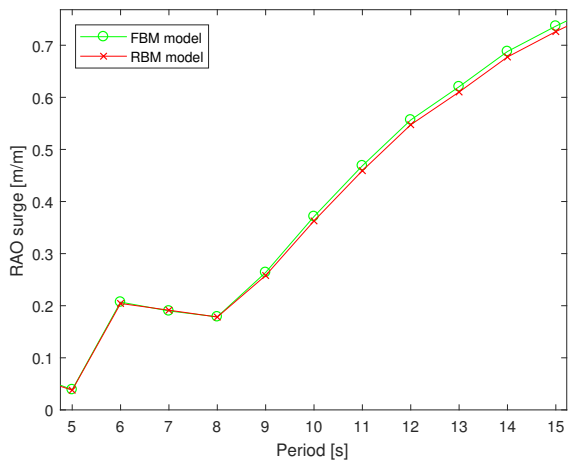

(b) RAO zoom in

Figure 4.38: Comparison of the RAO for surge motion for the FBM model and the RBM model from the regular waves test.

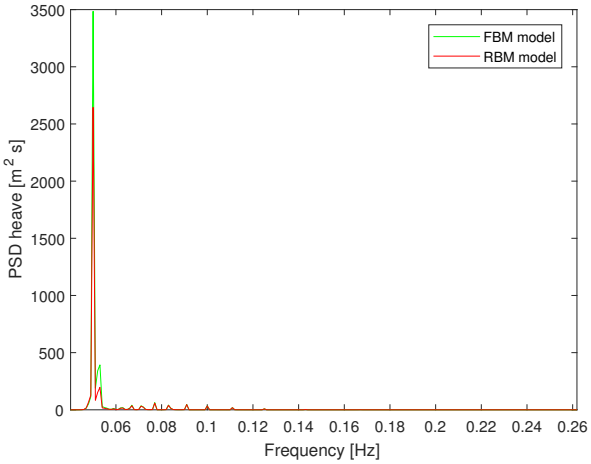

(a) PSD

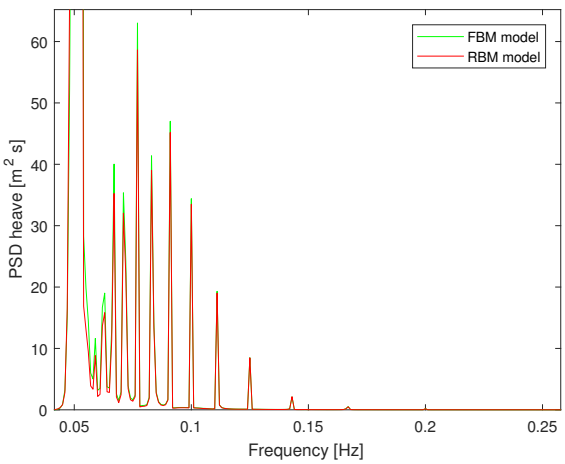

(b) PSD zoom in

Figure 4.39: Comparison of the PSD for heave motion for the FBM model and the RBM model from the regular waves test.

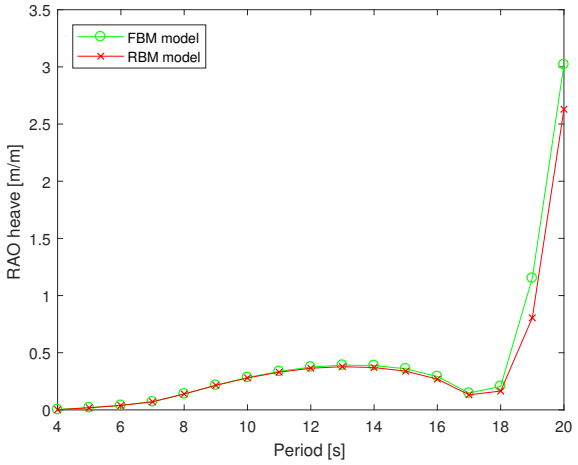

(a) RAO

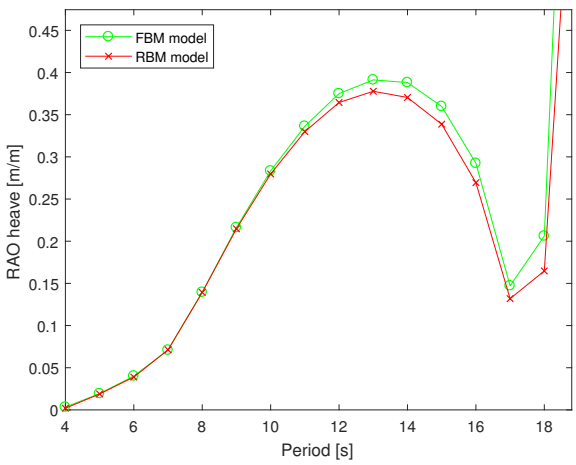

(b) RAO zoom in

Figure 4.40: Comparison of the RAO for heave motion for the FBM model and the RBM model from the regular waves test.

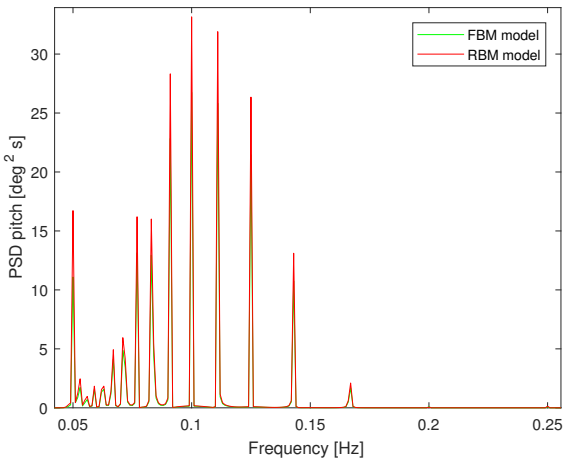

(a) PSD

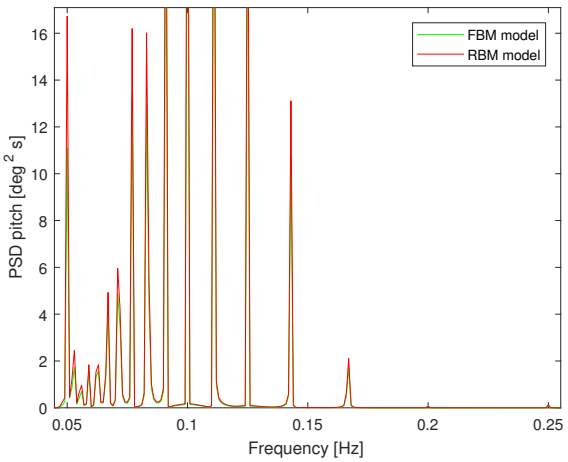

(b) PSD zoom in

Figure 4.41: Comparison of the PSD for pitch motion for the FBM model and the RBM model from the regular waves test.

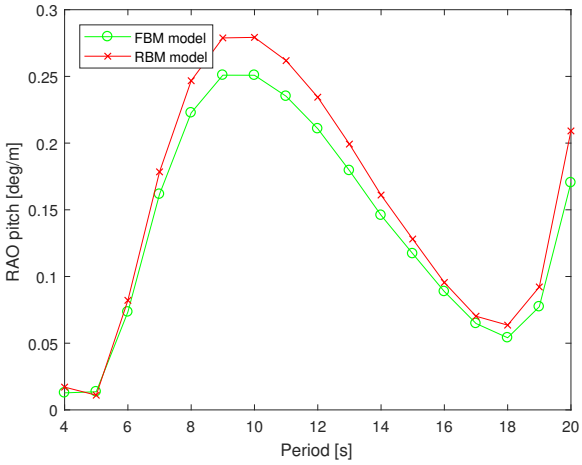

(a) RAO

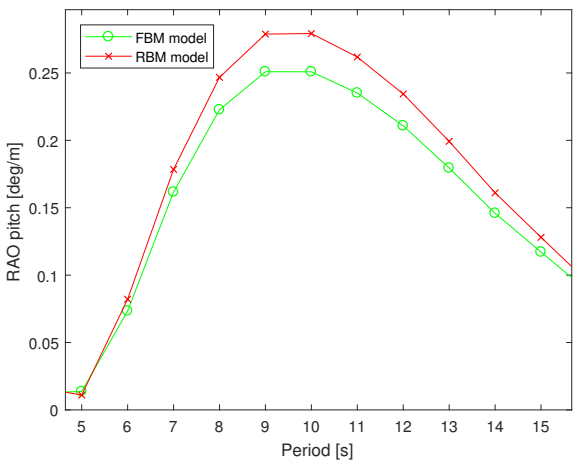

(b) RAO zoom in

Figure 4.42: Comparison of the RAO for pitch motion for the FBM model and the RBM model from the regular waves test.

4.4 Flexible beam model using distributed loads from first order potential theory

The fourth hydrodynamic model that was supposed to be made was the flexible beam model using distributed loads from first order potential theory. This model is referred to as flexible body potential (FBP) model. The FBP model was never finished due to software problems and limited time. The FBP model was supposed to be developed from a combination of the RBP model and the FBM model. The new method to implement radiation and diffraction pressures from first order potential theory as hydrodynamic load input for sections of the hull in SIMO-bodies was gonna be used.

The starting point was the 3D geometry model of the hull developed in GeniE for the RBP model. This model was divided into sections and imported to HydroD to generate the 3D panel model. Wadam was used as hydrodynamic solver to get the radiation and diffraction pressures on each panel separately. A MATLAB script, which was given by the supervisor, was attempted to further developed to transform the the radiation and diffraction pressures on the panels into frequency-dependent added mass, damping and excitation forces for sections of the hull. This was not finished and became the end of the work done in this thesis. The following sections will explain the software problems with the FBP model and where the work was ended.

4.4.1 GeniE mesh problems

The software problems started with the mesh of the 3D geometry model of the hull in GeniE. The first attempt was to make a geometry model with many feature edges. Feature edges are lines that elements cannot cross. This was done to have the opportunity to have many sections and to do a convergence test to see if the number of sections was an important factor for the new method. The geometry model was coded in a java script. The mesh turned out to be very bad for this model in terms of holes in the mesh, small elements close to large elements, and strange element patterns. The number of elements was close to 50000 and this is too many elements to run simulations in HydroD. Multiple persons were asked about the problems, varying from people at NTNU marine technology to DNV GL, without success. It seemed to be the shirt along the pontoons which made a lot of the problems with mesh. Figure 4.43 and 4.44 shows the mesh for this geometry model of the hull.

The next attempt was to make geometry model with less feature edges than before. The geometry model with many feature edges was used as a starting point. A lot of feature edges were removed until approximately a quarter of the originally feature edges remained. This geometry model was also coded in a java script. Unfortunately, the mesh in this model turned out bad as well. There were no holes in the mesh, but small elements close to large elements and strange patterns were still there. The number of elements was also way to high to run simulations in HydroD.

A third attempt was done. The starting point for this attempt was the geometry model developed for the RBP model. All of the modelling was done in the graphical user interface (GUI) in GeniE. The number of feature edges was kept low as the previous model. The mesh of this model turned out ok. There were still parts of the mesh that was not great, but the mesh was good enough for HydroD to run simulations. Figure 4.45 and 4.46 shows the mesh for this geometry model of the hull.

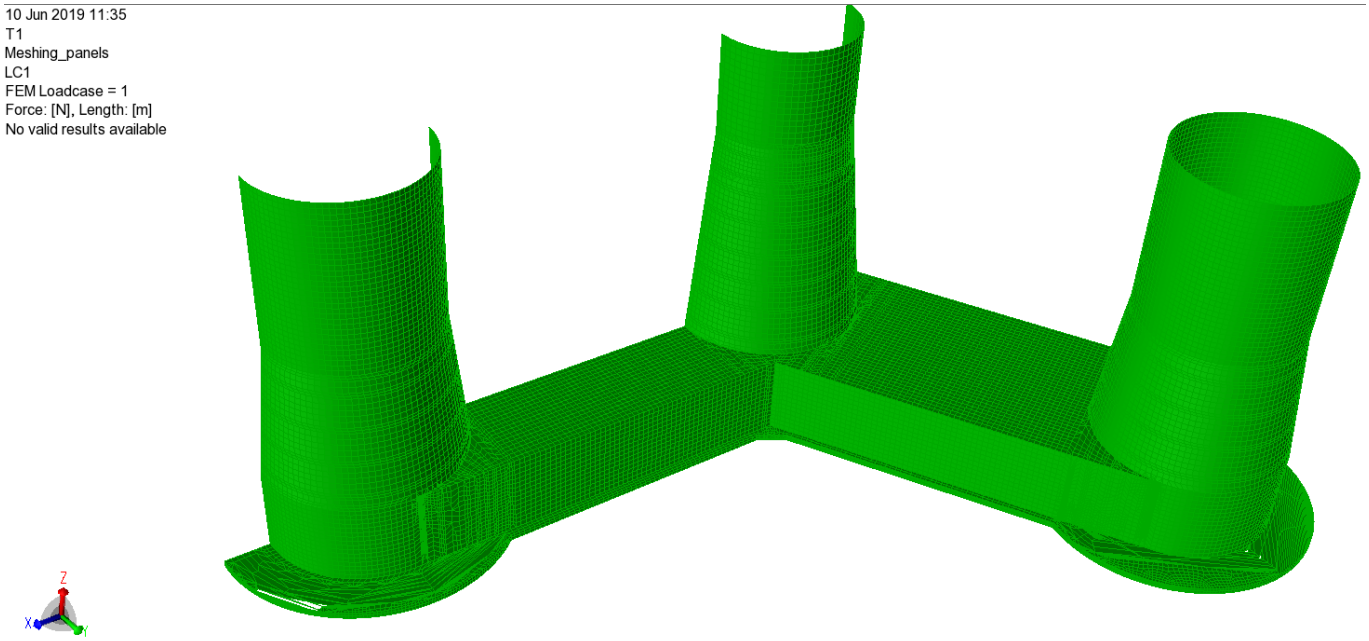

Figure 4.43: Mesh in GeniE of the geometry model of the hull with a lot of feature edges.

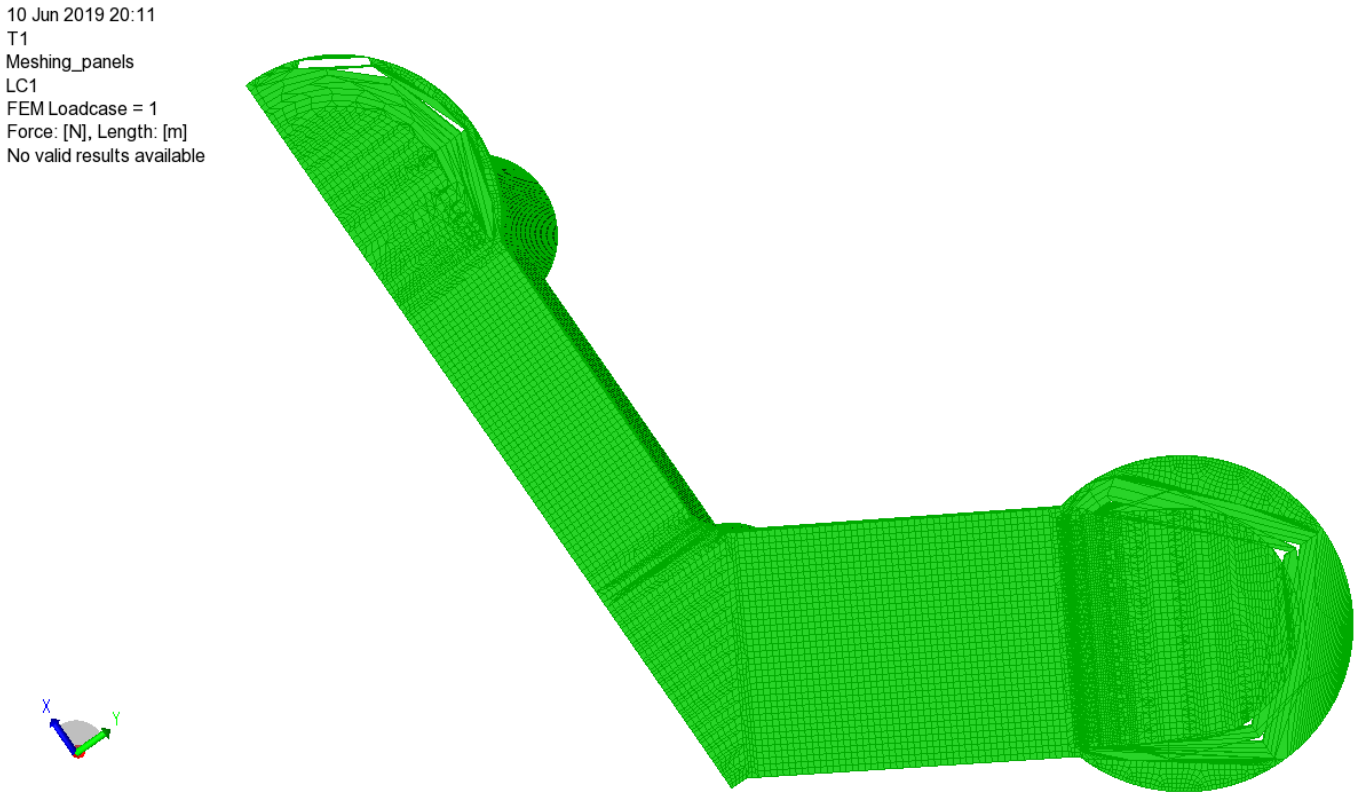

Figure 4.44: Mesh in GeniE of the geometry model of the hull with a lot of feature edges.

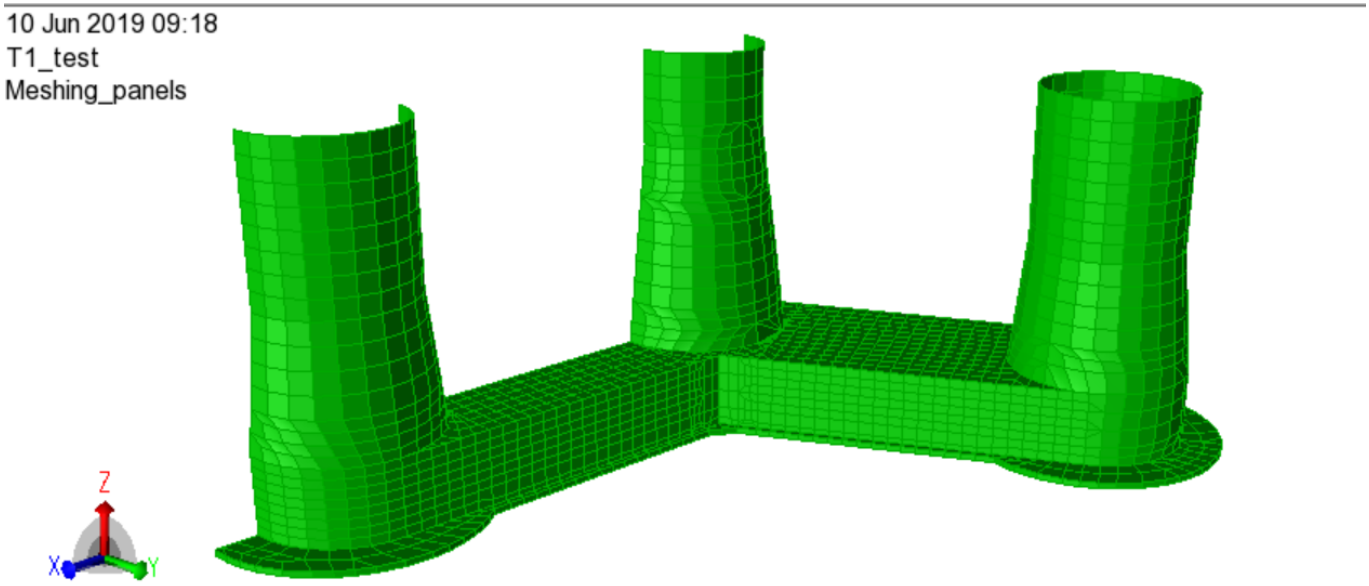

Figure 4.45: Mesh in GeniE of the geometry model of the hull with few feature edges.

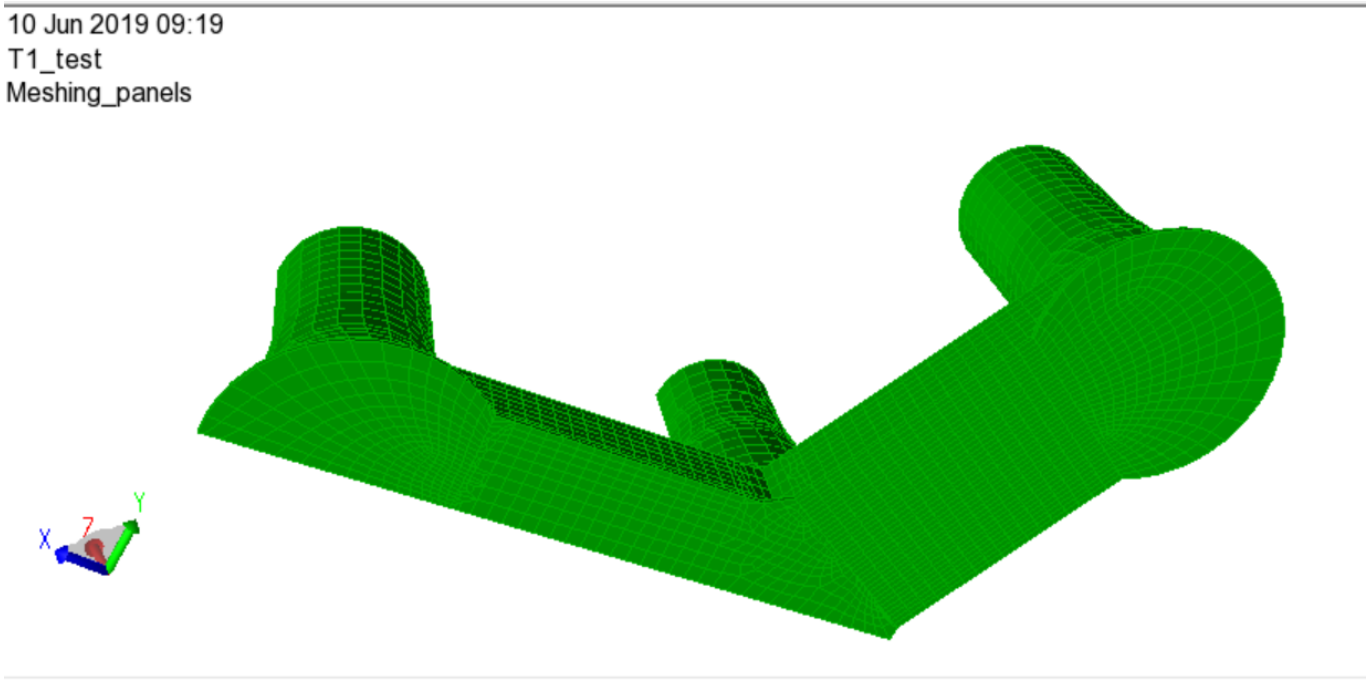

Figure 4.46: Mesh in GeniE of the geometry model of the hull with few feature edges.

4.4.2 MATLAB script problems

A MATLAB script was provided from the supervisor. The script was developed for a TLPWT with three pontoons and a center column, and did the following:

- Divide the hull structure into sections.
- Associate each panel in the 3-D panel model with one of the sections.
- Compute the added mass, radiation and excitation coefficients for each section.
- Determine the hydrodynamic loads' point of application within each section.

The script was developed on the basis that WAMIT was used as the hydrodynamic solver and the results were WAMIT result files. The script was used as a starting point. Wadam was used as hydrodynamic solver in this thesis. Wadam gives the radiation and diffraction pressure for each panel together in one file while WAMIT gives them separately. A separate script was developed to transform the results from Wadam into the same manner as WAMIT results. The provided script needed to be further developed for all the parts mentioned above to work for the SSWT. The script was able to run in the end and results for the added mass and damping for different sections were plotted. Here it was seen that something was wrong with the calculations in the script. The sum of the added mass in surge and heave from all of the sections did not match the added mass for the whole structure calculated for the RBP model. The damping was also negative for some sections. A solution to this problem was not found due to limited

time. It is believed that the mistake in calculations was connected to the integration of pressure on the panels and the values for the non-dimensional parameters from WAMIT.

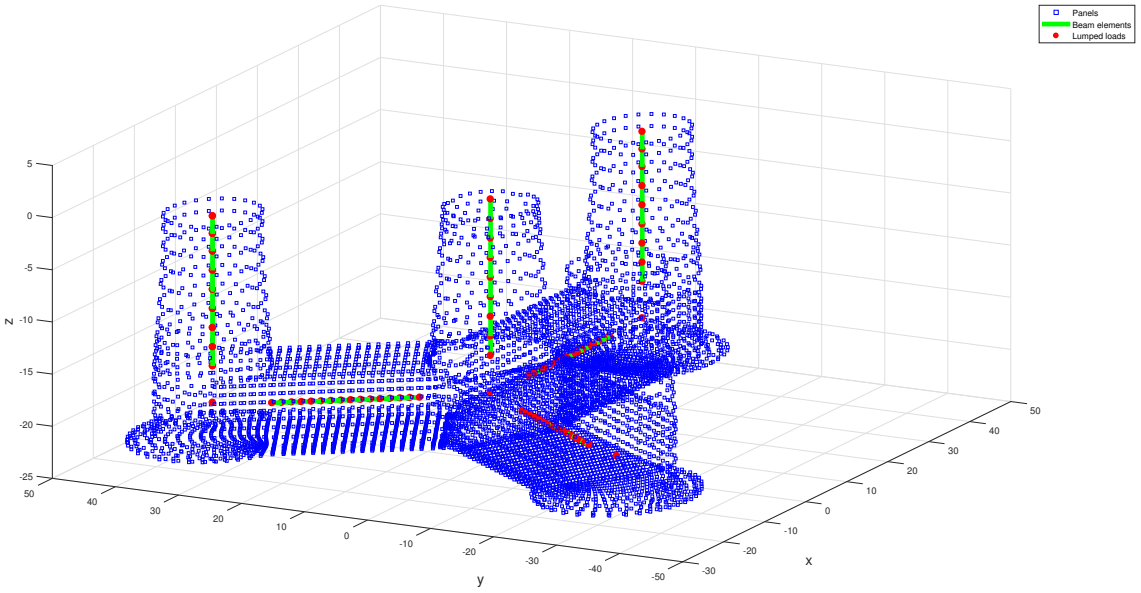

Figure 4.47: MATLAB visualization of panels (blue), nodes (red), and sections (green).

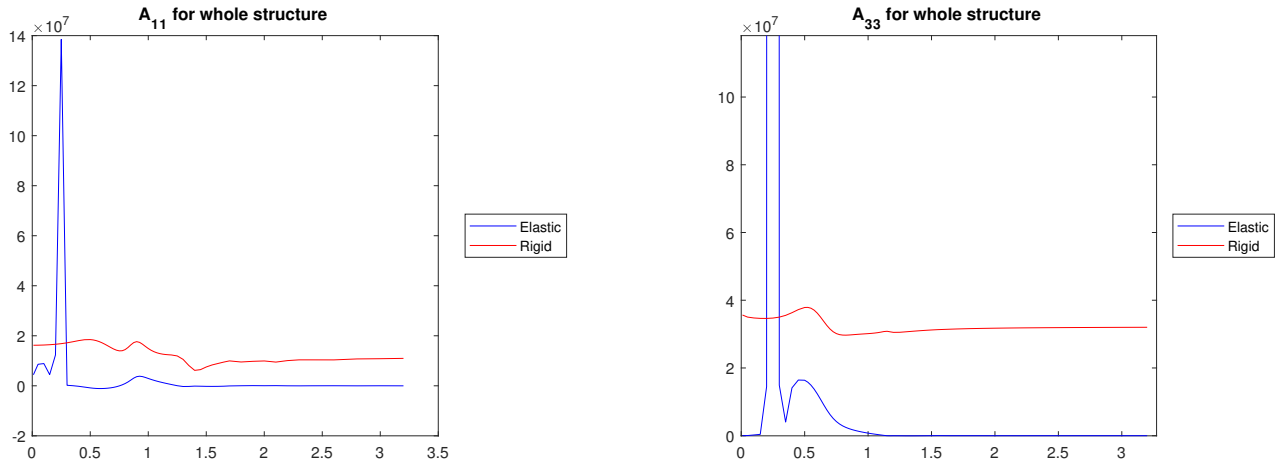

(a) A11 for hull

(b) A33 for hull

Figure 4.48: Comparison of A11 and A33 for the hull as a whole (rigid) and the sum of all sections (elastic). The horizontal axis are frequencies and the vertical axis is magnitude.

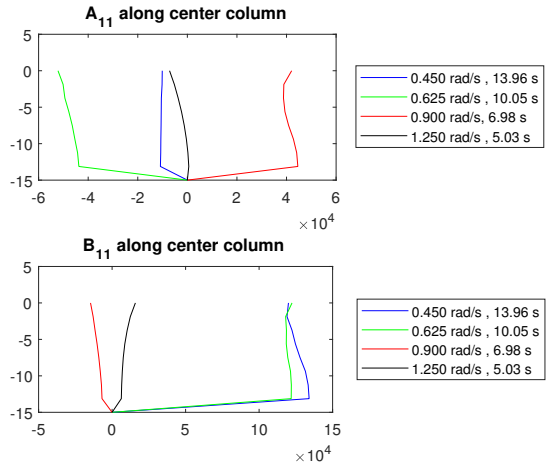

(a) A11 and B11 center column

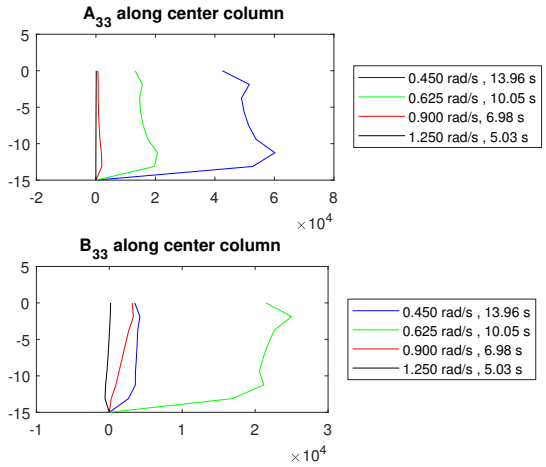

(b) A33 and B33 center column

Figure 4.49: A11, B11, A33 and B33 for different sections of the center column for different frequencies. The vertical axis is the height at center column and the horizontal axis is magnitude.

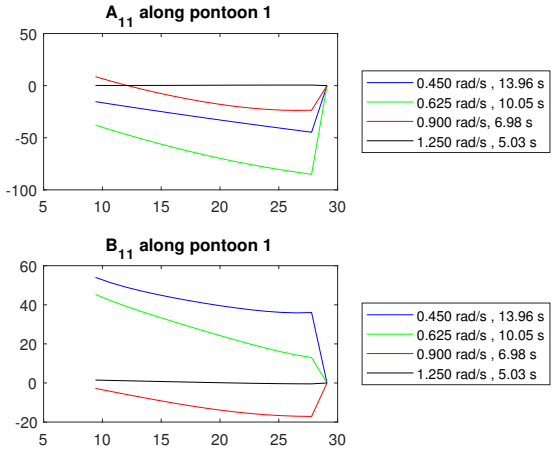

(a) A11 and B11 front pontoon

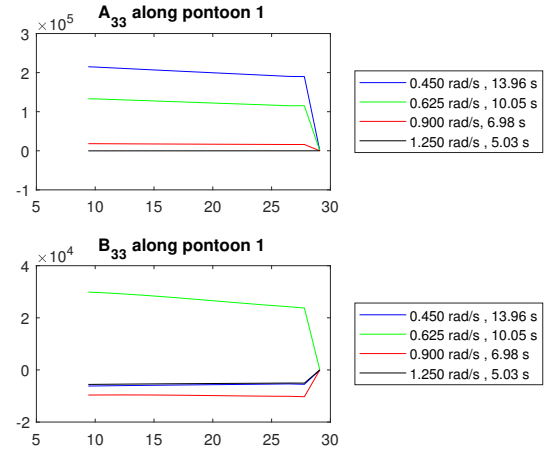

(b) A33 and B33 front pontoon

Figure 4.50: A11, B11, A33 and B33 for different sections of the front pontoon for different frequencies. The horizontal axis is the length along the pontoon and the vertical axis is magnitude.

5 Conclusion and recommendations for future work

5.1 Conclusion

Four different hydrodynamic models were supposed to be made and evaluated in this study. The first one to be made was a rigid body model using first order potential theory, referred to as the RBP model. The starting point was the sketches of the OO-Star Wind Floater Semi 10 MW in the D4.2 report [15]. A 3D geometry model of the hull was generated in GeniE. This model was taken into HydroD to generate a 3D panel model of the hull. Added mass and radiation damping coefficients together with first-order wave excitation for the different motions were then calculated for the hull as a whole using Wadam in HydroD. The results were compared against previous results in the D4.2 report to verify the results. The results were seen to be the same. The sensitivity of the results to the mesh in the first order potential flow solver was also checked and seen to be approximately the same for the chosen mesh sizes. A SIMO-RIFLEX model of the total structure (tower, floating substructure and mooring system) was then created in SIMA. Viscous effects were included in the model with quadratic drag from Morison's equation. Analyses in terms of decay tests and a regular waves test were performed on the RBP model. The results from the decay tests were compared against previous results in the D4.2 report to verify the results. The natural periods in surge and yaw were seen to be 2.68% and -10.89% in difference, respectively. This was assumed to be connected the mooring system. The natural period in heave was approximately the same. The natural period in pitch was -6.34% in difference, and the reason for this was not found. The regular waves test showed large values for the RAOs. This was assumed to be connected to lack of damping in the system.

The second model to be made was the rigid body model using Morison's equation, referred to as the RBM model. The added mass in vertical and horizontal direction were estimated from the frequency-dependent added mass from the RBP model. The quadratic drag was kept the same as in the RBP model. Analyses in terms of decay tests and a regular waves test were performed on the RBM model and compared with the RBP model. The natural periods were more or less the same. The natural period in yaw was 2.10% in difference, and assumed to be connected to the horizontal added mass. The regular waves test showed larger surge motion for the RBP model, while the heave and pitch motion varied depending on the wave period.

The third model to be made was the flexible beam model using Morison's equation, referred to as the FBM model. The structural properties for the beam elements representing the hull was taken from the D4.2 report [15]. The displaced water volume, mass, center of buoyancy, and center of mass were different for the FBM model compared to the RBM model. Extra volume were added to the pontoons to have the same buoyancy and masses were moved to have the same center of mass. However, a difference in the center of buoyancy was not changed in the FBM model. The added mass and quadratic drag in the

RBM model were kept the same in the FBM model. Analyses in terms of decay tests and a regular waves test were performed on the model and compared with the RBM model. The natural period in surge was the same. The natural period in heave was -2.60% in difference, and the reason for this was different water plane area in the models. The natural period in pitch was 7.32% and the reason for this was not found. The regular waves test showed same surge motion in the models, and larger heave motion in the FBM model. There was uncertainties connected to the pitch motion, and a conclusion was not made.

An attempt was made to generate a fourth hydrodynamic model which was a flexible beam model using distributed loads from first order potential theory. A new method was tried by implementing radiation and diffraction pressures from potential theory as hydrodynamic load input for sections of the hull by using SIMO-bodies. This was not finished due to software problems and limited time. A large part of the main objectives for this thesis were connected to the fourth hydrodynamic model, and not finishing this model made it difficult to reach these objectives. To implement the new method for a more complex geometry like the OO-Star Wind Floater Semi 10 MW has proven to be more difficult than first anticipated. It is difficult to draw conclusions to when the different modelling strategies of the hydrodynamic loads are applicable from the three hydrodynamic models made in this thesis. The reason for this is a combination of differences in the models, assumptions and estimations in calculations of parameters, and the lack of background information for used parameters in the models.

5.2 Recommendations for future work

A list of recommendations for future work are given. Only a brief list is given.

1. Finish the flexible beam model using distributed loads from first order potential theory. The MATLAB script is believed to be close to finished. The FBM model can be used as a basis for developing the model in SIMA. Only SIMO-bodies need to be inserted for the different sections in the model with the input calculated.
2. Perform decay tests and a regular waves test on the flexible beam model using distributed loads from first order potential theory. Compare the results against the FBM model and the RBP model.
3. Calculate internal loads in the hydrodynamic models and compare. Check if the hull elasticity effects the dynamic loads.
4. Find out the background information regarding the structural properties used in the hydrodynamic models from the D4.2 report [15].
5. Put the DTU 10 MW reference wind turbine back on the hydrodynamic models and perform coupled dynamic analyses on them.

6. First order potential loads theory was used in this thesis. Higher order potential theory may be done in the future and give more accurate results.

References

[1] Enerdata 2009 - 2018. *Total energy consumption.* URL: https://yearbook.enerdata.net/total-energy/world-consumption-statistics.html.

[2] European Commission. *Climate strategies targets.* URL: https://ec.europa.eu/clima/policies/strategies_en.

[3] Wind Europe. "Wind in power 2017 - Annual combined onshore and offshore wind energy statistics". In: (2018), pp. 6–7. URL: https://windeurope.org/about-wind/statistics/european/wind-in-power-2017/.

[4] Bryhni Ramberg. *Jorden – fordeling av land og hav.* URL: https://snl.no/Jorden_-_fordeling_av_land_og_hav.

[5] Ørstad. "Europe powered by green energy". In: (2017). URL: https://orsted.com/en/About-us/About-orsted/Green-is-cheaper-than-black/North-seas.

[6] 2018 Equinor ASA. *Hywind — the world's leading floating offshore wind solution.* URL: https://www.equinor.com/en/what-we-do/hywind-where-the-wind-takes-us.html#why-hywind.

[7] European Wind Energy Association. "Deep Water - The next step for offshore wind energy". In: (2013). URL: https://windeurope.org/about-wind/reports/deep-water/.

[8] S.W. Im Y.H. Bae M.H. Kim and I.H. Chang. "Aero-Elastic-Control-Floater-Mooring Coupled Dynamic Analysis of Floating Offshore Wind Turbines". In: (2011). URL: https://www.onepetro.org/download/conference-paper/ISOPE-I-11-097?id=conference-paper%5C%2FISOPE-I-11-097.

[9] INC. PRINCIPLE POWER. *Windfloat.* URL: http://www.principlepowerinc.com/en/windfloat.

[10] Fukushima Offshore Wind Consortium. *Fukushima floating offshore wind farm demonstration project.* URL: http://www.fukushima-forward.jp/project01/english/gaiyou/index.html.

[11] Peter Fairley. *Substainable energy, wind power that floats.* Apr. 2008. URL: https://www.technologyreview.com/s/409834/wind-power-that-floats/.

[12] GICON®-SOF. *Technological innovations.* URL: http://www.gicon-sof.de/en/technical-solution.html.

[13] IDEOL 2018 - Réalisation Metycea. *Floatgen demonstrator.* URL: https://www.ideol-offshore.com/en/floatgen-demonstrator.

[14] IRENA. "Floating Foundations: a Game Changer for Offshore Wind Power". In: (2016). URL: http://www.irena.org/DocumentDownloads/Publications/IRENA_Offshore_Wind_Floating_Foundations_2016.pdf.

[15] University of Stuttgart. “Deliverable D4.2 Public Definition of the two LIFES50+ 10MW floater concepts”. In: (2018). URL: http://lifes50plus.eu/wp-content/uploads/2018/04/GA_640741_LIFES50_D4.2.pdf.

[16] Trond Landbø. *Project: LIFES50+*. URL: https://www.olavolsen.no/global/upload/4BPPQ/files/LIFES50%5C%2B.pdf.

[17] Trond Landbø. *OO-Star Wind Floater - the future of offshore wind?* URL: https://www.sintef.no/globalassets/project/eera-deepwind-2018/presentations/closing_landbo.pdf.

[18] Torgeir Moan Marit I. Kvittem Erin E. Bachynski. “Effects of hydrodynamic modelling in fully coupled simulations of a semi-submersible wind turbine”. In: (2012). URL: https://www.sciencedirect.com/science/article/pii/S1876610212011587.

[19] Zhen Gao Ali Nematbakhsh Erin Bachynski. “Comparison of wave load effects on a TLP wind turbine by using computational fluid dynamics and potential flow theory approaches”. In: (2015). URL: https://www.sciencedirect.com/science/article/pii/S0141118715001108.

[20] Kristian Freng Svendsen. *Structural Design and Dynamic Analysis of a Tension Leg Platform Wind Turbine, Considering Elasticity in the Hull*. NTNU, 2016.

[21] Henrik Bredmose Michael Borg Anders Melchior Hansen. “Floating substructure flexibility of large-volume 10MW offshore wind turbine platforms in dynamic calculations”. In: (2016). URL: https://iopscience.iop.org/article/10.1088/1742-6596/753/8/082024.

[22] O.M.Faltinsen. *Sea Loads on ships and offshore structures*. Cambridge university press, 1990.

[23] MARINTEK. *RIFLEX 4.4 Program documentation*. MARINTEK, 2014.

[24] SINTEF Ocean. *RIFLEX 4.14.0 Theory Manual*. SINTEF Ocean, 2018.

[25] Ragnar Sigbjörnsson Ivar Langen. *Dynamisk analyse av konstruksjoner*. Sit Tapir, 1979.

[26] D.E.Newland. *An introduction to Random vibrations, spectral and wavelet analysis*. Longman Scientific Technical, 1993.

[27] Carl M. Larsen. *Marine Dynamics*. NTNU, 2016.

[28] Wl Lian D. Myrhaug. *Marine Dynamics - Lecture notes*. NTNU, 2009.

[29] Sverre Steen. *TMR7:Experimental Methods in Marine Hydrodynamics - Lecture Notes*. Dept. of marine technology, NTNU, 2014.

[30] Butterfield. In: (2007).

[31] Marilena Greco. *TMR4215: Sea Loads - Lecture Notes*. Dept. of marine technology, NTNU, 2012.

[32] DNV GL Software. *HydroD - Hydrodynamic analysis and stability analysis software*. URL: https://www.dnvgl.com/services/frequency-domain-hydrodynamic-analysis-of-stationary-vessels-wadam-2412.

[33] Bjørnar Pettersen. *TMR4247-Marin teknikk 3 Hydrodynamikk*. Kompendieforlaget, 2007.

[34] SINTEF Ocean. *SIMO 4.14.0 Theory Manual*. SINTEF Ocean, 2018.

[35] SINTEF. *Sima*. URL: https://www.sintef.no/en/software/sima/.

[36] Jan R. Hoff. "Estimation of linear and quadratic roll damping from free-decay tests". In: (2001). URL: http://www.ivt.ntnu.no/imt/courses/tmr7/resources/decay.pdf.

[37] DTU. "Deliverable D1.2 Wind turbine models for the design". In: (2015). URL: https://lifes50plus.eu/wp-content/uploads/2015/12/D1.2.pdf.

[38] DTU. "Deliverable D4.5 State-of-the-art models for the two LIFES50+ 10MW floater concepts". In: (2018). URL: https://lifes50plus.eu/wp-content/uploads/2018/05/GA_640741_LIFES50_D4.5-.pdf.

[39] DNV GL Software. *GeniE - An Integrated Design Solution*. URL: file:///C:/program%5C%20files/dnvgl/genie%5C%20v7.7-04/help/UserDocumentation/Introduction/GenieAnIntegrate.html.

[40] DET NORSKE VERITAS. *DNV-RP-C205 ENVIRONMENTAL CONDITIONS AND ENVIRONMENTAL LOADS*. 2010. URL: https://rules.dnvgl.com/docs/pdf/dnv/codes/docs/2010-10/rp-c205.pdf.

[41] Minoo H. Patel. *Dynamics of offshore structures*. Butterworth, 2013.

[42] Orcina Ltd. 1987-2019. *Spectral response analysis*. URL: https://www.orcina.com/SoftwareProducts/OrcaFlex/Documentation/Help/Content/html/Spectralresponseanalysis.htm.

[43] Fabian F. Wendt et al. *International Energy Agency Ocean Energy Systems Task 10 Wave Energy Converter Modeling Verification and Validation*. Technical Committee of the European Wave and Tidal Energy Conference, 2017.

[44] Jared Lewis Krish T. Sharman Amy Robertso. "Heave plate hydrodynamics for offshore wind turbine applications". In: (2015). URL: https://lifes50plus.eu/wp-content/uploads/2015/12/D1.2.pdf.

Appendix

Decay tests for the RBM model

Decay test surge

Table 5.1: Natural period and damping coefficients for surge.

Parameter	Unit	Value
T_0	[s]	186.85
b_1	[s^{-1}]	0.000405
b_2	[m^{-1}]	0.016706

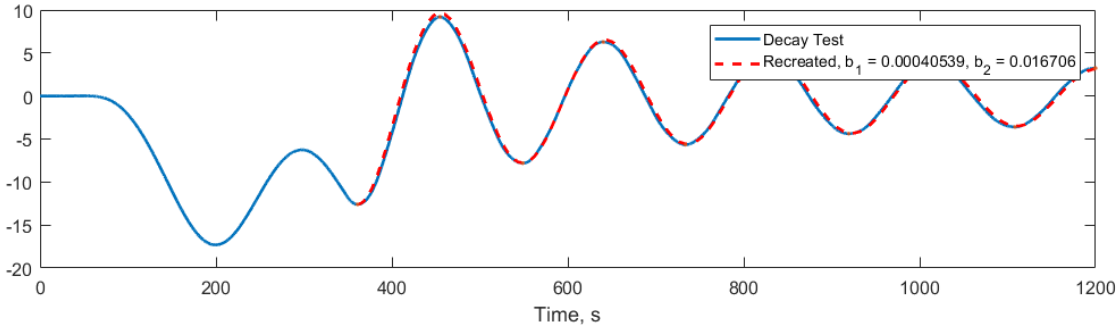

Figure 5.1: Surge motion: Time series plotted together with the recreated motions given by b_1 and $b2$

Decay test heave

Table 5.2: Natural period and damping coefficients for heave.

Parameter	Unit	Value
T_0	[s]	19.35
b_1	[s^{-1}]	0.000238
b_2	[m^{-1}]	0.026415

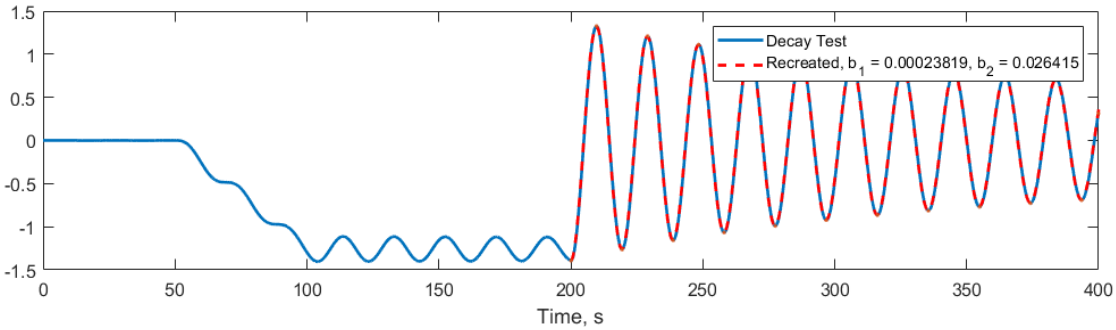

Figure 5.2: Heave motion: Time series plotted together with the recreated motions given by b_1 and $b2$

Decay test pitch

Table 5.3: Natural period and damping coefficients for pitch.

Parameter	Unit	Value
T_0	[s]	29.27
b_1	[s^{-1}]	0.002503
b_2	[m^{-1}]	0 (negative)

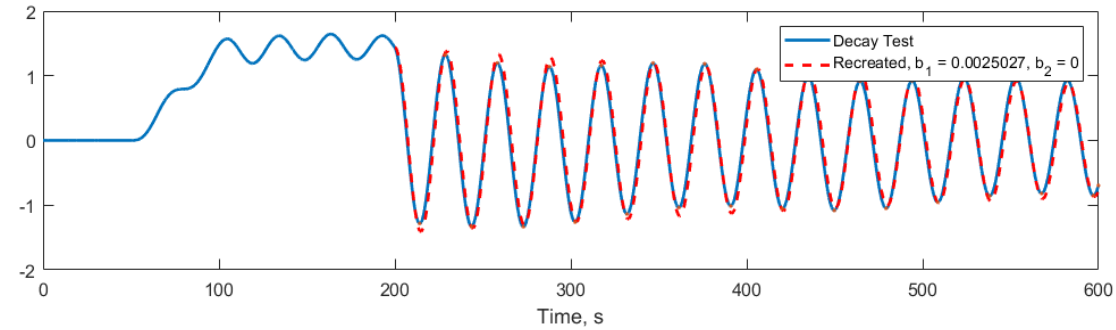

Figure 5.3: Pitch motion: Time series plotted together with the recreated motions given by b_1 and $b2$

Decay test yaw

Table 5.4: Natural period and damping coefficients for yaw.

Parameter	Unit	Value
T_0	[s]	103.62
b_1	[s^{-1}]	0.000405
b_2	[m^{-1}]	0.016706

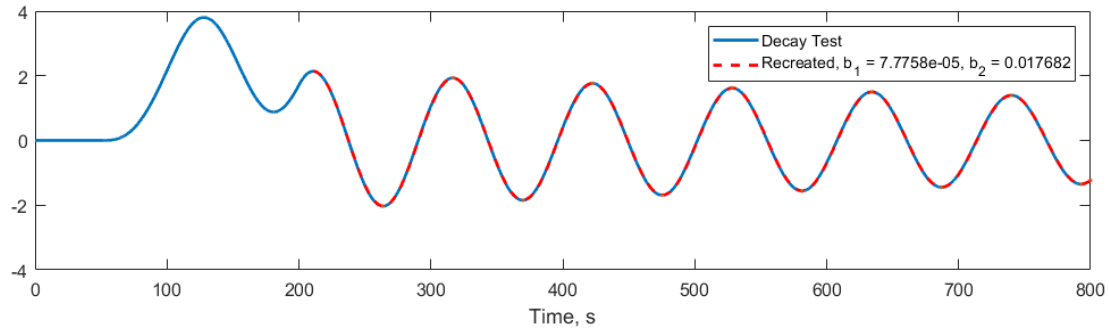

Figure 5.4: Yaw motion: Time series plotted together with the recreated motions given by b_1 and $b2$

Decay tests for the FBM model

Decay test surge

Table 5.5: Natural period and damping coefficients for surge.

Parameter	Unit	Value
T_0	[s]	186.57
b_1	[s^{-1}]	0.000391
b_2	[m^{-1}]	0.016976

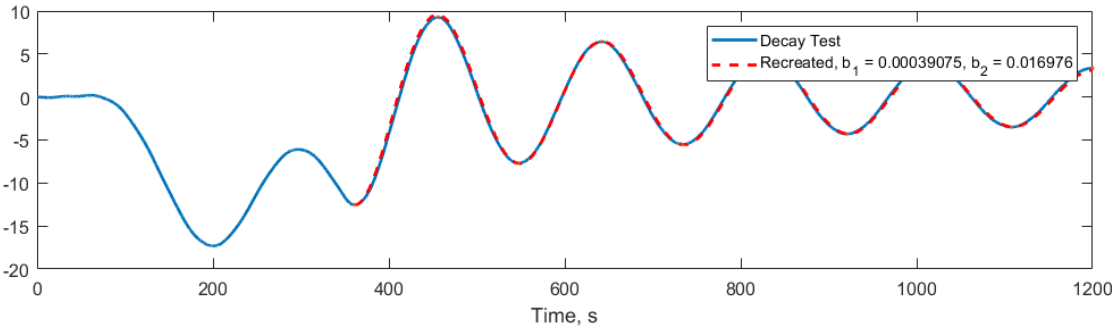

Figure 5.5: Surge motion: Time series plotted together with the recreated motions given by b_1 and $b2$

Decay test heave

Table 5.6: Natural period and damping coefficients for heave.

Parameter	Unit	Value
T_0	[s]	18.84
b_1	[s^{-1}]	0.000508
b_2	[m^{-1}]	0.023962

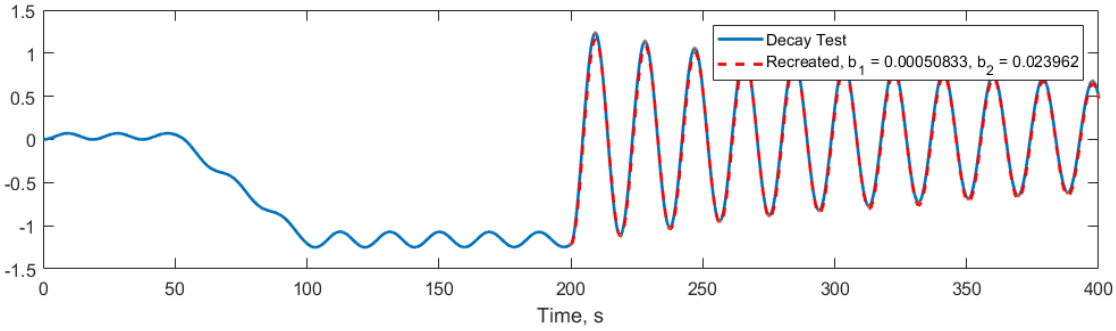

Figure 5.6: Heave motion: Time series plotted together with the recreated motions given by b_1 and $b2$

Decay test pitch

Table 5.7: Natural period and damping coefficients for pitch.

Parameter	Unit	Value
T_0	[s]	31.59
b_1	[s^{-1}]	0.001867
b_2	[m^{-1}]	0.000963

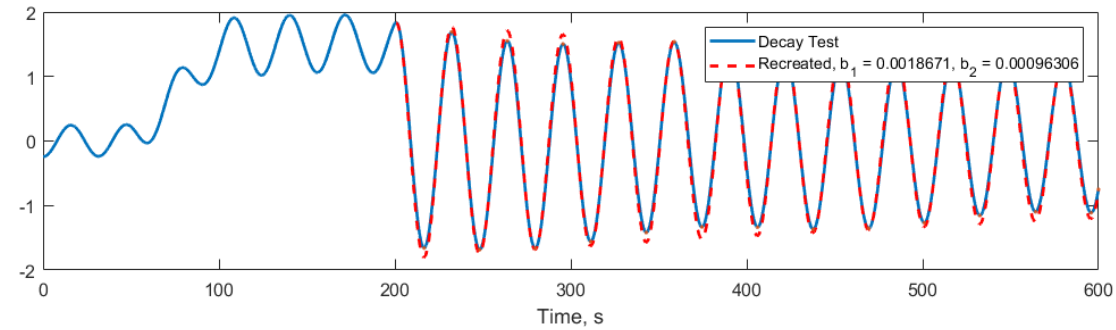

Figure 5.7: Pitch motion: Time series plotted together with the recreated motions given by b_1 and $b2$

Decay test yaw

Table 5.8: Natural period and damping coefficients for yaw.

Parameter	**Unit**	**Value**
T_0	[s]	102.80
b_1	[s^{-1}]	0.000292
b_2	[m^{-1}]	0.018158

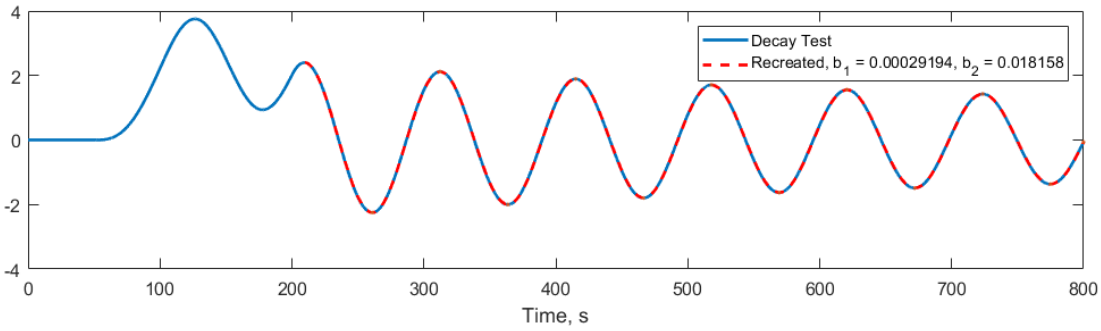

Figure 5.8: Yaw motion: Time series plotted together with the recreated motions given by b_1 and $b2$

Daniel Kaasa

Integrated dynamic analysis of a semi-submersible wind turbine considering hull flexibility

NTNU
Norwegian University of
Science and Technology